DIELECTRIC ANISOTROPY AND OPTICAL TRANSITIONS

by

Sanjay Debnath

A Dissertation

Submitted to the Faculty of Purdue University

In Partial Fulfillment of the Requirements for the degree of

Doctor of Philosophy

School of Electrical and Computer Engineering

West Lafayette, Indiana

December 2022

THE PURDUE UNIVERSITY GRADUATE SCHOOL
STATEMENT OF COMMITTEE APPROVAL

Dr. Evgenii E. Narimanov, Chair

School of Electrical and Computer Engineering

Dr. Andrew M. Weiner

School of Electrical and Computer Engineering

Dr. Alexandra Boltasseva

School of Electrical and Computer Engineering

Dr. Dan Jiao

School of Electrical and Computer Engineering

Approved by:

Dr. Dimitrios Peroulis

Dedicated to my family.

ACKNOWLEDGMENTS

I have been very fortunate to have received support, opportunity, and guidance as a graduate student at Purdue. I sincerely appreciate the help and express my gratitude to all.

First of all, I would like to start by thanking my advisor, Prof. Evgenii E. Narimanov for his relentless help throughout my academic career. Most of my academic achievements can be attributed to his mentorship and continuous support during my Ph.D. journey. I would not be where I am today if not for Prof. Narimanov.

I would like to extend my sincere gratitude to all my committee members: Prof. Andrew M Weiner, Prof. Alexandra Boltasseva, and Prof. Dan Jiao for their valuable feedback and consistent suggestions from the beginning to the end of this journey. Special thanks to Prof. Vladimir Shalaev, Prof. Zubin Jacob, and my ECE mentor Dr. Justus Ndukaife for their guidance and consistent help. Additional humble acknowledgments go out to all my professors at Purdue for valuable courses and intriguing discussions.

A special thank for the diverse student community at Birck Nanotechnology center where I had spent some wonderful years with good memories. I am grateful to several Purdue student organizations: BNC, NSAC, SPIE, OSA, PGSC, BDSA, and Purdue Cricket Club for giving me the opportunity to actively participate while I met many new friends from different backgrounds. I will always cherish the memory of late night discussions with my office colleagues: Samuel Trezitorul, Matthew Storey, Soham Saha, and Shreyas Shah.

At last, my deep love and sincere appreciation go to my parents, siblings, and family-friends within Purdue Village and outside for their consistent inspiration and support. I cannot thank my wife, Sanchita, enough for being there with me all the time, without her this journey would have been impossible. And finally to the joy of my life, my dear son, Dhrubo, for his ability to turn my difficult moments into hope with his smile ('Bhubon Vulano Hashi').

TABLE OF CONTENTS

LIST OF FIGURES

LIST OF SYMBOLS

k_0	vacuum wavevector
c_0	velocity of light in vacuum
λ	wavelength of light
ω	frequency of light
ϵ	dielectric constant
D	displacement vector
P	polarization vector
R	reflectivity
I	radiation intensity
ζ	emissivity
f_m	metal fill fraction
q	momentum wavevector
κ	decay constant
ψ	wavefunction
Γ	decaying factor
J_l	Bessel function of the first kind
H_l^+	outgoing Hankel function
H_l^-	incoming Hankel function

ABBREVIATIONS

As_2S_3	Arsenic Sulfide
CPA	Coherent Perfect Absorption
DP	Diabolic Point
EP	Exceptional Point
H-I	Hyperbolic Type-I
H-II	Hyperbolic Type-II
InAlAs	Indium Aluminium Arsenide
InGaAs	Indium Gallium Arsenide
IPA	Incoherent Perfect Absorption
KTP	Potassium Titanyl Phosphate
LHM	Left Handed Media
LBO	Lithium Triborate
$NaNO_2$	Sodium Nitrite
NIM	Negative Index Mode
OTT	Optical Topological Transition
PT	Parity-Time
PIM	Positive Index Mode
TE	Transverse Electric
TM	Transverse Magnetic
TeO_2	Tellurium Dioxide
TST	Triplet-Singlet-Triplet
ZSW	Zenneck Surface Wave

ABSTRACT

Similar to thermodynamic phase transitions in matter, readily apparent changes in optical response arise in the transition from isotropic to anisotropic optical phases. Treating the anisotropy of the dielectric permittivity as a control parameter, which changes continuously from zero to a nonzero finite value at the transition, in this work we describe the resulting effect on light propagation.

We begin by investigating a simple case of the manifestations of such optical transition in lossy media. In the presence of loss, isotropic materials do not support Brewster phenomenon, however, if one changes the anisotropy continuously, the exact zero in the reflection at the Brewster incidence angle is recovered. Next, in the case of uniaxial anisotropy, we uncover dramatic changes in far-field thermal radiation induced by the transitions between metal, dielectric, and hyperbolic optical regimes that can be observed in the same material. We demonstrate that continuous evolution between different "phases" in the electromagnetic response imprints a characteristic signature in the far-field thermal emission. Finally, we show that the evolution of the optical anisotropy from uniaxial to biaxial symmetry brings qualitatively new optical modes which are different from the conventional propagating and evanescent fields. These emergent "ghost" waves offer a unique way to control mode interactions in optical systems. Our work uncovers the connection between the macroscopic properties of the optical materials and the transitions between different regimes of the electromagnetic response in these media. At last, we propose a range of potential applications of the resulting phenomena, from perfect absorption in lossy media to thermal radiation and optical sensing.

1. INTRODUCTION

Even though matter is made up of enormous number of atoms, the properties of matter are radically different than that of individual atoms. It is the interaction between the constituents that define and control the macroscopic properties. Different phases of matter can be built entirely by the same constituents but with different interactions among them. A transition between thermodynamic phases can be achieved by changing various thermodynamic parameters: water changing from solid to liquid is a common example of many.

Though interactions among the constituents have many degrees of freedom, thermodynamic properties are controlled by a few parameters such as pressure, temperature, density, magnetism, etc. Similarly, the optical refractive index is one of the thermodynamic degrees of freedom responsible for optical responses. Phase transitions in such responses can be achieved by changing the medium refractive index to reach a critical limit. Analogously, we find that optical phase transitions can be controlled by the degree of anisotropy, which is accountable for direction-dependent electromagnetic responses of the media

Since its discovery, optical anisotropy has led to the understanding of fundamental concepts ranging from polarization to light-matter interactions at the microscopic level. In modern-day optics, anisotropy still finds new engineering applications and concepts in fundamental physics. In this work, we show how anisotropy-induced optical phase transitions lead to qualitative changes in light absorption, thermal emission, guided modes, and optical scattering.

We begin our study by considering incoherent perfection absorption using the Brewster effect: a semi-infinite slab of lossless non-magnetic dielectric does not reflect any $p-$polarized light for a certain angle of incidence. But this effect is suppressed due to the loss within isotropic media and consequently fades. However, loss in anisotropic media can bring the Brewster phenomenon back and hence perfect absorption by using the degrees of freedom in material anisotropy. As detailed in Chapter 2, this method employs a simple planar system of air and lossy uniaxial media.

The effect of phase transition in uniaxial media on far-field thermal emission is investigated in Chapter 3. Since the density of microscopic optical states varies as the material

parameters cross over different phases, the number of outcoupled photons also changes accordingly. It is shown that evolution in the topology of electromagnetic responses between different phases leaves a characteristic signature in the far-zone thermal emission. Moreover, we have demonstrated that our results are applicable in both naturally available and artificially structured media.

In Chapter 4, continuous evolution from uniaxial to biaxial media is investigated. The optical modes supported by biaxial media are hybrid in general, consisting of two propagating constants. Moreover, anisotropy-induced nontrivial dynamics turn one of the modes into a negative index mode (NIM)[1] while the optical index of the other mode remains positive (PIM). Eventually, annihilation of PIM and NIM by each other results in "ghost" waves. These are qualitatively new classes of nonuniform waves which are both oscillatory and evanescent in nature. Furthermore, when two such ghost modes are allowed to interact, the resonance frequencies show symmetry-protected degeneracies instead of mode splitting. However, in the presence of asymmetric loss, these degeneracies turn into exceptional points enabling new approaches for optical sensing applications.

Finally, in Chapter 5, we consider anisotropy in artificial structures which support triplet states in optical scattering. It is shown that nontrivial dynamics of such triplet states evolve into a singlet state and a ghost resonance. The ghost resonance is created by the self-annihilation of the other two resonance frequencies. During this evolution, due to the presence of ghost resonance, the system goes through a continuous transition where the constituents change their operating modes. We have theoretically calculated ghost-induced scattering cross section for multiple cylinders.

The various theoretical findings presented in this thesis are within experimental reach. These findings are expected to have a significant impact on light absorption, thermal emission, optical mode interactions, and sensing applications.

2. INCOHERENT PERFECT ABSORBER

This chapter has been partially reproduced from a previous publication [2].

In this chapter we show perfect absorption of electromagnetic waves using Brewster phenomenon. Since the mechanism does not depend on the phase of incoming light, we find that perfect absorption of incoherent light is possible in a semi-infinite lossy slab if the absorption media is anisotropic instead of isotropic. The operating frequency of the proposed system is free of any dependence on physical dimensions.

2.1 Perfect absorption

Perfect absorption, the phenomenon where an electromagnetic wave incident on a medium is absorbed completely without any back reflection, has applications in broad range of areas including biosensing [3], radar cloaking [4], photovoltaics [5] etc. This is usually achieved by manipulating the incoming wave, or the medium, or both.

When the incoming radiation is coherent, perfect absorption can be realized by manipulating the wave to interfere destructively and to dissipate energy into the material, just as in a time-reversed laser. The resulting coherent perfect absorption (CPA) [6], however, is quite sensitive to any perturbation from the coherent state of light, or from the balance between destructive interference and material absorption [7].

On the other hand, with the goal of perfect absorption in mind, manipulation of material generally involves surface impedance matching. Metamaterials, through its tailorable permittivity and permeability components, can demonstrate perfect absorption via resonance in photodetectors [8], sensors [3], microcavities [9] etc. from GHz [10] to visible range [11]. However, material engineering requires a great deal of design effort and complex fabrication process, making it desirable to achieve perfect absorption through simpler means for large scale applications.

The aim of this chapter is to have perfect absorption using incoherent light using the zero reflection of Brewster phenomenon: a semi-infinite slab of lossless non-magnetic dielectric does not reflect any $p-$polarized light for a certain angle of incidence. Under the presence

of an infinitesimal loss for sufficiently large thickness, the slab will eventually absorb all the incident energy. For the resulting perfect absorber, the frequency of operation only depends on material properties.

The condition of no back reflection in Brewster phenomenon does not require any coherence in the incoming wave since it does not depend on any wave interference (required for CPA). As a result, the Brewster effect allows perfect absorption of spatially incoherent radiation. For the incident field that is formed by a random superposition of p- polarized waves, propagating along the Brewster angle with respect to the interface normal (but in an arbitrary direction in the interface plane), the entire energy will be transmitted into the medium and eventually be absorbed. Note that such incident fields are spatially incoherent due to random relative phases between different plane wave components.

In practice materials are lossy. While this lifts the requirement of infinite thickness of the absorber, loss destroys the Brewster phenomenon and only gives a reflection minimum in its stead. Interestingly the same conclusion cannot be generalized to lossy anisotropic media. In fact, incoherent perfect absorption (IPA) has already been predicted theoretically [12–14] and observed experimentally [15] in a strong anisotropic (hyperbolic) medium which shows dielectric and metallic behavior in two orthogonal directions.

In this paper, we show incoherent perfect absorption can be achieved in lossy uniaxial dielectric as well and provide material examples already available in nature. We also develop a physical picture to explain how anisotropy can modify the polarization of a lossy media to bring back the Brewster phenomenon.

2.2 Zero reflection and Brewster angle

The Brewster phenomenon is illustrated in Fig.2.1 where a $p-$polarized light impinges on an interface between two isotropic lossless media and we have a definite angle of incidence where there is no reflection (blue curve). For a two-dimensional planar interface, the Brewster angle only restricts one out of two degrees of freedom in the propagation direction and any incoherent CPA system. Similar to the planar geometry in the present work, a spherical CPA resonator operating at frequency ω_0 for a particular incident field profile $\mathrm{E}_0(r, \omega_0)$, will

also show perfect absorption for any incoherent linear combinations of the incident waves $E_i(r, \omega_0)$ that originate from a spatial rotation of $\mathrm{E}_0(r, \omega_0)$ by an arbitrary angle. Here the CPA leads to zero reflection, for a single spherical harmonic. Due to the rotational symmetry of the system, spatial incoherent superposition of such states, that differ from each other by spatial rotation will also be totally absorbed.

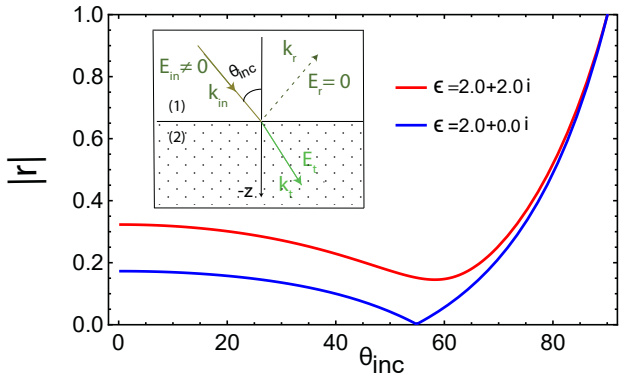

Figure 2.1. Reflection coefficient of a TM polarized light as a function of incident angle from a plane interface between air and isotropic dielectric material(ϵ). The blue and red curves correspond to lossless ($\epsilon = 2$) and lossy ($\epsilon = 2 + i$) material respectively. The inset shows the schematic of the planar system.

If some finite amount of loss is introduced in the isotropic medium, the Brewster phenomenon is not observed and the reflection goes to a minimum instead of zero (see the red curve in Fig. 2.1). However, as we show in the present work that even with lossy materials there could still be possibilities of no reflection if the material is allowed to have optical anisotropy. In the next section, we develop a physical picture of the effect of material polarization.

2.3 Polarization, loss, and anisotropy

When light is incident on a medium, it polarizes the surface molecules and the induced dipoles radiate in unison. The transmitted wave is the summation of the forward scattered light from these dipoles and the incident energy, which is reflected in one of Maxwell's Eq. $\nabla.\mathbf{D} = 0$ where the displacement field $\mathbf{D} = \epsilon_0\mathbf{E} + \mathbf{P}$ contains both the electric field $\mathbf{E}$ and the polarization $\mathbf{P}$.

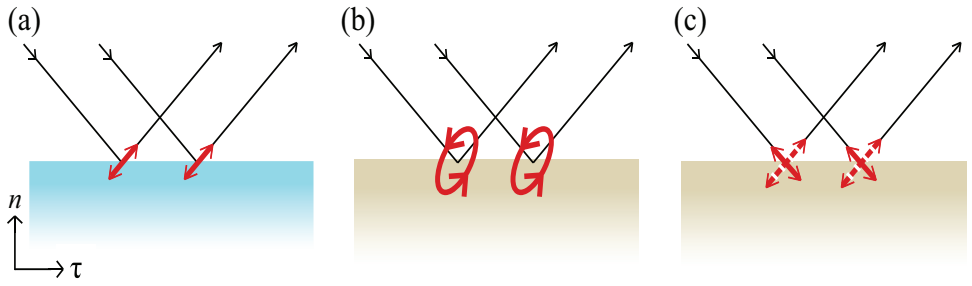

Figure 2.2. Origin of Brewster phenomenon illustrated in terms of material polarization. (a) A lossless isotropic medium with $p-$polarized light incident at the Brewster angle will have all the induced dipoles (shown by red arrows) aligned along the reflection direction. (b) However, if there is loss present in the medium, the dipoles, instead of oscillating along a line, rotate with an elliptical trajectory. (c) This can be viewed as a superposition of two orthogonal linear dipole oscillations with a phase delay as shown by the dotted and solid arrows. The presence of dipoles oscillating perpendicular to the reflected ray (solid arrows) sends energy back and suppresses the Brewster phenomenon.

The reflected wave, on the other hand, is the back-scattered radiation wavefront coming from these dipole sources. If one looks at one oscillating electric dipole, one sees the emanating radiation expand in spherical shells with the speed of light. However, not all points on the spherical surface represent to the same radiated energy [16]. The points on the equator of the sphere correspond to the most intensity whereas no energy is carried along the polar direction. As one considers more than one single dipole, interference between the radiation takes place and the emission angle narrows just as for an antenna array. For a plane wave illumination on a material surface, we get a continuum picture of induced dipoles and the emission becomes a ray, sending energy only in one direction with an intensity dependent on the orientation of the dipole axis with respect to the reflected ray.

For $s-$polarized light the electric field and hence the polarization is perpendicular to the reflection direction, and as a result, there is always energy available in the reflected light since it is contained in the equatorial plane of all the individual dipoles. However, for $p-$polarized light there can be a situation when the dipole axis points along the reflection direction (see Fig. 2.2(a)). In that case, the reflected ray contains no energy and we have the Brewster phenomenon.

Now if we consider an isotropic medium with loss described by a complex permittivity scalar ϵ, the transmitted light decays as it propagates because of absorption. This is indicated by the complex nature of the normal component of the wavevector $\mathbf{k} = (k_\tau, k_n)$ given by

$$k_n = \sqrt{\epsilon \left(\frac{\omega}{c}\right)^2 - k_\tau^2} \tag{2.1}$$

with ω being the frequency of light. Consequently, the polarization $\mathbf{P} = (P_\tau, P_n)$ will have a phase delay introduced between its two components P_τ and P_n since

$$\frac{P_n}{P_\tau} = \frac{E_n}{E_\tau} = \frac{D_n}{D_\tau} = -\frac{k_\tau}{k_n} \tag{2.2}$$

is not real (here the last equality followed from $\nabla \cdot \mathbf{D} = 0 \Leftrightarrow \mathbf{k} \cdot \mathbf{D} = 0$). Therefore, instead of having the induced dipoles oscillating linearly, we have a rotating dipole picture whose trajectory in general is elliptical (see Fig. 2.2(b)). This dipole oscillation can then again be decomposed in two non-zero components (see Fig. 2.2(c)): one along the reflected ray (dashed arrows) and the other perpendicular to it (solid arrows). The presence of dipoles oscillating perpendicular to the reflected ray sends energy back from lossy isotropic medium and kills the Brewster condition.

However for uniaxial anisotropic material described by permittivity components $(\epsilon_\tau, \epsilon_n)$, Eq. (2.2) is modified as

$$\frac{P_n}{P_\tau} = \frac{\epsilon_n - 1}{\epsilon_n} \frac{\epsilon_\tau}{\epsilon_\tau - 1} \frac{D_n}{D_\tau}. \tag{2.3}$$

Even though loss introduces a phase difference in the components of $\mathbf{D}$, the different scaling factors in Eq. (2.3) can still cancel that phase and make $\mathbf{P}$ linearly oscillate again, as in lossless isotropic case (Fig. 2.2(a)). This phase cancellation condition, which can bring back the Brewster phenomenon, would make perfect absorption possible in lossy anisotropic media. In the next section we further show that this loss-induced perfect absorption can only exist in uniaxial dielectric and hyperbolic media, but not in metals.

2.4 Mathematical description

Let us consider a $p-$polarized light incident from medium 1 onto the interface with medium 2. If the permittivity components tangential and normal to the interface are given by $\epsilon_{1\tau}$ and ϵ_{1n} for medium 1, and those for medium 2 by $\epsilon_{2\tau}$ and ϵ_{2n}, respectively, then the Fresnel reflection coefficient [17] is

$$r_{\rm p} \;=\; \frac{\varepsilon_{2\tau}k_{1\rm n} - \varepsilon_{1\tau}k_{2\rm n}}{\varepsilon_{2\tau}k_{1\rm n} + \varepsilon_{1\tau}k_{2\rm n}}, \tag{2.4}$$

where the wavevectors in the two media $\mathbf{k_1} = (k_{1\tau}, k_{1n})$ and $\mathbf{k_2} = (k_{2\tau}, k_{2n})$ maintain

$$\frac{k_{1\tau}^2}{\varepsilon_{1\rm n}} + \frac{k_{1\rm n}^2}{\varepsilon_{1\tau}} = \left(\frac{\omega}{c}\right)^2 = \frac{k_{2\tau}^2}{\varepsilon_{2\rm n}} + \frac{k_{2\rm n}^2}{\varepsilon_{2\tau}}. \tag{2.5}$$

The zero(s) of $r_{\rm p}$ corresponds to the zero reflection for the IPA. Then from Eq. (2.4) we have

$$\varepsilon_{2\tau}k_{1\rm n} \;=\; \varepsilon_{1\tau}k_{2\rm n}. \tag{2.6}$$

Due to translational symmetry, the tangential components of the wavevectors will be same for both media: $k_{1\tau} = k_{2\tau} \equiv k_\tau$. If we assume medium 1 to be lossless air ($\epsilon_{1\tau} = \epsilon_{1n} = 1$) then we get

$$\varepsilon'_{2\tau} + \frac{\varepsilon''_{2\tau}}{\varepsilon''_{2\rm n}}\varepsilon'_{2\rm n} \;=\; \frac{1}{1 - (\frac{c}{\omega})^2 k_\tau^2} \tag{2.7}$$

where ϵ' and ϵ'' represent the real and imaginary parts of the corresponding permittivities. The right hand side of Eq. (2.7) is always positive as $(\frac{c}{\omega})^2 k_\tau^2 < 1$. Since medium 2 is absorbing $\varepsilon''_{2\tau}, \varepsilon''_{2\rm n} > 0$, both $\varepsilon'_{2\tau}$ and $\varepsilon'_{2\rm n}$ cannot be negative simultaneously. This condition shows that lossy metals cannot exhibit zero reflection from the air-metal planar interface. Except for metals, other materials satisfying Eq. (2.7), such as an anisotropic dielectric or a

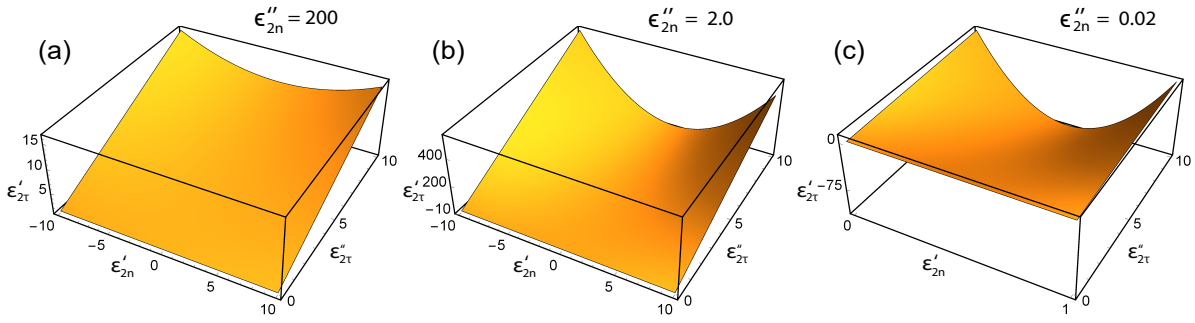

Figure 2.3. Three dimensional plot of the real part of the tangential permittivity that corresponds to the incoherent perfect absorption for incidence from air, vs. the real and imaginary parts of the normal component of the permittivity. Panel (a) corresponds to the imaginary part of the normal permittivity component $\varepsilon''_{2n} = 200$. Here the real part of the tangential permittivity $\varepsilon'_{2\tau}$ is positive everywhere in the plot, so that the range $\varepsilon'_{2n} < 0$ correspond to the hyperbolic regime, while the region with $\varepsilon'_{2n} > 0$ describes a dielectric. In panel (b), the imaginary part of the normal permittivity component $\varepsilon''_{2n} = 2$, and the solution includes both hyperbolic and dielectric bands. Note that $\varepsilon'_{2\tau}$ and ε'_{2n} are never simultaneously negative. In panel (c), we have $\varepsilon''_{2n} = 0.02$. Here the region the region $0 < \varepsilon'_{2n}$ with $\varepsilon'_{2t} < 0$, again corresponds to the hyperbolic behavior.

hyperbolic medium, may support zero reflection. To find the condition for perfect absorption in terms of material parameters, we find

$$(\varepsilon''_{2n})^2 - \frac{\varepsilon''_{2n}}{\varepsilon''_{2t}}(\varepsilon'_{2\tau} - 1) - \varepsilon'_{2n} + (\varepsilon'_{2n})^2 \quad = \quad 0 \tag{2.8}$$

which can be shown to be consistent with the phase canceling condition developed in the previous section.

Equation (2.8) can be used as a criterion for zero reflection in any nonmagnetic ($\mu = 1$) lossy uniaxial material. The solution of Eq. (2.8) for $\varepsilon'_{2\tau}$ is shown in Fig. 2.3 as a function of other material parameters. Each point in Fig. 2.3 corresponds to the combination of the material permittivity for zero reflection. Note that the observed behavior is consistent with the predictions [14] of perfect absorption for hyperbolic material with large transverse and small axial components of the permittivity tensor. Additionally, Eq. (2.8) predicts that lossy dielectric with permittivity components satisfying the condition would provide

zero reflection as well (see Figs. 2.3(a)-2.3(b)). In the following section we will show few examples of naturally available lossy dielectric material to support the above result.

2.5 Material examples

As an example of the preceding discussion, we show sapphire (Al_2O_3), a commonly used material in optical applications [18] is naturally anisotropic. The dielectric permittivity [19] in the infrared spectral range and the reflection coefficient from Eq. (2.4) are plotted in Figs. 2.4(a)-2.4(c). Fig. 2.4(c) shows that for the dielectric permittivities $(\varepsilon_{\rm n}, \varepsilon_\tau) \approx (-1.474 + 0.146\ i, 8.326 + 0.292\ i)$ at the frequency $\omega \approx 503.46$ cm^{-1}, Al_2O_3 satisfies the zero-reflection condition even though the material has loss. This is consistent with the predictions in [15] which pointed out perfect absorption by lossy indefinite anisotropic medium. While this frequency is within the hyperbolic band, nontrivial dispersion of sapphire also leads to the zero reflection at another frequency $\omega \approx 520.93$ cm^{-1}. At this frequency, the permittivity components $(\varepsilon_{\rm n}, \varepsilon_\tau) \approx (2.099 + 0.079\ i, 15.274 + 0.491\ i)$ of sapphire is from dielectric band. Consequently, if a $p-$ polarized wave of that specific frequency impinges on a half infinite Al_2O_3 slab, all the incoming light will be absorbed.

For the second example, we use hexagonal Boron-Nitride (h-BN), another promising optical application [20] platform. Anisotropic properties of this material are shown in the dielectric permittivity [21] plot (Fig. 2.5(a)). The reflection coefficient plot in (Fig. 2.5(b)) indicates that perfect absorption occurs at frequencies $\omega \approx 611.7$ cm^{-1} and $\omega \approx 952.8$ cm^{-1} which are consistent with the results in [15]. Thus, a p-polarized light will be perfectly absorbed at those frequencies and the corresponding Brewster angles are 68.8° and 72.9° respectively shown in (Fig. 2.5(c)). Notice that the permittivity values $(\varepsilon_{\rm n}, \varepsilon_\tau) \approx (7.351 + 0.038i, 6.794 + 0.0047i)$ and $(\varepsilon_{\rm n}, \varepsilon_\tau) \approx (3.051 + 0.0159i, 8.084 + 0.0180i)$ are both from the dielectric band. The nonzero imaginary parts of the permittivity tensor show that despite being lossy, h-BN supports perfect absorption.

IPA can also be observed for higher energy photons upto and including ultraviolet frequency band. For example anisotropic dielctric response of graphite [22] satisfies Eq. (2.8)

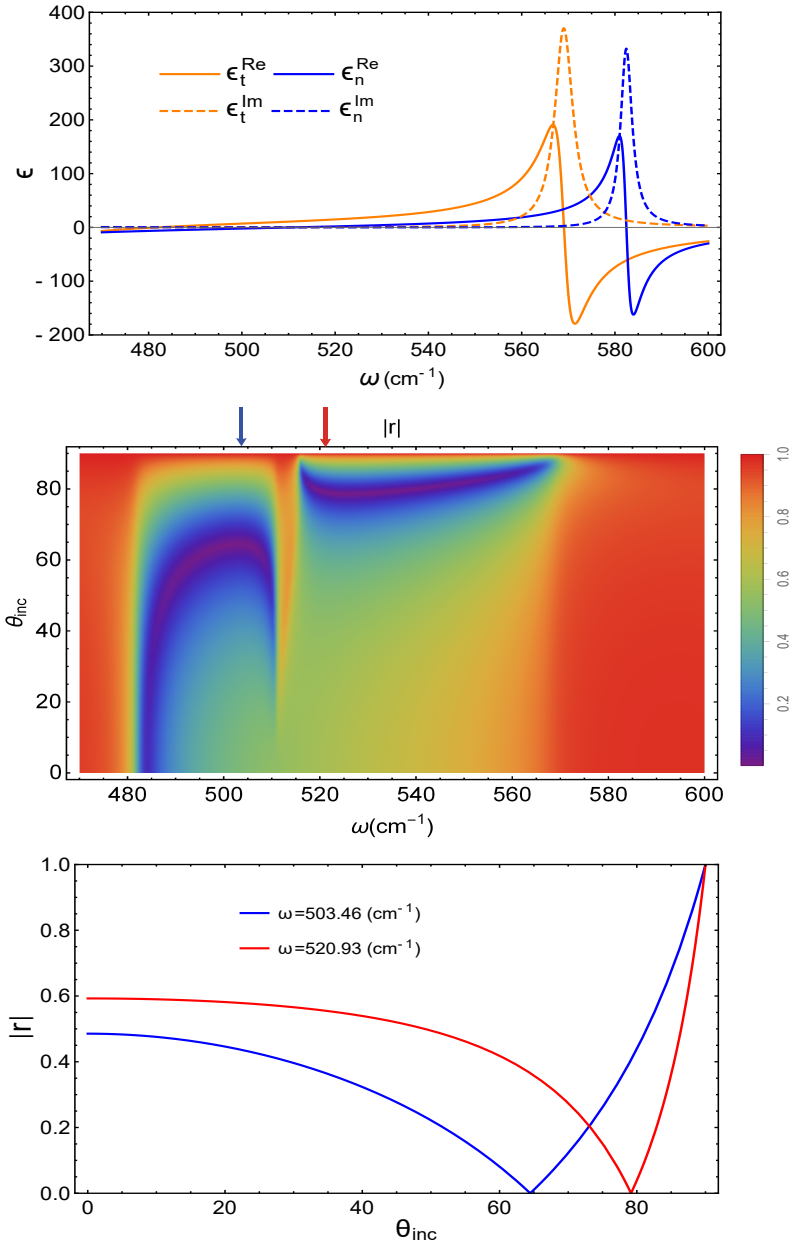

Figure 2.4. Perfect absorption from Al_2O_3 - air interface: (a) dielectric permittivity [19] of both tangential and normal components of Al_2O_3 slab vs. frequency, (b) 2D plot of reflection from Al_2O_3 slab for $p-$ polarization as a function of incident angle (degrees) and frequency (cm^{-1}). The false color shows the reflection amplitude. Note the presence of perfect absorption at the frequencies $\omega \approx 503.46$ cm^{-1} and 520.93 cm^{-1}, indicated by the arrows, (c) the absolute value of the reflection coefficient as a function of incident angle for the frequencies indicated by two arrows in (b). Reflection at 64.465° and 79.151° respectively goes to zero, corresponding to the Brewster angles for the indicated frequencies.

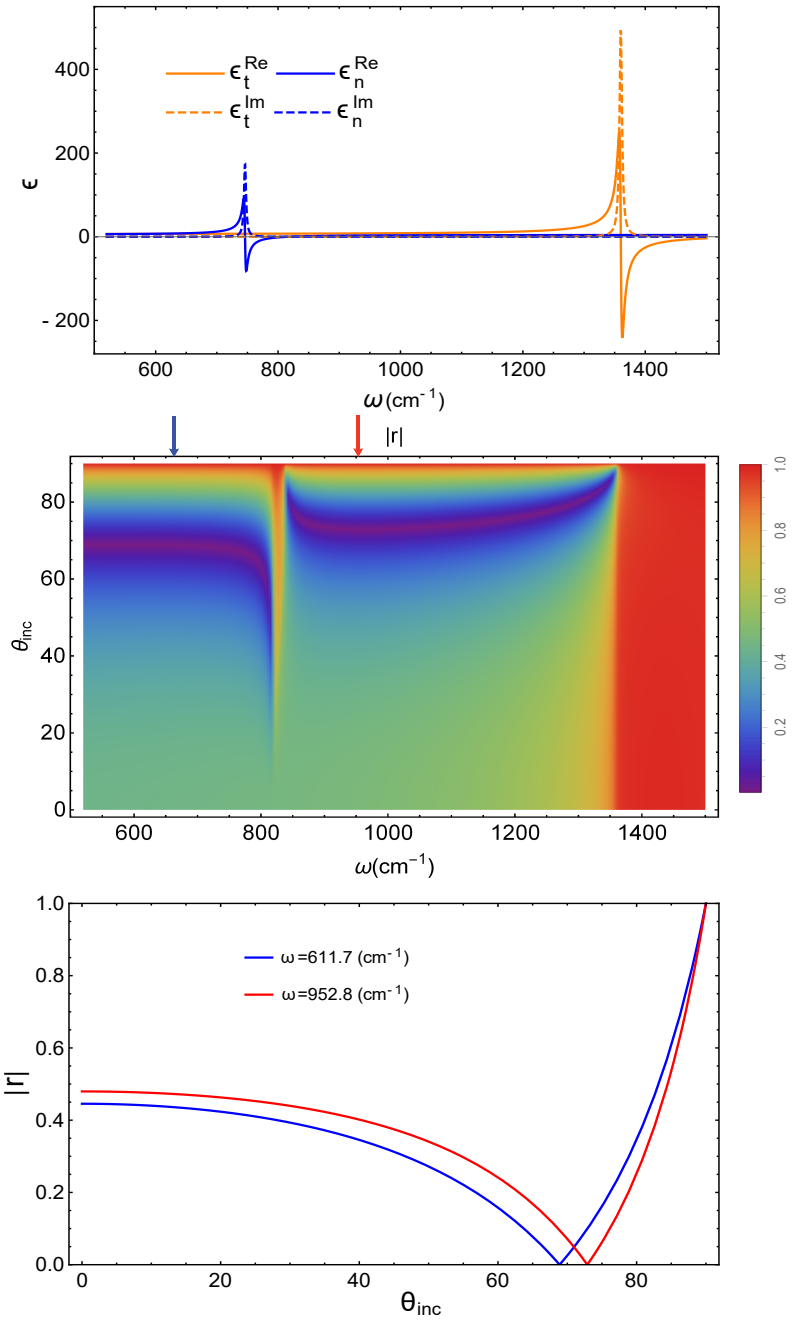

Figure 2.5. Perfect absorption from h-BN - air interface: (a) dielectric permittivity of h-BN slab as a function of frequency, (b) 2D plot of reflection from hBN-air interface for $p-$ polarized light as a function of incident angle (in degrees) and frequency (cm^{-1}). The false color shows the reflection amplitude, and the presence of perfect absorption at frequency $\omega \approx 611.7$ cm^{-1} and $\omega \approx 952.8$ cm^{-1} are shown by the blue and red arrows respectively, (c) the absolute value of the reflection coefficient as a function of incident angle for the indicated arrow in (b).

for $\omega \approx 27027$ cm^{-1} and 39215 cm^{-1} (corresponding $\lambda \simeq 370$ nm and 255 nm, respectively) at the interface orthogonal to the basal crystallographic plane.

2.6 Discussion

Perfect absorption due to Brewster phenomenon in planar media is related to the associated Brewster wave [23]. If, starting from lossless isotropic dielectric, we continuously increase the losses in the material, the Brewster wave evolves directly into the Zenneck surface wave (ZSW) [24]. Inherent leaky nature of ZSW for isotropic lossy dielectric material makes the reflection coefficient minimum instead of zero (red curve in Fig. 2.1). In fact, the criterion for zero reflection in Eq. (2.6) is identical to the Eq. for ZSW in lossy isotropic dielectric material. These identical Eqs. stem from the same boundary condition for both Brewster wave and ZSW, which implies that there is only one wave at infinity in the first medium.

Equation (2.8) is a non-trivial constraint on the medium parameters for the zero reflection condition, and hence not all anisotropic dispersive material can be candidates for IPA. However, consideration of biaxial and magnetic materials [13] may expand the solution space, even for other polarizations of light. Furthermore, a particular material is not restricted to satisfy Eq. (2.8) only at a single frequency. Instead, as shown in the examples of Al_2O_3, h-BN, and graphite, there could be multiple operating frequencies for the same material. Since the proposed system does not require any additional layered or surface structures, the operating frequency depends solely on material parameters, making this technique suitable for broad range of sensing and thermal applications.

So far, we have considered the case of planar system that has infinite thickness. Restriction to finite thickness due to practical consideration will not change the results appreciably because of the exponential field decay ($\sim \exp(-\mathrm{Im}\{k_n\}z)$) inside the medium. The corresponding absorption length $\delta = 1/\mathrm{Im}\{k_n\}$ then characterizes the absorber performance. For the examples given in this article the absorption lengths for sapphire, h-BN and graphite are on the order of tens of microns, a few millimeters and few hundred nanometers, respectively.

2.7 Summary

A planar system for incoherent perfect absorption has been proposed and the relevant condition on material parameters has been derived. To explain the associated principle a physical picture is given from material polarization perspective. The scope of material choice for potential realization of such a system has been extended from hyperbolic media to lossy uniaxial dielectric class, and material examples have been provided.

3. THERMAL EMISSION AT THE OPTICAL TOPOLOGICAL TRANSITION

This chapter has been partially reproduced from a previous publication [25].

In this chapter we develop a theoretical description of far-field thermal radiation near optical topological transitions of uniaxial media. Our results show a strong asymmetric pattern of reduced emission near the transition from type-I hyperbolic to dielectric responses and are applicable in both naturally available and composite media.

3.1 Optical topological transition

Conventional phase transitions in materials may be induced by changes in temperature or stress. Similarly, optical properties also exhibit a drastic change due to a variation in external parameters such as photon energy. For example, silver is reflective for low energy photons but transparent for photons above the plasma frequency. Optical topological transition (OTT) corresponds to the drastic change in the electromagnetic response. This originates from a transformation in the topology [26] of the phase space for light waves propagating in the medium.

Optical responses of different "phases" differ in many aspects. For example, in the dielectric phase light passes through in all directions, but the propagation is diffraction limited [27]. On the other hand, in the "hyperbolic" phase [28] light propagates in limited directions and does so without beam broadening. This is due to the "hyperbolic" phase behaving like a metal in one direction and a dielectric in the orthogonal direction. Finally, in the metallic phase, no propagating waves are supported at all. Transition between these phases results in drastic changes such as reduced reflection, spontaneous emission [29], superresolution imaging [30], enhanced radiative thermal conductivity [31], and near-field super-Planckian [17, 32–34] radiation.

In this article, we show that optical topological transitions have strong effect in far-field thermal radiation as illustrated in Fig. 3.1(a). Note the drastic change in thermal radiation

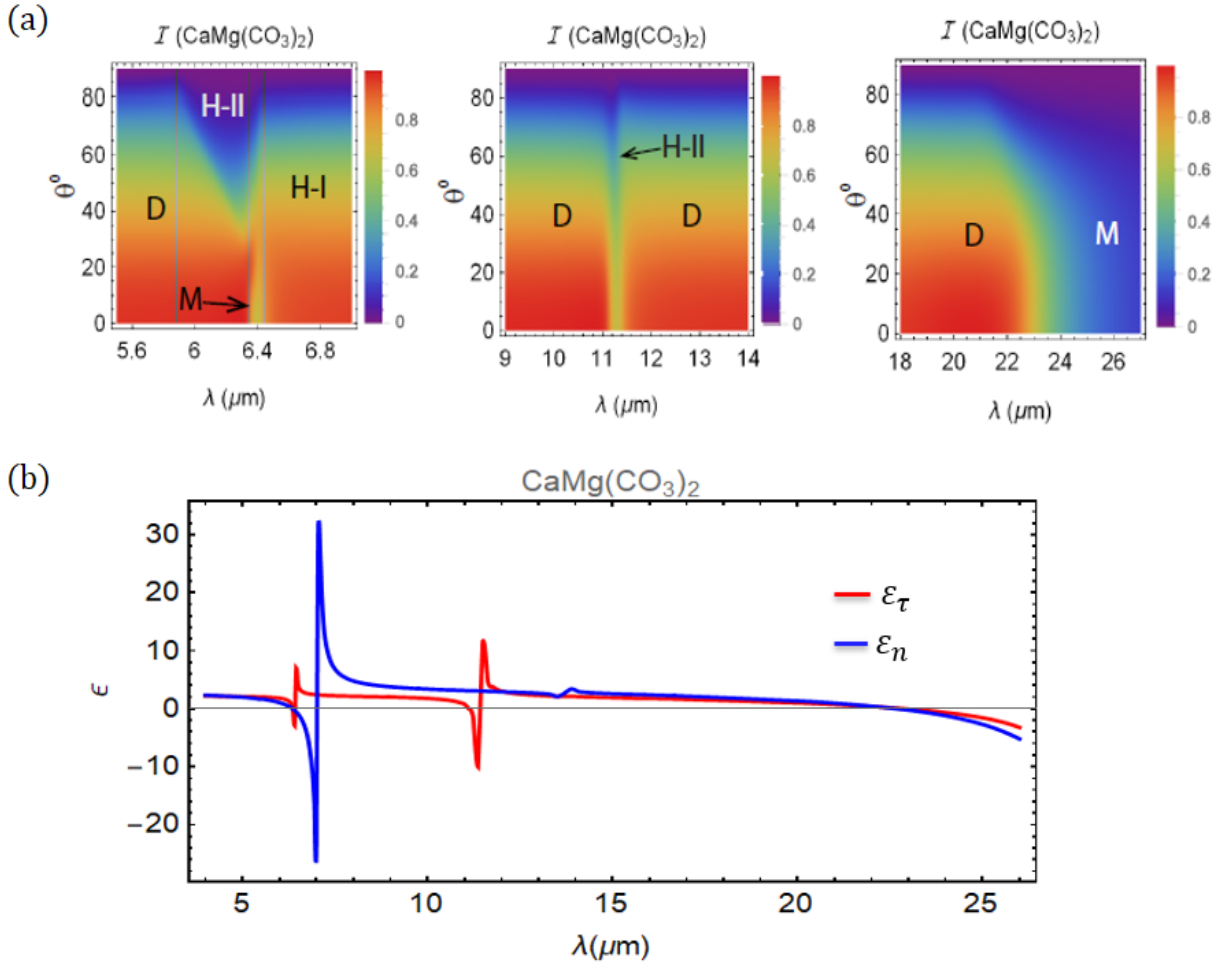

Figure 3.1. Far-field radiation intensity ($\mathcal{I}$, normalized to blackbody [35]) plot from dolomite ($CaMg(CO_3)_2$)[36] mineral as a function of frequency and radiation angle (θ) from a flat interface as shown in panel-(a) for several wavelength regimes. Different optical phases: dielectric ($\epsilon_n > 0, \epsilon_\tau > 0$), anisotropic metal ($\epsilon_n < 0, \epsilon_\tau < 0$, hyperbolic type-I ($\epsilon_n < 0, \epsilon_\tau > 0$) and hyperbolic type-II ($\epsilon_n > 0, \epsilon_\tau < 0$) are indicated by D, M, H-I, and H-II, respectively. Note that the color coded numerical value of intensity has different characteristic profiles for different OTTs. Panel-(b) shows the corresponding anisotropic dielectric permittivities where ϵ_τ and ϵ_n represent permittivities along tangential and normal directions of planar dolomite crystal, respectively.

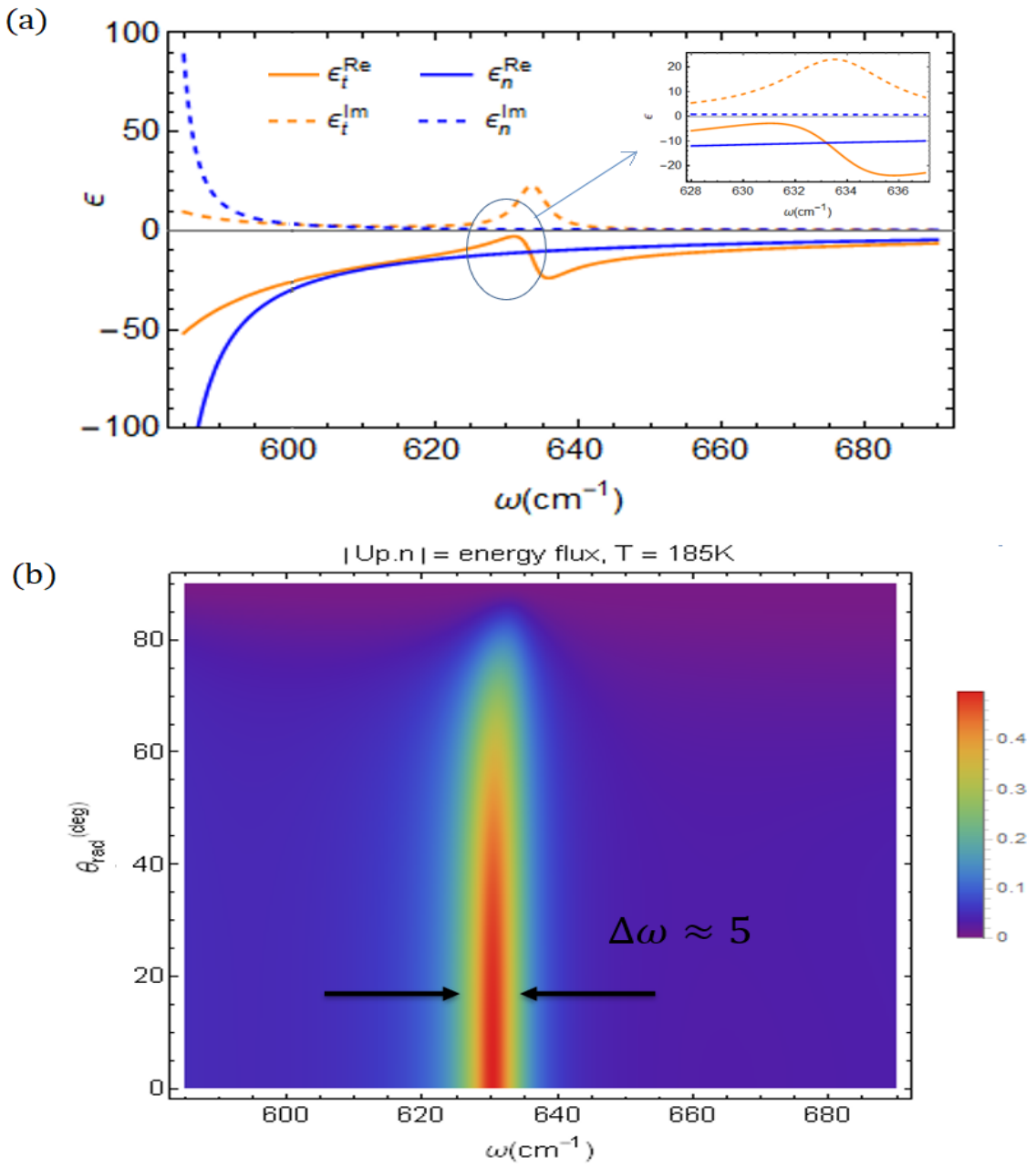

Figure 3.2. Thermal radiation due to ghost transition. Panel -(a) shows the dielctric permittivity of sapphire Al_2O_3 [19] for metallic band. Solid and dotted lines correspond to the real and imaginary parts of the permittivity, respectively. Even though, both real parts are negative within the bandwidth considered here, one of the components was about to change its sign (ghost transition, inset shows magnified image). The corresponding far-zone thermal radiation is shown in panel-(b) where we see no radiation due to metallic phase except the ghost region which results in narrowband emission with $\Delta\omega \approx 5\text{cm}^{-1}$.

leaving emission features within the parameter space of radiation angle and wavelength, considered in this analysis. Furthermore, as pointed out, each radiation feature is related with corresponding optical phase (D, M, H-I, H-II, etc.) which evolves as the permittivities $(\epsilon_{\rm n}, \epsilon_\tau)$ change with wavelength as shown in panel-(b). At the crossover of optical phases where one of the permittivity components changes its sing, topology of electromagnetic responses leave characteristic signature in the far-zone thermal emission. The signature is even evident in the case of "ghost" transition: a topological change which did not take place but was about to, as shown in Fig. 3.2.

For understanding the OTT, we use the concept of the isofrequency surface: a surface of allowed electromagnetic modes in the momentum space at constant frequency. The dispersion relation of an uniaxial medium can be described by the equation $k_\tau^2/\epsilon_n + k_n^2/\epsilon_\tau = (\omega/c)^2$ for p-polarized wave. Here the wavevector of the propagating wave is given by $\vec{k} \equiv (k_\tau, k_n)$, ω is the frequency of radiation, c is the light speed in vacuum and the dielectric permittivities $\{\epsilon_\tau, \epsilon_n\}$ are along the tangential and normal propagation directions, respectively. The constant frequency surface of the dielectric $(\epsilon_\tau, \epsilon_n > 0)$ phase in momentum space forms an ellipsoid. On the other hand, when permittivity tensor components have opposite signs, the isofrequency surface forms a hyperboloid (different topology). The contrast between open topology of hyperboloid and close topology of ellipsoid shows up qualitative differences in the propagating waves of the corresponding phases. The wavenumbers in case of hyperbolic phase are not limited by the isofrequency surface, while they are confined by the frequency in dielectric phase.

Even though hyperbolic media support large wavenumbers exceeding the outside medium wavenumber $(k_0 = \omega/c_0)$, the energy is carried into the far zone by corresponding propagating modes. If the interface of the material and the outside medium is flat, then the symmetry of the system allows waves with tangential momentum between $-k_0$ and $+k_0$ (low k), satisfying momentum conservation, to outcouple. Hence, the low k momentum subspace dictates far-field thermal radiation properties.

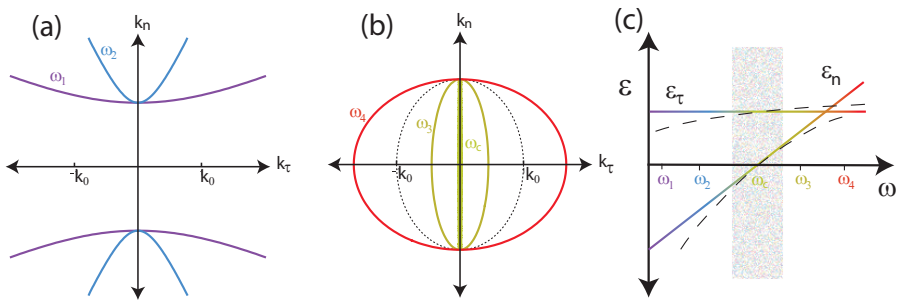

Figure 3.3. 2D plot of isofrequency surface (contour) for lossless uniaxial anisotropic medium. Type-I hyperbolic phase in panel (a) shows that it supports low-k momentum for all frequencies (e.g.: ω_1, ω_2). As the frequency changes, open isofrequency contour turns into a closed one at $\omega = \omega_c$ and the medium becomes dielectric. The isofrequency contour of the dielectric phase (ω_3, ω_4) is plotted in panel (b). The corresponding frequencies are indicated by different colors in the dielectric permittivity plot in panel (c) where ϵ_τ remains positive and ϵ_n changes sign at $\omega = \omega_c$. The asymmetric feature of the thermal radiation related to the OTT appears near the proximity of ω_c indicated by the shaded region. In this range, the linear model of the material permittivity even though it may be significantly different, is accurate to the actual value.

3.2 Mathematical model of OTT

In this letter, we focus on a particular OTT: hyperbolic type-I to dielectric phases where ϵ_τ remains constant and ϵ_n changes sign with frequency. Isofrequency surfaces of both phases (see ω_1 and ω_4 in Fig. 3.3) have tangential momenta spanning the entire momentum space from $-k_0$ to $+k_0$ of the outside medium. As a consequence, thermal radiation far away from the OTT critical frequency appears to be very similar for both phases. However, the signature of the OTT is quite evident near the transition frequency. Furthermore, we predict that this OTT will have a unique far-field thermal emission feature present in the parameter space of radiation angle and frequency for $p-$polarized waves.

To calculate the far-field radiation pattern near the OTT, we analyze the evolution of the isofrequency surface (Figs. 3.3(a)-3.3(b)) in the vicinity of the transition. In the hyperbolic phase, the entire low k spatial spectrum is supported by the medium allowing for thermal radiation in all directions. At the transition frequency, the closed isofrequency surface (ω_c) only supports tangential momentum $k_\tau = 0$. As the frequency increases beyond

the transition, the closed isofrequency surface (ω_3) will only support a subset of the low k momentum. Therefore, due to momentum matching conditions only certain directions of outcoupled radiation are supported. The allowed tangential momenta for far-field thermal emission from the dielectric band can be expressed as

$$k_\tau < k_0\sqrt{\epsilon_n(\omega)}. \tag{3.1}$$

The far-field emission profile from a planar surface can be related to the reflectivity [17],

$$\xi(\omega,\theta) = (1-R)\cos\theta \tag{3.2}$$

where $\xi(\omega,\theta)$ is the thermal emissivity [37] at the radiation angle θ with respect to surface normal and R is the Fresnel reflection co-efficient. For a low-loss material, the reflectivity near the OTT can be obtained from the approximation that neglects the (small) imaginary part of the dielectric permittivity. Furthermore, in the vicinity of the OTT we can neglect the frequency dispersion of the permittivity component that does not change sign at the transition, while for the other component we use linear approximation for frequency dependence. We therefore approximate $\epsilon_\tau(\omega) \approx \epsilon_\tau(\omega_c)$ and $\epsilon_n(\omega) \approx \alpha(\omega-\omega_c)$. The corresponding thermal emissivity due to the $p-$polarized wave is obtained as follows

$$\xi_p(\omega,\theta) \approx a(\theta) \times \begin{cases} \frac{\omega-\omega_c-b_1(\theta)}{\omega-\omega_c-b_2(\theta)}, & \{\omega,\theta\} \in \mathrm{A} \\ 0, & \{\omega,\theta\} \in \mathrm{B} \\ 1+\frac{b_3(\theta)}{\omega-\omega_c}, & \{\omega,\theta\} \in \mathrm{C} \end{cases} \tag{3.3}$$

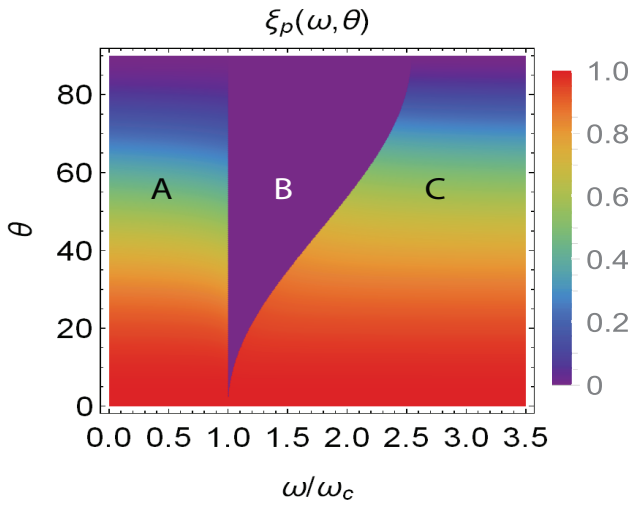

Figure 3.4. 2D plot of spectral directional emissivity as a function of frequency and radiation angle. Numerical value of the emissivity is shown by the false color on the scale from 0 to 1. Here we use ϵ_τ=1 for the entire spectrum and linearly increasing value of ϵ_n ($\alpha = 0.65$) with frequency which changes its sign from negative to positive at $\omega = \omega_c$. Therefore, region A corresponds to hyperbolic and regions B, C are within the dielectric band.

where

$$a(\theta) = \frac{4\sqrt{\epsilon_\tau(\omega_c)}\cos^2\theta}{(1+\sqrt{\epsilon_\tau(\omega_c)}\cos\theta)^2}, \tag{3.4}$$

$$b_1(\theta) = \frac{\sin^2\theta}{2\alpha}, \tag{3.5}$$

$$b_2(\theta) = \frac{1}{(1+\sqrt{\epsilon_\tau(\omega_c)}\cos\theta)}\frac{\sin^2\theta}{\alpha}, \tag{3.6}$$

$$b_3(\theta) = \frac{(1-\sqrt{\epsilon_\tau(\omega_c)}\cos\theta)}{(1+\sqrt{\epsilon_\tau(\omega_c)}\cos\theta)}\frac{\sin^2\theta}{2\alpha}. \tag{3.7}$$

The resulting emissivity is shown in Fig. 3.4 as a function of radiation angle and frequency. Note the sharp contrast of emissivity across the region boundaries. The edge at the critical frequency corresponds to the OTT from type-I hyperbolic to dielectric, while the border between region B and region C is not a transition between two optical topological

phases (i.e. metal, dielectric, hyperbolic), rather the limit of total internal reflection [38] of a dielectric medium.

3.3 Material examples

As an example of this behavior we present the thermal emission intensity [35] (normalized to blackbody at the same temperature, Eq. (3.2)) from sapphire (Al_2O_3) [19] in Fig. 3.5(b). For this calculation, we use experimentally measured dielectric permittivity [19] in the infrared spectral region (see Fig. 3.5(a)) where medium optical response changes from hyperbolic type-I to dielectric. To find out the parameters introduced in Eqs. (3.4) - (3.7), we numerically calculate the slope of ϵ_n and the value of ϵ_τ at the critical frequency. Near the OTT, the corresponding radiation energy goes down drastically showing good agreement with the theoretically calculated region boundaries (superimposed black dotted line). Furthermore, the thermal emission from all three regions is consistent with the theoretical prediction in Fig. 3.4.

As a second example, we consider another promising platform hexagonal Boron-Nitride (h-BN) [20] for optical applications. In this material [21], $\epsilon_{\rm n}$ changes its sign at the frequency $\omega = 818.94\text{cm}^{-1}$ as shown in Fig. 3.5(c), corresponds to the OTT described in this article. As expected, in the vicinity of the transition, the radiated energy (Fig. 3.5(d)) diminishes strikingly corresponding to region B of the theoretical profile described in Eq. (3.3).

This feature of reduced thermal emission is not limited solely to natural media. Metamaterials with metal-dielectric periodic structure also show the same behavior. Consider GaAs based composites, which are well known and commonly used platforms due to their semiconductor and photonic applications [41]. Using the effective parameter model introduced in Ref. [28, 42] for a heterostructure composed of periodic layer of InAlAs and doped InGaAs, we calculate the dielectric permittivity shown in Fig. 3.5(e) for 50% metal fill fraction. Within the frequency range of interest, ϵ_τ remains positive while $\epsilon_{\rm n}$ changes its sign and the corresponding thermal emission shown in Fig. 3.5(f) drops near the critical frequency. Comparing the numerical result with our theoretical model, given in Eqs. (3.3) - (3.7) (Fig.

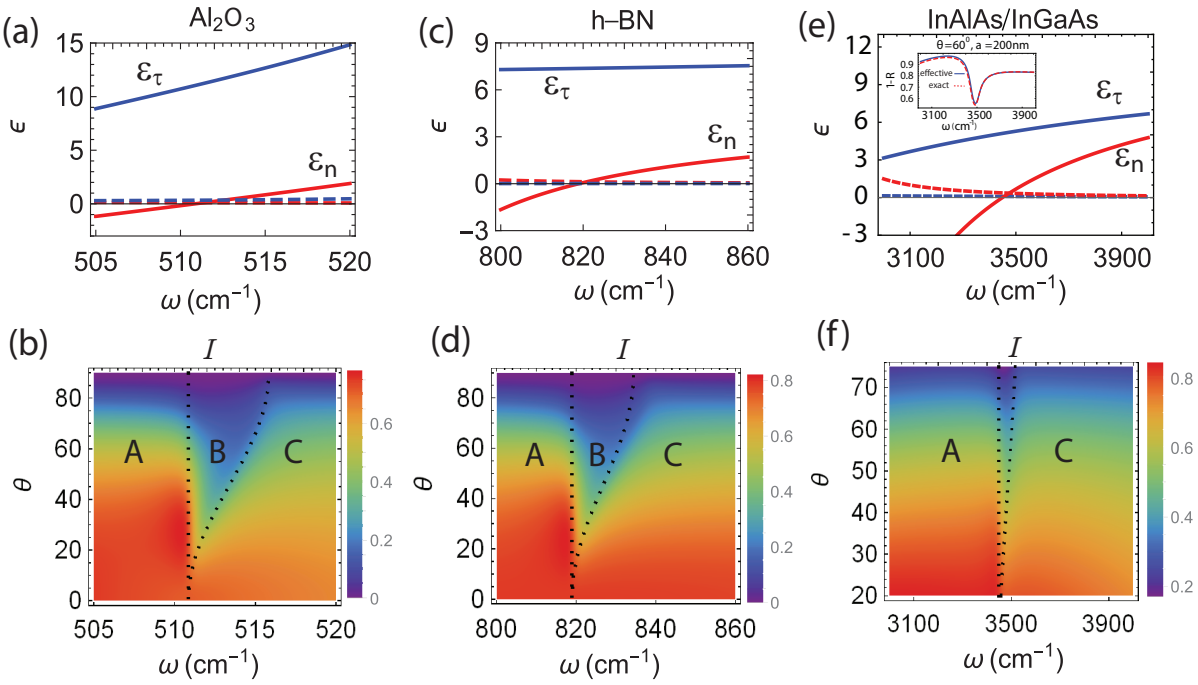

Figure 3.5. Dielectric permittivity for different materials in panels (a), (c), and (e) as a function of frequency. The solid (dotted) blue and red curves correspond to the real (imaginary) part of ϵ_τ and $\epsilon_{\rm n}$, respectively. The corresponding radiated (normalized to black body) thermal intensity are shown as a function of radiation angle and frequency in panel (b), (d), and (f). The theoretically predicted boundaries in black dotted lines are superimposed for each material and it shows that at the topological transition, all three have a general profile predicted by the model. Inset of panel (e) shows that the reflectivity calculated based on effective medium theory is highly accurate compared to the exact (e.g. $S-$ matrix based[39, 40]) method when the unit cell length of multilayer system is much smaller than the wavelength.

3.4), we clearly see the reduced emission that corresponds to region B from the theoretical prediction.

The asymmetric feature of the thermal emission happens within very narrow frequency range compared to the typical frequency scale of the permittivity variation as shown in Fig. 3.5. This justifies the use of linear model for material permittivity in Eq. (3.3). In fact, exact reflectivity (Fig. 3.5(e) inset[39, 40]) based on $S-$ matrix method for multilayer system yields emission pattern which is visually indistinguishable from that of Fig. 3.5(f), when the wavelength (2.5 μm - 3.3 μm) is larger than the unit cell length (e.g. 200 nm). Note the presence of region B in all three examples considered. Furthermore, the general asymmetric profile of reduced emissivity is in good agreement with the theoretical model in all the examples.

However, one can see visible discrepancies in the actual thermal emission profile compared with the theoretical model. In particular, the nonzero emission in region B, where the theory predicts zero emission, is due to the finite loss of the material. Frequency dependence of ϵ_n may also differ from our linear approximation. As a consequence, the boundary between region B and region C in h-BN deviates from the model.

3.4 OTT by metal-dielectric composite

The predicted behavior is not limited to specific metamaterials but is, in fact, common to all planar metal-dielectric composites. To justify the claim, we plot the optical phase diagram [32] for the entire class of planar conducting-dielectric periodic systems in Fig. 3.6. One can clearly see the transition (white line) from the hyperbolic to dielectric phase for predicted thermal emission. This transition is supported by all such heterostructures regardless of metal fill fraction.

The thermal emission near the OTT reduces drastically and both natural and composite materials show this behavior. Hence, the existence of the asymmetric feature should be experimentally observable and can be used as a tool to detect the OTT between type-I hyperbolic and dielectric phases.

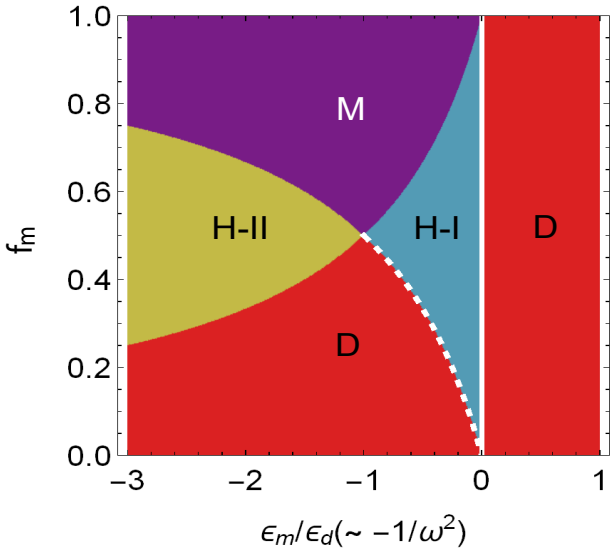

Figure 3.6. The "phase diagram" of metal-dielectric layered system as a function of metal fill fraction and frequency with false color showing the metallic, dielectric, and hyperbolic response of the composite. As a convenient measure of frequency, we choose the ratio of metal to dielectric permittivity which behaves as $-1/\omega^2$. The phase diagram shows all phases: anisotropic metal, anisotropic dielectric, hyperbolic type-I and hyperbolic type-II are labeled by M, D, H-I, and H-II, respectively. The transition for the zero thermal emission of $p-$ polarized light has been indicated by the dark white line at the boundary of H-I and D phases. Similar transition takes place when permittivity of metal is negative for $0 < f_m < 0.5$ shown in dotted white line. However, associated loss of such transition is too high to produce the zero emission feature for $p-$polarization.

Moreover, away from the OTT, the contribution from $s-$ polarized wave to the thermal emission is comparable to that of $p-$ polarized wave. However, near the OTT, the thermal emission intensity of $p-$polarized wave drops by approximately an order of magnitude while emissivity of $s-$ polarized light does not change significantly because ϵ_τ remains approximately constant at the OTT. Hence the predicted effects of thermal emission persist when both polarizations are taken into account. Thus, it is possible to build frequency-varying polarized thermal emitters using planar fabrication technology.

Finally, the interface can also support a surface wave. But, since surface waves have high momenta $k_\tau > k_0$, they would not couple to the far-field and hence will not change our result. However, the situation becomes very different in the case of near-field radiation. Exponential decay of the surface wave away from the interface affects the near-field radiation significantly which could reach beyond Planck radiation limit[32]. To generalize our result for the near-field radiation one has to include surface wave contribution in our model.

3.5 Summary

In conclusion, a theoretical description of far-field thermal radiation has been developed near an optical topological transition. Material examples consisting of both natural and composite media showed that our analytic approach is in good agreement with numerical results.

4. GHOST WAVE IN BIAXIAL MEDIA

This chapter has been partially reproduced from previous publications [43, 44].

In this chapter we show that ghost waves – a special class of nonuniform waves in biaxial dielectric media that are not present in uniaxial or isotropic classes. Moreover, interactions between such hybrid waves can lead to exact frequency degeneracies in guided modes. These degeneracies are a new way of controlling mode interactions with a broad range of potential applications, such as integrated waveguides, nonlinear optics, and optical sensing.

4.1 Biaxial medium

Optical biaxial media are such that there are no two equivalent crystallographic directions that could be chosen which makes the media different from uniaxial or isotropic media where such equivalent directions exist. Thus, optical permittivities of biaxial crystal along the principal dielectric axes are all different from each other ($\epsilon_x \neq \epsilon_y \neq \epsilon_z$).

In contrast with the uniaxial media, there can be two or more optically equivalent directions chosen in a plane perpendicular to an axis having threefold (rhombohedral [45]), fourfold (tetragonal [46]) or sixfold (hexagonal [47]) symmetry. If the axis is along z direction and one dielectric axis coincides with it, then $\epsilon_x = \epsilon_y \neq \epsilon_z$. Contrary to that, the directions of the principal dielectric axes in the biaxial media may (orthorhombic, monoclinic) or may not (triclinic) be determined by the crystallographic symmetry. In the case of orthorhombic symmetry, all three principal dielectric axes are aligned with the crystallographic orientation. However, for triclinic system, the directions of all three axes are dictated by the frequency of light passing through.

4.2 Dispersion

In general, a plane wave propagating in biaxial media is determined by the dielectric tensor ϵ_{ij} that links the displacement field and the electric field as follows

$$D_i = \sum_j \epsilon_{ij} E_j; \quad \text{where} \{i, j\} = \{x, y, z\}. \tag{4.1}$$

If the coordinate axes of the system coincides with the principle dielectric axes, then in transparent media, $\epsilon_{ij} = 0$ for $i \neq j$ and the above relation simplifies to $D_i = \sum_i \epsilon_{ii} E_i$. Inside such biaxial media, a monochromatic plane wave with frequency ω and momentum vector $\vec{q} = (q_x, q_y, q_z)$ satisfies the following wave equation

$$\vec{D} + \frac{\vec{q} \times \vec{q} \times \vec{E}}{k_0^2} = 0 \tag{4.2}$$

where k_0 is the free space momentum. Using vector algebra and material properties, the above equation can be reduced to

$$k_0^2 \epsilon_i E_i - |q|^2 E_i + (\vec{E} \cdot \vec{q}) q_i = 0. \tag{4.3}$$

Equation (4.3) being linear and homogeneous in E_x, E_y, and E_z, can be solved for nonzero values if the associated determinant is zero, which yields a quartic dispersion equation

$$\begin{aligned} &\epsilon_x \epsilon_y \epsilon_z k_0^4 + |q|^2 (\epsilon_x q_x^2 + \epsilon_y q_y^2 + \epsilon_z q_z^2) \\ &- \Big[q_x^2 \epsilon_x (\epsilon_y + \epsilon_z) + q_y^2 \epsilon_y (\epsilon_z + \epsilon_x) + q_z^2 \epsilon_z (\epsilon_x + \epsilon_y) \Big] k_0^2 = 0. \end{aligned} \tag{4.4}$$

Notice the absence of both cubic and linear terms from eq. (4.4). This biquadratic equation corresponds to a wavevector surface having two shells in the momentum space as shown in Fig.(4.1). In other words, for each direction, there are two propagating modes supported by biaxial media. If any two (q_x, q_y) of the momentum components are given, then Eq.(4.4) can be solved for the third component [48]

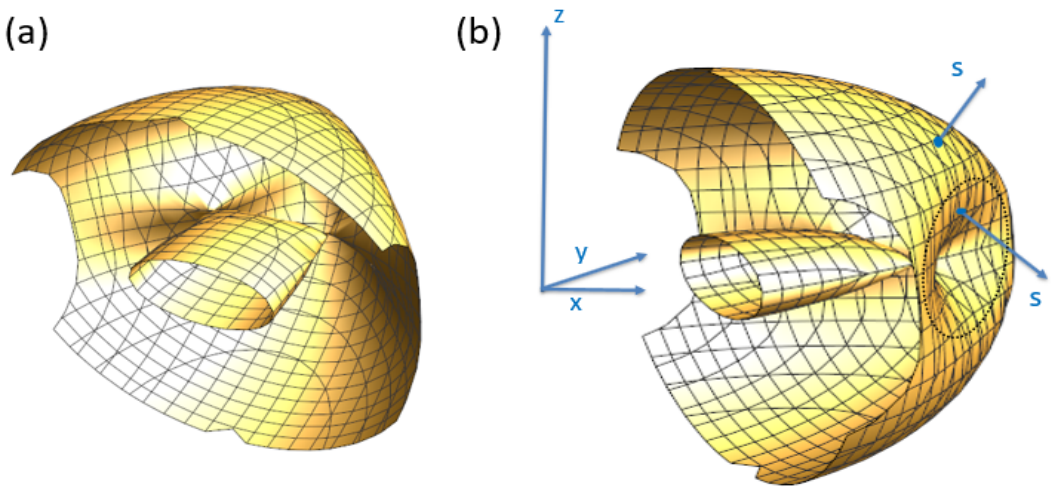

Figure 4.1. 3D momentum space of biaxial medium shown from inside (a) and outside (b) the shell. Note that the presence of Diabolic points (DPs) on $q_z = 0$ plane which create cusps in the 3D momentum space where the Poynting vectors (s) have a negative (z) component correspond to negative index mode (NIM)[49]. On the contrary, outside the cusp regime, the Poynting vector creates an acute angle with the momentum vector that corresponds to a positive index mode (PIM). The black dotted ring shown in panel-(b) corresponds to the boundary between PIM and NIM where they annihilate each other.

$$
\begin{aligned}
q_z^{\pm} =& \frac{1}{\sqrt{2}} \Bigg\{ (\epsilon_x + \epsilon_y) k_0^2 - \left(1 + \frac{\epsilon_x}{\epsilon_z}\right) q_x^2 - \left(1 + \frac{\epsilon_y}{\epsilon_z}\right) q_y^2 \\
& \pm \Bigg[\left((\epsilon_x - \epsilon_y) k_0^2 + \left(1 - \frac{\epsilon_x}{\epsilon_z}\right) q_x^2 - \left(1 - \frac{\epsilon_y}{\epsilon_z}\right) q_y^2 \right)^2 \\
& + 4 \left(1 - \frac{\epsilon_x}{\epsilon_z}\right) \left(1 - \frac{\epsilon_y}{\epsilon_z}\right) q_x^2 \, q_y^2 \Bigg]^{\frac{1}{2}} \Bigg\}^{\frac{1}{2}} .
\end{aligned}
\tag{4.5}
$$

However, for wave propagation along any principal dielectric plane (i.e. $q_z = 0$), the biquadratic dispersion (Eq. 4.4) turns into two independent quadratic equations representing TE and TM modes as shown in Fig. (4.2). Polarizations of these independent modes are such that one of the field components is zero. Whereas, in general, biaxial media support hybrid mode consisting of all nonzero field components [48]. Moreover, the isofrequency contours separate different regimes of momentum space as indicated in Fig. (4.2)(b).

The isofrequency contours of biaxial media have four singular points of self-crossing known as Diabolic points (DPs); Of which, all of them are located on the crystallographic

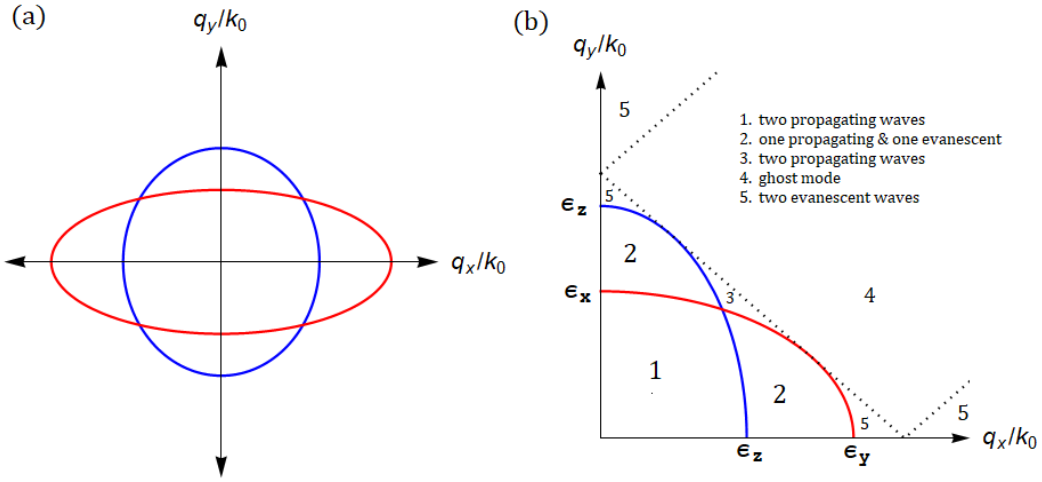

Figure 4.2. (a) Isofrequency contours $\frac{q_x^2}{\epsilon_y} + \frac{q_y^2}{\epsilon_x} = k_0^2$ (red) and $q_x^2 + q_y^2 = \epsilon_z k_0^2$ (blue) supported by biaxial crystal with $\epsilon_x < \epsilon_z < \epsilon_y$. Note the singularities induced by the self-crossing of the isofrequency wavevector at plane $q_z = 0$. While those singular points form two principal optical axes through the origin of the momentum space, the isofrequency contours correspond to the region boundaries in the phase space. Different regimes can be mathematically classified by the values of the q_z as indicated by the magnified view of the momentum space in panel (b). Out of five different regimes-"3" and "4" are unique in biaxial crystal while regimes-"1", "2", and "5" are similar to uniaxial media.

plane and the optical axes can be found by connecting two opposite DPs through the origin of the momentum space. The directions of optical axes are the only ones for which the wavevector has one magnitude. If any two components of the dielectric permittivity are equal, then, two optical axes are aligned with each other and pointed towards the crystallographic axis resulting in uniaxial media.

For biaxial media with permittivity $\epsilon_x < \epsilon_z < \epsilon_y$, all four DPs are on $q_z = 0$ plane which connect several regimes of the momentum space. Mathematically, those regimes can be identified by the solution of q_z (Eq. 4.5) as shown in Fig. 4.2(b). While regimes -"1", "2", and "5" are similar to uniaxial media, regimes -"3" and "4" uniquely differentiate the biaxial crystal from the uniaxial. In regime-"1", both q_z are real but the corresponding ray directions are different resulting in birefringence. However, in regime-"2", one of the modes is an evanescent type resulting in unimodal propagation. Finally, regime-"5" does not allow

any propagating mode within biaxial media indicating that both q_z are imaginary and the associated modes decay exponentially with distance.

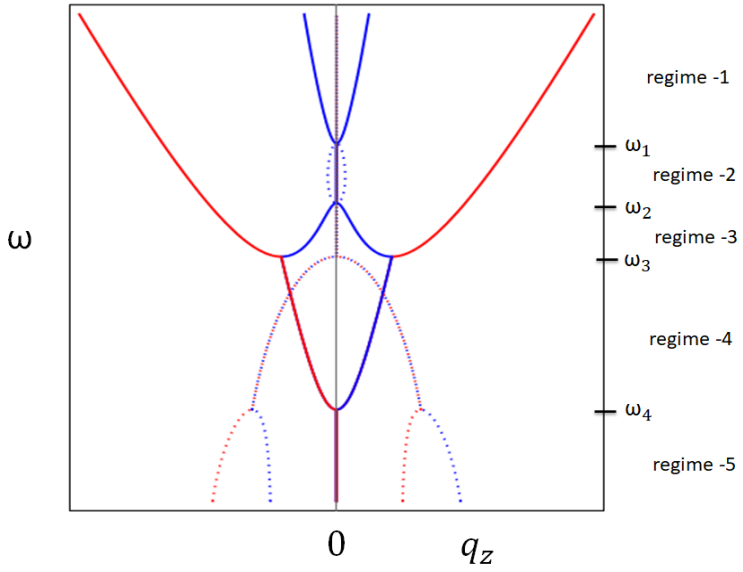

Figure 4.3. Dispersion diagram of biaxial media as a function of q_z (q_x and q_y are fixed) where solid and dotted lines correspond to real and imaginary parts of the frequency, respectively. Note that, the operating regimes indicated in the frequency scale are akin to that of the momentum space (Fig. 4.2 b) whereas the region boundaries are marked by ω_i.

Contrary to that, in regime-"3", even though both modes ($q_z^{\pm}$) are the propagating type, their difference ($\Delta q_z = q_z^+ - q_z^-$) decreases with the increase of q. This behavior is due to the presence of an anomalous dispersion (i.e., $\frac{\partial \omega}{\partial q_z} < 0$) resulting in the NIM [50] supported by biaxial media. To show these nontrivial dynamics we plot $\omega(q)$ as a function of q_z in

Fig. (4.3) where different regimes of operations are indicated in the frequency scale and the region boundaries are defined as

$$\begin{aligned}
\omega_1 &= c\sqrt{\frac{q_x^2}{\epsilon_y}+\frac{q_y^2}{\epsilon_x}},\\
\omega_2 &= c\sqrt{\frac{q_x^2+q_y^2}{\epsilon_z}},\\
\omega_3 &= \frac{c}{\epsilon_y-\epsilon_x}\left(q_x\sqrt{1-\frac{\epsilon_x}{\epsilon_z}}+q_y\sqrt{\frac{\epsilon_y}{\epsilon_z}-1}\right),\\
\omega_4 &= \frac{c}{\epsilon_y-\epsilon_x}\left(-q_x\sqrt{1-\frac{\epsilon_x}{\epsilon_z}}+q_y\sqrt{\frac{\epsilon_y}{\epsilon_z}-1}\right).
\end{aligned} \tag{4.6}$$

Note the transition from regime-"2" to regime-"3" where one biaxial mode evolves continuously but the other one transforms nontrivially from imaginary to real with $\frac{\partial\omega}{\partial q_z} < 0$. Moreover, such nontrivial evolution turns both modes to annihilate each other at ω_3 where all higher order dynamics of biaxial modes have equal magnitudes but opposite phases. In the momentum space (see fig.4.2(b)), this condition is indicated by the black dotted line touching TE and TM isofrequency contours. Beyond the tangent bifurcation, dynamics of the system modes enter into complex phase space resulting in ghost wave(s): a qualitatively new hybrid wave supported by regime-"4" of the phase space where propagating constant pair ($q_z^{\pm}$) is complex conjugate to each other while the other two (q_x, q_y) are real. Finally, in regime-"5" both q_z are imaginary.

Akin to different phases in the momentum space, biaxial crystals support qualitatively different types of electromagnetic waves. In the next section, we will discuss such waves in the realm of parallel plate waveguides with biaxial media as a core.

4.3 Parallel plate waveguides with biaxial core

Consider a parallel plate optical waveguide system as shown in the schematic in Fig. 4.4 (a) with biaxial core inside. Since the refractive indices of the core region are direction-dependent, careful attention is given to the value of the permittivities and the orientation of the core. For structural simplicity, we use isotropic cladding surrounding the core region

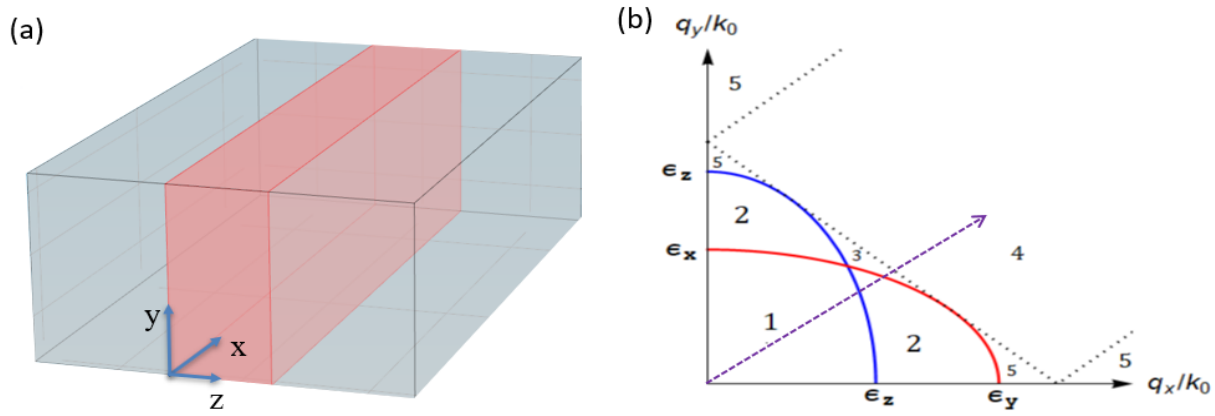

Figure 4.4. (a) Parallel plate waveguide with biaxial core (red) and isotropic cladding (water blue) with permittivities $\epsilon_{biaxial} = \text{diag}(2, 30, 6)$ and $\epsilon_0 = 7.2$, respectively. (b) Schematics of the momentum space of biaxial core where momenta (q_x, q_y) correspond to that of the tangential components of the guided modes which are being changed in our calculation along the dotted purple line with slope m = 0.4; Note that the orientation of the crystal would remain same throughout the thesis except section-4.10 where the necessity of the change in the orientation is discussed in details.

and assume that the interface of the system is infinitely extended. Moreover, the thickness of the cladding is assumed to be infinite whereas the core has finite width as shown in the schematic.

The orientation of the biaxial crystal is such that the plane containing maximum and minimum values of the permittivities is parallel to the interface plane. Whereas, the normal direction to the interface has permittivity between maximum and minimum. Note that to excite guided modes supported by different regimes of the momentum space, the refractive index of the isotropic medium is chosen such that $\epsilon_x < \epsilon_z < \epsilon_0 < \epsilon_y$.

Dispersion of those modes is shown in Fig. 4.5(a). Note the presence of all five regimes supported by the system. Modes within regime-"2" are well separated from each other in the frequency scale and orthogonal as if the core is isotropic media. Contrary to that, in regime-"3", the interaction is nonzero. Moreover, the interactions vary as a function of frequency and momentum which result in both mode degeneracies and repulsions (details of mode interactions are discussed in Secs. 4.7 - 4.9). Finally, in regime-"4", due to complex conjugation characteristic of momentum component q_z, mode profile within biaxial core

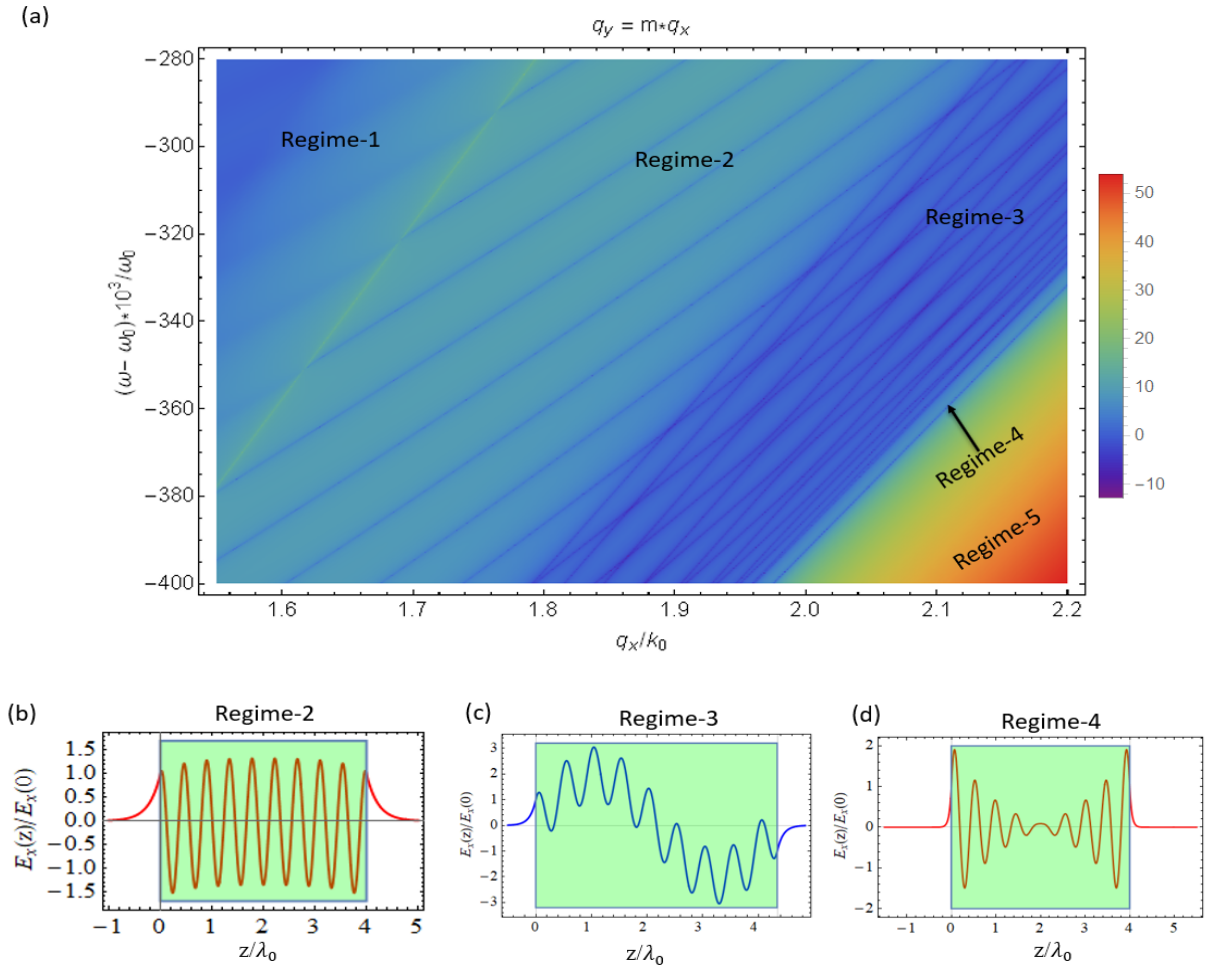

Figure 4.5. (a) Schematics of 2D plot of the determinant of transfer matrix [39, 48] representing isotropic-biaxial-isotropic system where the false color indicates the value of the determinant in natural log scale. The deep blue lines representing zero of the transfer matrix correspond to the guided modes of the system. Note the presence of all five regimes which are inherent to biaxial crystal, supported by the system. Among all five regimes, regime-"1" corresponds to light scattering which remains above the light (yellow) line while regimes-"2"-"4" support guided modes. Field profiles associated with three qualitatively different guided modes are shown in panels (b)-(d). Finally, due to the imaginary nature of the propagating constants (q_z), regime-"5" does not support any guided mode.

contains both oscillating and exponential decaying fields known as "ghost" wave [50] as shown in Fig. 4.5(d). In the next section, we will discuss more details about ghost waves and their excitation mechanism.

4.4 Ghost waves

Ghost wave is a special class of non-uniform electromagnetic waves [51] inside a biaxial anisotropic medium that combines the properties of propagating and evanescent fields. The designation "ghost" [50] refers to the fact that these waves are created in tangent bifurcations that annihilate pairs of positive and negative index modes and represent the optical analogue of the "ghost orbits" in the quantum theory of non-integrable dynamical systems [52].

Although ghost waves can be generally excited in a variety of device geometries and material platforms, a simple prototypical realization would be its excitation as a surface wave but the conclusion will hold in general for any arbitrary ghost waves.

4.5 Ghost surface waves

Ghost surface waves are a special class of Dyakonov surface waves [53] that can be confined at the interface between biaxial and isotropic medium with permittivity ϵ_0. Analogous to conventional Dyakonov waves as shown in Fig. 4.6(a), ghost surface waves decay exponentially away from the interface in the isotropic material. However, inside the biaxial medium, they act differently: in addition to the exponential decay they also show oscillations (see Fig. 4.6(b)).

If the z direction points along the interface normal, and the y direction is chosen such that $\epsilon_x < \epsilon_y$, then one of the conditions for the existence of the surface wave is [48]

$$\epsilon_x < \epsilon_z < \epsilon_0 < \epsilon_y \tag{4.7}$$

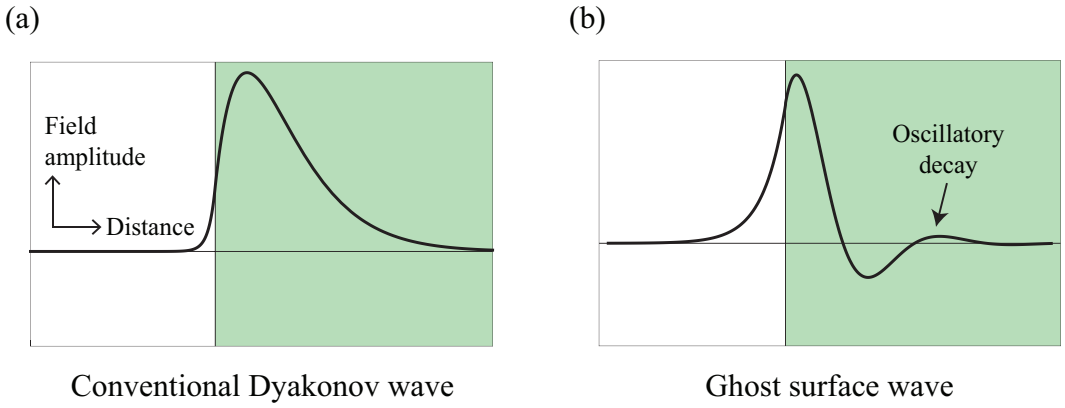

Figure 4.6. Surface waves that can be excited at the interface of a biaxial (green) and an isotropic (white) dielectric media can be of two distinct classes: (a) conventional Dyakonov waves and (b) ghost surface waves. Among these, only ghost surface waves decay with oscillations inside the biaxial medium.

Moreover, the tangential components of the wavevector (q_x, q_y) have to satisfy the surface wave dispersion equation [48]

$$\begin{aligned}
&\kappa_0(\kappa_+ + \kappa_-)\left\{\frac{\epsilon_x\epsilon_y}{\epsilon_0}\left[\left(\frac{\omega_s}{c}\right)^2 - \frac{q_x^2}{\epsilon_y} - \frac{q_y^2}{\epsilon_x}\right] - \kappa_+\kappa_-\right\} \\
&\quad + \kappa_+\kappa_-\left[(\epsilon_x+\epsilon_y)\left(\frac{\omega_s}{c}\right)^2 - \frac{\epsilon_0+\epsilon_x}{\epsilon_0}q_x^2 - \frac{\epsilon_0+\epsilon_y}{\epsilon_0}q_y^2\right] \\
&\quad + \left\{\frac{\epsilon_x\epsilon_y}{\epsilon_0}\kappa_0^2\left[\left(\frac{\omega_s}{c}\right)^2 - \frac{q_x^2}{\epsilon_y} - \frac{q_y^2}{\epsilon_x}\right] - \kappa_+^2\kappa_-^2\right\} = 0
\end{aligned} \tag{4.8}$$

where ω_s corresponds to the single interface resonance frequency for the surface wave. Here, the fields of the surface wave decay evanescently within the dielectric side with a decay coefficient

$$\kappa_0 = \sqrt{q_x^2 + q_y^2 - \epsilon_0\left(\frac{\omega_s}{c}\right)^2}. \tag{4.9}$$

The corresponding decay coefficients within the biaxial side can be found by solving eq. (4.4)

$$\kappa_{\pm} = iq_z = \frac{1}{\sqrt{2}}\Bigg\{ \left(1+\frac{\epsilon_x}{\epsilon_z}\right) q_x^2 + \left(1+\frac{\epsilon_y}{\epsilon_z}\right) q_y^2 - (\epsilon_x+\epsilon_y)\left(\frac{\omega_s}{c}\right)^2 \pm \Bigg[\left((\epsilon_x-\epsilon_y)\left(\frac{\omega_s}{c}\right)^2 + \left(1-\frac{\epsilon_x}{\epsilon_z}\right) q_x^2 - \left(1-\frac{\epsilon_y}{\epsilon_z}\right) q_y^2\right)^2 + 4\left(1-\frac{\epsilon_x}{\epsilon_z}\right)\left(1-\frac{\epsilon_y}{\epsilon_z}\right) q_x^2\, q_y^2 \Bigg]^{\frac{1}{2}} \Bigg\}^{\frac{1}{2}}. \tag{4.10}$$

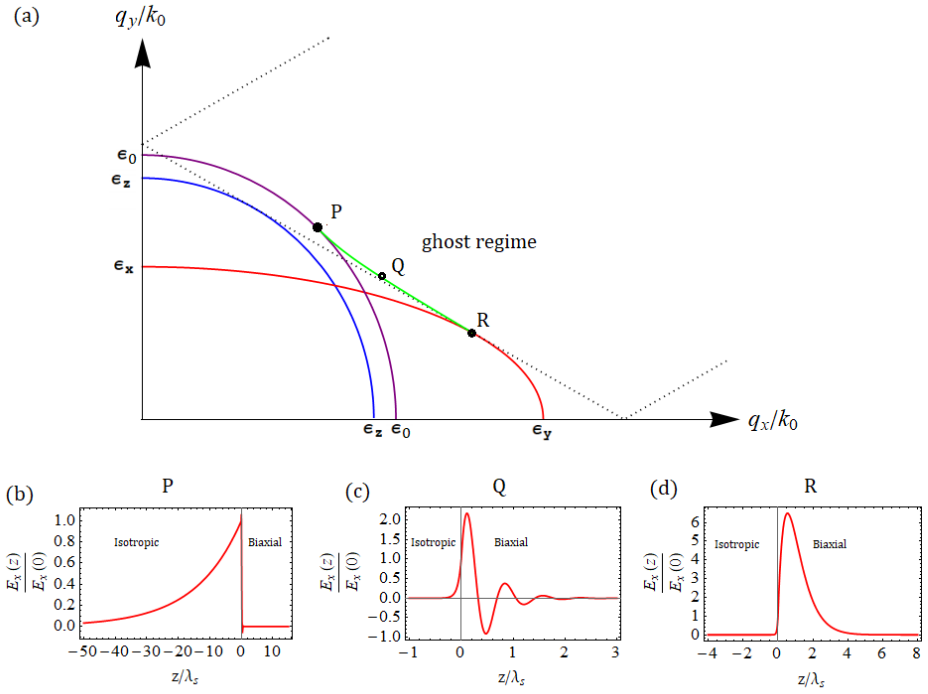

Figure 4.7. Panel (a) shows isofrequency contour of ghost surface waves (green) excited at the interface of a biaxial (red and blue) and an isotropic (purple) dielectric media. Panels (b)-(d) correspond to the field plots at different points on the ghost surface wave dispersion. Note the surface wave dispersion lies within the ghost regime of the momentum space where the two extreme points are denoted by P and R. At those extreme limits, this hybrid type surface wave evolves into conventional Dyankonov surface wave. At point P, where the dispersion touches the isotropic medium contour, the new surface wave penetrates deep within the isotropic medium. On the other hand, at point R, the surface wave tail extends within the biaxial medium which could be used for long-range sensor applications.

Note, that in the uniaxial limit $\epsilon_x \to \epsilon_z$, $\kappa_{\pm}$ are purely real, and thereby the mode reduces to the well-known Dyakonov surface wave at the interface between an isotropic medium and a

uniaxial dielectric[53, 54]. Since point R in Fig.(4.7a) of the biaxial medium behaves similar to a uniaxial medium, at that point, ghost mode evolves into conventional Dyakonov surface as shown in Fig. (4.7d).

In general, Eq. (4.10) asserts that $\kappa_\pm$ are complex conjugates of each other. For the resulting surface wave ($\mathrm{Re}[\kappa_\pm] > 0$) to belong to the ghost class, as opposed to the conventional Dyakonov class (see Fig. 4.6(a)), the imaginary parts of $\kappa_\pm$ have to be nonzero:

$$\mathrm{Im}[\kappa_\pm] \neq 0, \tag{4.11}$$

so that the field amplitudes exhibit oscillations in addition to the evanescent decay (see Fig. 4.6(b)). As will be shown in the next section, this oscillatory nature of ghost surface waves leads to exact frequency degeneracy when two such waves are allowed to interact.

4.6 Ghost induced degeneracies

Lifting of energy degeneracies of a composite system through interaction among its constituents is a generic theme of all physical systems - from splitting of $s-$orbital energies of two hydrogen atoms [55] to two surface modes in a plasmonic waveguide [40, 56] in the metal-insulator-metal configuration. The universal feature present in all of the manifestations of this phenomenon is the direct relation of the amount of splitting with the interaction length.

The generic feature of interaction lifting degeneracy also shows a direct monotonic relation between the amount of splitting and the interaction length. In this work, we challenge this notion and show that degeneracies may persist even though there is a nonzero interaction length. We demonstrate this behavior in the case of recently discovered ghost waves [48, 50].

4.7 Ghost coupling: Interaction between Ghost modes

Consider two ghost surface waves excited on either side of a lossless biaxial slab which is surrounded by the same isotropic lossless dielectric material on both sides, as shown in

Fig. 4.8(a). Because of the finite slab thickness L, the fields of the two surface waves would spatially overlap.

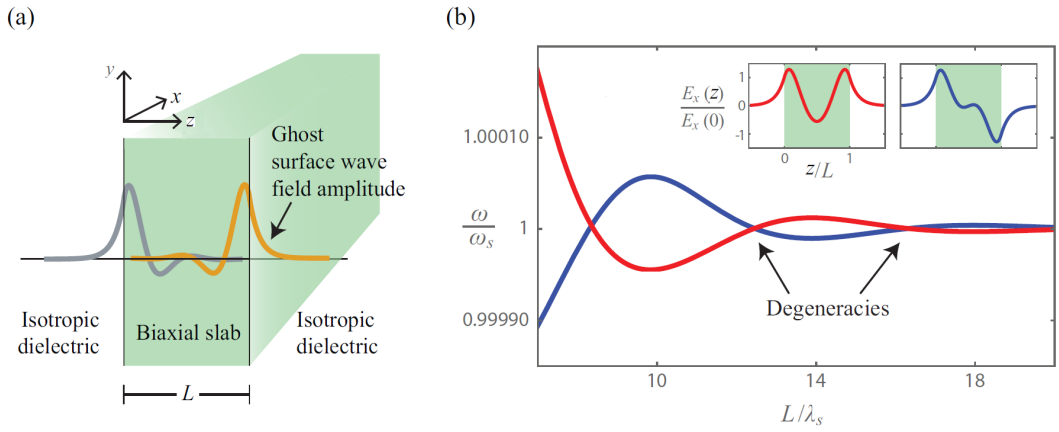

Figure 4.8. Oscillatory character of ghost surface wave leads to vanishing coupling between guided modes and yields frequency degeneracies. (a) Waveguide schematics show a biaxial core (of $NaNO_2$, with permittivity tensor $\bar{\bar{\epsilon}}_{\text{slab}} = \text{diag}(1.806, 2.726, 1.991)$) of thickness L with an isotropic dielectric surrounding (of permittivity $\epsilon_0 = 2.01$) along with the field amplitudes of the two uncoupled ghost surface waves. Note the oscillatory nature of the fields inside the biaxial medium. (b) Behavior of mode splitting as a function of the slab thickness L, normalized to single interface ghost resonance wavelength $\lambda_s = 2\pi c/\omega_s$, shows that for certain interaction lengths the two modes have exact degenerate frequencies. Insets show the field profiles of the symmetric (red line) and anti-symmetric (blue line) slab eigenmodes.

These individual surface states would then form the basis of the symmetric and anti-symmetric combination for the slab eigenmodes. Both these eigenmodes have their frequencies asymptotically converge to the single interface mode frequency ω_s as $L \to \infty$ as shown in Fig. 4.8(b). However, their variation for finite L shows oscillations, as opposed to conventional monotonic behavior in other prototypical systems. Additionally, note that for certain slab thicknesses, the frequency difference between the two eigenmodes is exactly zero. These frequency degeneracies are attributed to the oscillatory character of ghost surface waves which leads to vanishing coupling between the two guided modes.

To illustrate this result, consider the transmission through such a biaxial slab as a function of frequency and slab thickness (see Fig. 4.9 (a)). For an incident evanescent field, the ghost resonances amplify the field inside the biaxial slab, much similar to the evanescent field amplification in negative index material [57]. However, as slab thickness is varied, the

two resonance frequencies intertwine around each other, leading to degeneracies at regular intervals.

To contrast this behavior with that of usual surface waves, consider replacing the biaxial slab with an ideal lossless metal so that the interaction between the two surface plasmon modes on either side of the slab splits the system eigenmodes on the frequency scale. Fig. 4.9(b) shows the corresponding transmission plot as a function of the slab thickness. Notice the transmission corresponding to two plasmon resonance frequencies monotonically approach each other, asymptotically converging to the single interface resonance frequency ω_s, without showing any frequency degeneracy along the way.

In the next section, we employ coupled-mode theory [40, 58], a standard perturbation technique widely used for explaining mode interactions in waveguides, in order to capture the essence of "ghost coupling" presented in this section upto the first order.

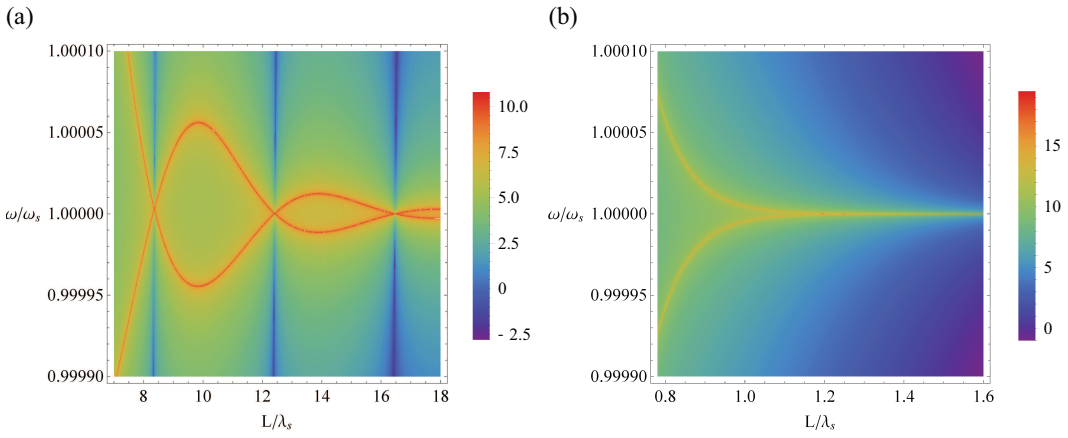

Figure 4.9. Transmission through a biaxial slab (shown by false color in *log* scale), as a function of frequency and slab thickness, shows the occurrence of ghost resonances. For certain slab thicknesses, these resonances occur at the same frequency. Here the system consists of a $NaNO_2$ biaxial slab surrounded by an isotropic dielectric with permittivity $\epsilon_0 = 2.01$. Since the incident field is evanescent (the transverse wavevector components $(q_x, q_y) \simeq (0.793, 1.182)$ in units of ω_s/c), a prism coupler may be used, which does not alter the results qualitatively. Panel (b) shows the transmission through a metallic slab for the same setting with a permittivity of -2 surrounded by air.

4.8 Coupled-mode analysis

The physical origin of ghost coupling can be explained within the framework of perturbation theory, where the interaction among the elements of a composite system can be described, to first order, by a term that is linear in the interaction potential. For example, for the case of two hydrogen atoms considered at the beginning of this paper, let $\|\psi_1\rangle$ and $\|\psi_2\rangle$ denote their wavefunctions when they are not interacting with each other. If they are brought nearby and allowed to interact through a potential V, then the amount of energy splitting can be approximated [59] by $\langle\psi_1\|V\|\psi_2\rangle$.

A similar perturbation technique, known as coupled-mode theory, describes optical interaction between modes in waveguides [58, 60, 61]. This approach offers a good qualitative picture of the nature of mode interaction without the need to solve for fields of the entire system. In cases of moderate interaction, it also yields good quantitative estimates for power exchange, transfer distance, frequency splitting, etc.

Mathematically, the potential V for our system can be described by a permittivity tensor $\overline{\overline{\epsilon}}(\mathbf{r}) = \overline{\overline{\epsilon}}_{\text{slab}}$ for $0 < z < L$ and $\epsilon_0\overline{\overline{I}}$ otherwise ($\overline{\overline{I}}$ being the identity tensor). The general wave equation for the electric field $\mathbf{E}(\mathbf{r})$ is given by

$$\nabla \times (\nabla \times \mathbf{E}) = \omega^2 \mu_0 \, \overline{\overline{\epsilon}} \cdot \mathbf{E}. \tag{4.12}$$

where μ_0 is the permeability of free space. By dot multiplying Eq. 4.12 by $\mathbf{E}^*$, and integrating over a large volume where the fields vanish for large z or have contributions canceled from parallel surfaces due to system symmetry, one gets [58]

$$\omega^2 = \frac{\int (\nabla \times \mathbf{E}^*) \cdot (\nabla \times \mathbf{E}) \, dV}{\mu_0 \int \mathbf{E}^* \cdot \overline{\overline{\epsilon}} \cdot \mathbf{E} \, dV}. \tag{4.13}$$

Now the perturbation in the analysis comes from approximating the field $\mathbf{E}$ as a linear combination of the unperturbed fields:

$$\mathbf{E} = \sum_i a_i \mathbf{e}_i, \quad i = 1, 2. \tag{4.14}$$

Here, $\mathbf{e}_1$ is the field for the single interface system characterized by a permittivity tensor $\bar{\bar{\epsilon}}_1(\mathbf{r}) = \bar{\bar{\epsilon}}_{\text{slab}}$ for $z > 0$ and $\epsilon_0 \bar{\bar{I}}$ otherwise. Similarly, $\mathbf{e}_2$ corresponds to the system described by $\bar{\bar{\epsilon}}_2(\mathbf{r}) = \bar{\bar{\epsilon}}_{\text{slab}}$ for $z < L$ and $\epsilon_0 \bar{\bar{I}}$ otherwise. Since, each $\mathbf{e}_i$ represent fields at resonance, we have from Eq. 4.12

$$\nabla \times (\nabla \times \mathbf{e}_i) = \omega_s^2 \mu_0 \, \bar{\bar{\epsilon}}_i \cdot \mathbf{e}_i \tag{4.15}$$

where ω_s is the single interface resonance frequency. Equation 4.13 then turns into

$$\omega^2 = \omega_s^2 \frac{\mathbf{a}^\dagger \mathbf{K} \mathbf{a}}{\mathbf{a}^\dagger \mathbf{W} \mathbf{a}} \tag{4.16}$$

where

$$\begin{aligned} W_{ij} &= \int \mathbf{e}_i^* \cdot \bar{\bar{\epsilon}} \cdot \mathbf{e}_j \, dV \\ K_{ij} &= \int \mathbf{e}_i^* \cdot \bar{\bar{\epsilon}}_j \cdot \mathbf{e}_j \, dV \end{aligned} \tag{4.17}$$

and $\mathbf{a}$ is the vector containing the coefficients in Eq. 4.14. For a lossless system both $\mathbf{W}$ and $\mathbf{K}$ are Hermitian matrices. Their positive definiteness property also implies a real value for ω, as expected. Differentiating Eq. 4.16 with respect to $\mathbf{a}$ yields [58]

$$\omega^2 \mathbf{W} \mathbf{a} = \omega_s^2 \mathbf{K} \mathbf{a} \tag{4.18}$$

which gives stationary values for the system frequencies that can be readily determined from the unperturbed fields by solving

$$\det \left[\omega^2 \mathbf{W} - \omega_s^2 \mathbf{K} \right] = 0. \tag{4.19}$$

We apply coupled-mode theory to the case of biaxial slab ($\bar{\bar{\epsilon}}_{\text{slab}} = \text{diag}(\epsilon_x, \epsilon_y, \epsilon_z)$), and illustrate the ghost resonance frequencies in Fig. 4.10. We compare the resonance frequencies determined from Eq. 4.19 and by solving the full system as a function of slab thickness. In comparison with the exact calculation, although there are slight quantitative discrepancies for small slab thicknesses which is expected from a perturbation approach that assumes small interaction, the results match well in showing the oscillating behavior of the resonances. In particular, occurrence of degeneracies as well as the corresponding slab thicknesses are well

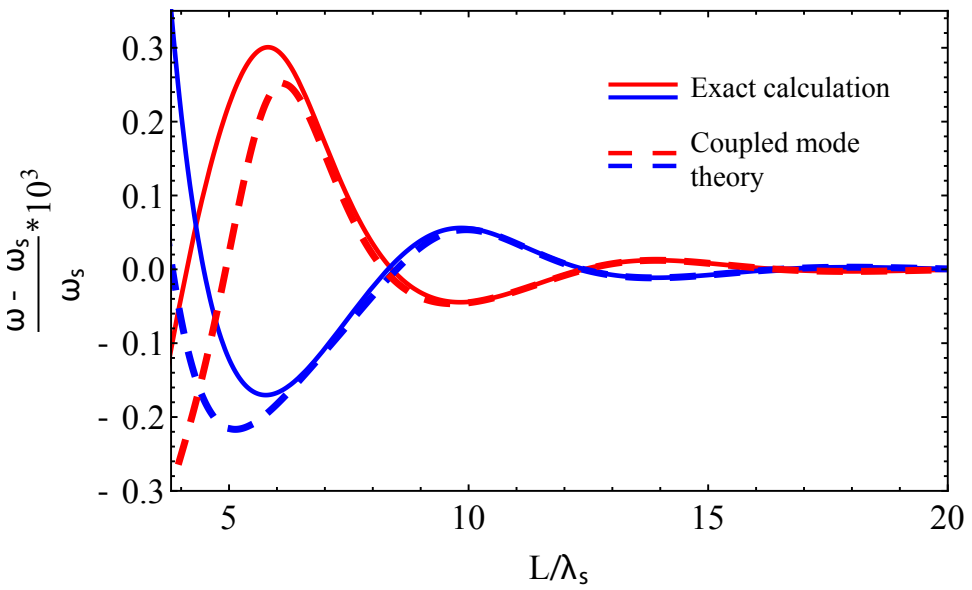

Figure 4.10. Application of a coupled-mode analysis for the system considered in Fig. 4.8 shows the frequency degeneracies and correctly predicts the corresponding slab thicknesses. Solid and dotted lines correspond to exact and couple mode results, respectively while different colors represent symmetric and anti-symmetric eigenmodes of the system.

predicted through this approach. Hence, couple mode analysis captures the essence of ghost wave interactions and shows that due to the characteristic oscillatory part of the ghost wave the effective coupling is zero at the degenerate points.

Furthermore, for the lossless biaxial system, it can be shown that **W** and **K** are real and symmetric. The condition for frequency degeneracy then becomes

$$\frac{K_{11}}{W_{11}} = \frac{K_{12}}{W_{12}}. \tag{4.20}$$

From Eq. 4.20 with the standard approximations of the coupled mode approach, for the slab thickness interval ΔL between successive degeneracies, we obtain

$$\Delta L \approx \frac{\pi}{|\mathrm{Im}(\kappa)|} \tag{4.21}$$

where κ is the propagation constant of ghost mode inside the biaxial slab. Eq. 4.21 indicates that ghost-induced degeneracies have periodicity which is half of the ghost wave oscillation

within biaxial medium. Furthermore, as evident from Fig. 4.10, the frequency at the degeneracy point ω_{degen} is not exactly ω_s, but approximately given by the coupled mode theory as

$$\omega_{\text{degen}} \approx \omega_s \sqrt{\frac{K_{11}}{W_{11}}}. \tag{4.22}$$

Note that degeneracy points do not necessarily occur at the single interface resonance frequency. The offset decreases as one goes to the asymptotic limit $L \to \infty$ where the modes get increasingly uncoupled.

So far we have discussed ghost-induced degeneracies which are the consequence of the oscillatory nature of the hybrid mode. Since ghost surface waves are special kind of hybrid mode, such level crossings are not limited to surface modes but are prevalent within propagating bands too. In the next section, we will discuss nonuniform electromagnetic mode-induced degeneracies supported by biaxial media.

4.9 Degeneracies in bulk modes

As pointed out in Sec. 4.2, biaxial media support different regimes of operations (see Fig. (4.3)). Consequently, isotropic-biaxial-isotropic system would also have several regimes of operation depending on the number of propagating constants of biaxial media and their corresponding types. In Sec. 4.3, different regimes are shown for waveguide mode dispersion as a function of frequency and momentum while the width of the biaxial core remains fixed. In this section, the evolution of the system modes is discussed by changing the core width while momentum remains fixed as shown in Fig. 4.11.

Regime-1 corresponds to scattering modes for our setup which in Fig. 4.11 (a) ties with higher frequency and out of our scope of analysis. We start our discussion from regime-2 in which, there is only one real propagating constant resulting in the monotonic evolution of the system mode. As evident from Fig. 4.11(a), successive modes in regime-2 are separated on the frequency scale with the variation of slab thickness. Moreover, the geometrical configuration of the system confirms that the parity of successive modes would have alternate symmetry (even and odd) with respect to the center of the system. Furthermore, within

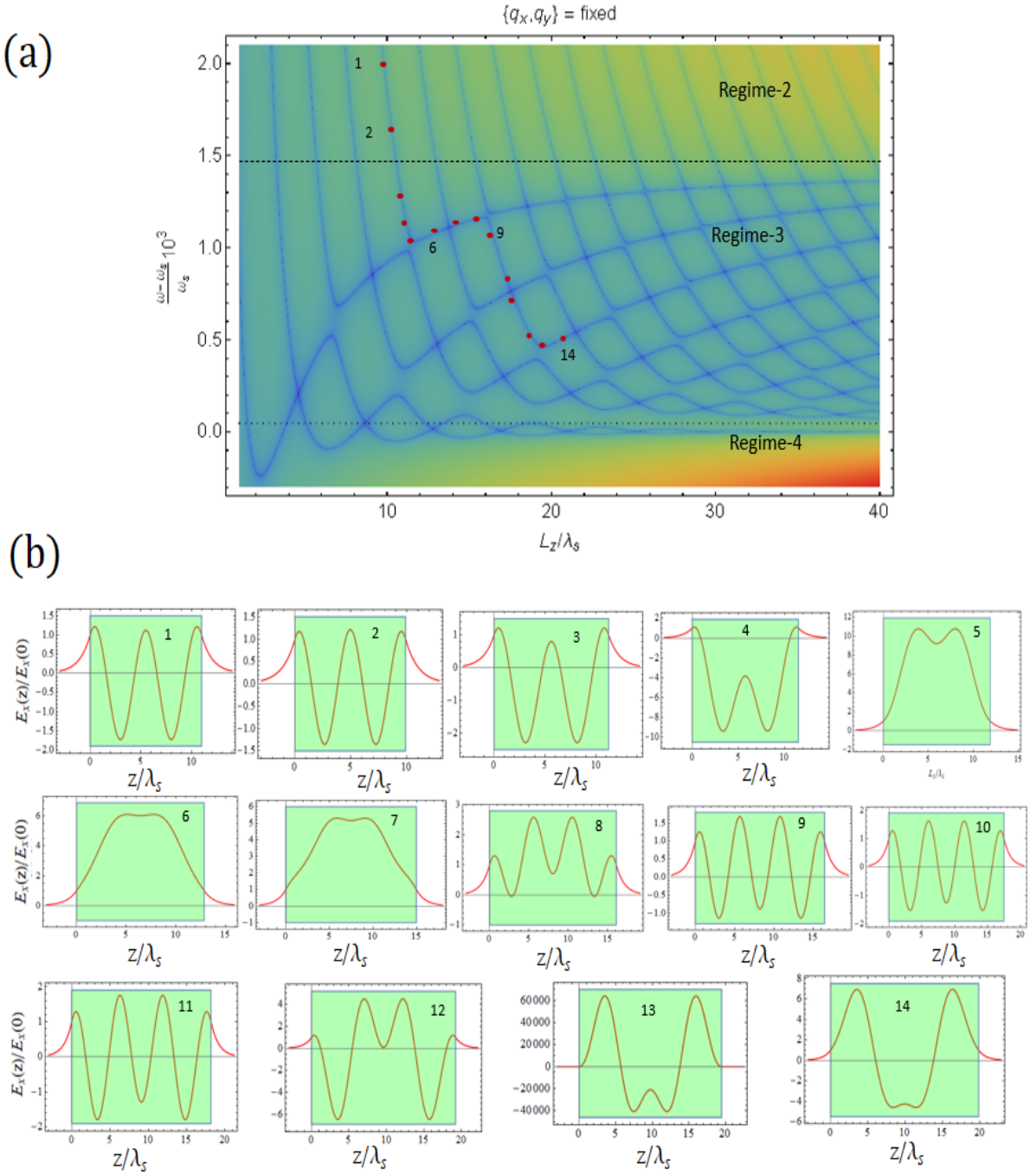

Figure 4.11. (a) Density plot of a matrix corresponds to isotropic-biaxial-isotropic system introduced in Fig.(4.8) where deep blue lines correspond to the guided modes of the system as a function of frequency and biaxial slab length. Note the mode evolution across different regimes where the boundaries between regimes are indicated by dotted black lines. Panel (b) shows field profiles associated with the evolution of system mode from regime-2 to regime-3. Note the change of the number of nodes within the field (wavefunction) profile while the symmetry remains unaltered.

regime-2, the number of nodes (zero crossings of the field) of a system mode remains fixed as shown by field plots in Fig. 4.11(b), and successive modes have one more or one less node.

However, nontrivial dynamics ($\frac{\partial \omega}{\partial q_z} < 0$) in regime-3 cause nearby modes with opposite parity (P) symmetry to couple with each other and form doublets. As the slab length is varied, constituents of each doublet cross at multiple points in a regular interval giving rise to degeneracies. While all the doublets are within the propagating band, the lowest pair in the frequency scale corresponds to the surface modes of the system.

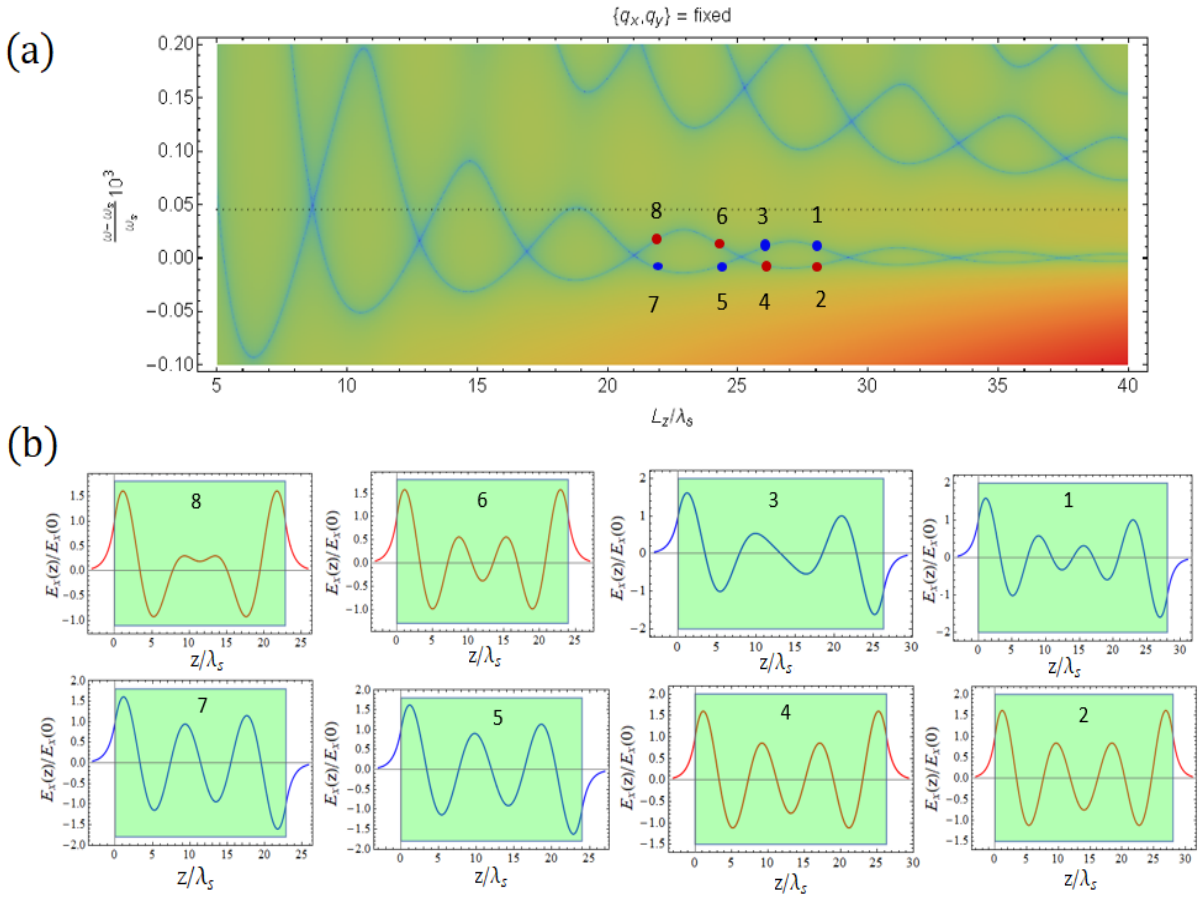

Figure 4.12. Evolution of ghost surface waves as a function of frequency and biaxial slab thickness shown in panel (a) and the corresponding field profiles ($\frac{E_x(z)}{E_x(0)}$) are shown in panel (b). Note the formation of crossing and anti-crossing junctions within the doublet whose constituents have opposite $P-$ symmetry. Moreover, since, surface waves are the lowest frequency modes, frequency maxima only correspond to anti-crossing junctions. As a consequence, change in no. of nodes takes places while the modes traverse through maxima in the frequency scale ($1\rightarrow$ 3, $6\rightarrow$ 8) whereas there are no such changes for the cases of frequency minima ($2\rightarrow$ 4, $5\rightarrow$ 7).

A physical explanation of doublet formation and degeneracies within the bulk band can be explained from the coupled mode theory introduced for ghost wave in Sec. (4.8). With the presence of nontrivial dynamics, the field components of the system modes start to overlap for finite slab thickness (L). With the change of L, the coupling between nearby modes is varied, and the contribution from all field components sums to zero at degenerate points.

Beyond a degenerate point, the DP-induced dynamics bring both modes of the doublet closer to the nearby doublets in the frequency scale. We call the points where each doublet is closest to the nearby doublets the anti-crossing points. After the anti-crossing point is reached, P symmetry-induced repulsion pushes both modes of the doublet closer together and away from neighboring doublets. As the slab width is varied, the crossing and anti-crossing patterns continue in regular intervals in such a way that each crossing point is surrounded by four nearby anti-crossing points and vice versa. Therefore due to the crossing and anti-crossing properties, the system doublets create a checkerboard pattern as shown in Fig.4.11 (a).

Notice the change in the number of nodes in the field profiles shown in Fig.4.11 (b). While the frequency of a system mode is within regime-2, adiabatic change of the biaxial length (or any other system parameter such as q) does not alter the wavefunction's node number. Contrary to that, in regime-3, the node number changes near anti-crossing points, which is one of the characteristic features of the junction supported by an isotropic-biaxial-isotropic system.

Changes in the number of nodes are also prevalent within regime-4 as shown in Fig. (4.12) where the system supports ghost waves. Since there is only one doublet in the ghost regime, each degenerate point within that doublet is surrounded by two anti-crossing points instead of four and vice versa. As the slab thickness is changed, the frequency maxima of the doublet correspond to anti-crossing junctions while the minima do not. Consequently, as evident by the field profiles shown in Fig. 4.12 (b), changes in the number of nodes take place while ghost surface modes traverse through the frequency maxima only. Note that the parity symmetry of the modes remains unaltered through evolution.

Finally, we conclude unusually that anisotropy introduced nontrivial dynamics give rise to a change in the number of nodes for the same mode. Moreover, scalar wavefunctions (in

electronic systems) remain well separated in the energy scale while the system goes through adiabatic perturbation. However, in optics, vectorial wavefunctions (field) under anisotropic (biaxial) potential form a checkerboard pattern consisting of frequency degeneracies and anti-crossing junctions as a function of system parameters (L, q or ω). This nontrivial behavior is due to the presence of a cusp regime("3") originating from the DP in biaxial media. In the next section, we will discuss NIM mode supported by the cusp regime.

4.10 Negative index mode

Since the discovery of left handed media (LHM) by Veselago[62], NIM becomes an exciting tropic for numerous theoretical studies and applications including superlens [57], negative pressure [63], higher harmonic generation [64], phase maching between different electromagnetic polarizations [65], dispersionless optical modes [66, 67], etc.

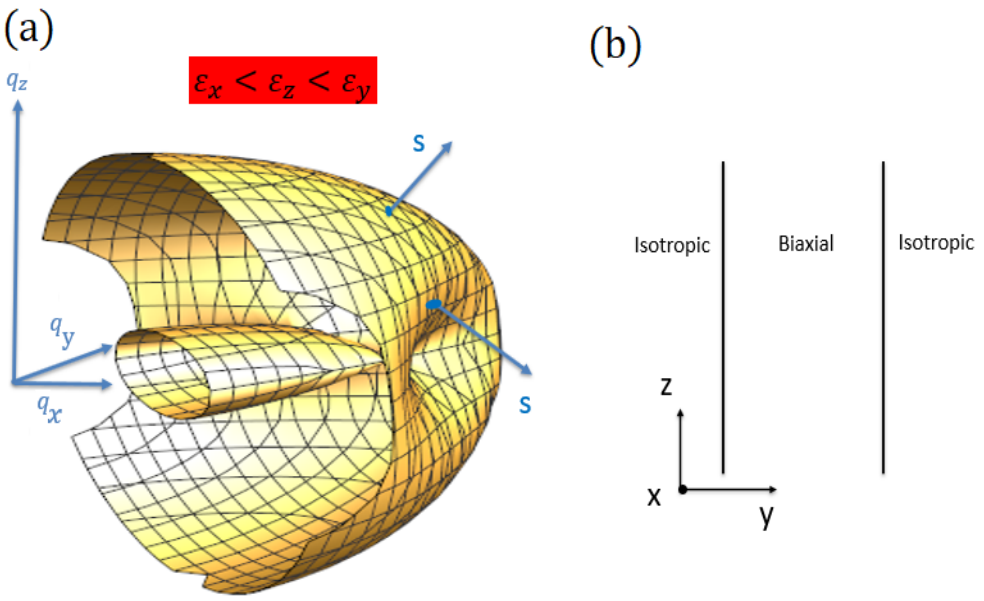

Figure 4.13. (a) 3D momentum space of biaxial crystal for $\epsilon_x < \epsilon_z < \epsilon_y$ where coordinate axes are parallel to the crystal axes. Note the presence of DP on the the x-y plane and negative component of pointing vector (s_z) within the cusp regime supported by the media. Panel (b) shows the Fabry-Perot cavity configuration where biaxial media is sandwiched between two isotropic dielectric in such a way that the "z" direction is along the interface.

Since LHM are not available in nature, researchers have turned themselves towards artificial approaches including but not limited to split ring resonators [68], metal-dielectric planar

composites [69, 70], photonic crystals [71], negative transmission lines [72] and their optical analogues [73] to obtain NIMs. However, due to the composite nature of the system, these approaches have their own drawbacks in design, fabrications, and applications.

In this regard, from their beginning, natural anisotropic crystal with in-build anomalous dispersion is drawing tangible attention for both linear and non-linear [74] optical applications. Recently, a planar dielectric slab geometry [49] with biaxial crystal has been theoretically proposed to achieve negative radiation pressure. However, due to the leaky nature of those modes, such a concept has yet to produce any lasing activity.

In the case of laser, media with anomalous dispersion [75] have been used in conjunction with Fabry-Perot cavity configuration. Here, anomalous dispersion compensates the intracavity stress [75] that optical modes suffer while traversing through the system. However, biaxial media, with nontrivial dynamics in the cusp regime offer a simple way to compensate for optical mode stressing while being used as part of the cavity.

In this section, we discuss the theoretical concept of a continuous wave laser using biaxial crystals. The cavity of the system is designed such that the biaxial media is placed in between two lossless isotropic dielectrics. Moreover, the dielectric permittivities of the isotropic cladding are chosen judicially such that each interface works as perfect reflector.

Since the DP of the biaxial crystal remains on the crystallographic plane, cusp regimes have all three momentum components which are nonzero. Subsequently, a nonzero momentum component perpendicular to the plane containing DP is required to realize NIM as shown by the schematic of Fig. 4.13(a). With permittivities $\epsilon_x < \epsilon_z < \epsilon_y$, the momentum vector ($q_z$) remains positive while traversing from inside to outside of the cusp region, one of the pointing vector components (s_z) changes it's sign from negative to positive. Consequently, with such orientation of biaxial media, Fabry-Perot configuration as shown in Fig. 4.13(b) offers optical modes with zero frequency dispersion (ω Vs q_z) which could be used to build single-mode laser based on monolithic crystal [76].

As an example of this behavior, we present the mode dispersion for the system where biaxial crystal As_2S_3 is surrounded by isotropic NaF. The orientation of biaxial crystal is such that the crystallographic direction having maximum optical refractive index (n) is pointed towards the perpendicular direction of the NaF-As_2S_3 interface. For this calculation, we use

constant values of n for both media [77]. Note the system mode shows negative frequency dispersion ($\frac{\partial\omega}{\partial q_z} < 0$) for $q_x = 1.8k_0$ as shown in Fig.4.14(a). Moreover, akin to the biaxial anisotropy, the nontrivial evolution of NIM turns into PIM through a critical point where $\frac{\partial\omega}{\partial q_z} = 0$ corresponding to zero dispersion. Since the mode is guided, this zero dispersion property could be used to support a continuous wave laser in a Fabry-Perot geometry.

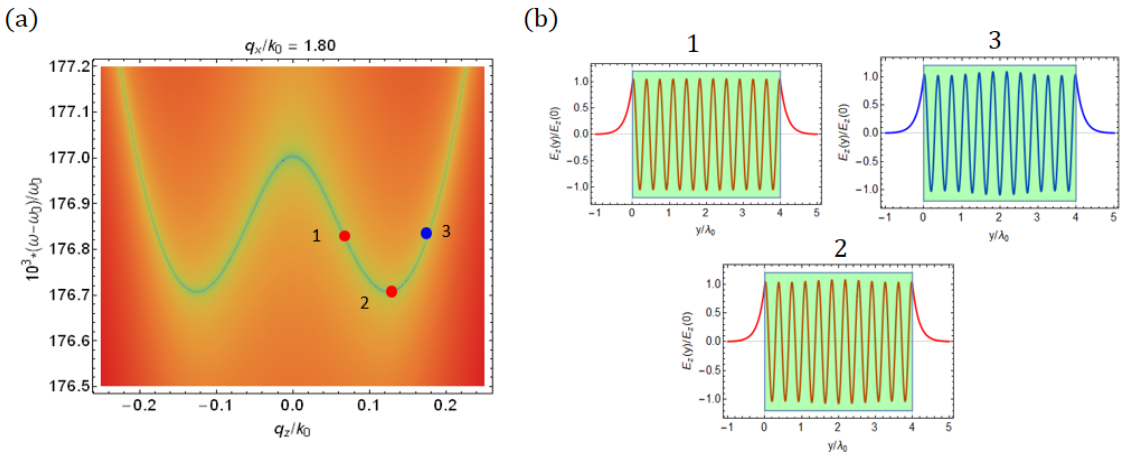

Figure 4.14. Frequency dispersion of NaF(n=1.326): As_2S_3(n=2.4,3.02,2.81): NaF(n=1.326) [77] system is shown in panel (a) as a function of q_z while q_x remains fixed. Note the presence of both NIM and PIM regimes supported by the system where the inherent anisotropy of the biaxial medium results in nontrivial evolution of the system mode between the regimes. Panel (b) depicts the field profile evolution where it is noteworthy that the parity of the mode remains unaffected.

As a second example we consider TeO_2 [78], another promising platform for optical applications[79, 80]. Out of the different crystallographic phases [81], high-pressure orthorhombic D_2^2 phase shows biaxial anisotropy. In our calculation we use refractive index of TeO_2 as n = diag[2.0,2.38,2.18] [77] sandwiched between two identical isotropic media (NaF) with optical index $n_{NaF} = 1.326$ as shown in Fig.4.13(b). Figure 4.15(a) clearly shows, as expected, that the system supports both positive and negative frequency dispersion while the evolution from NIM to PIM is plotted as a function of the tangential momentum component q_z. The zero frequency dispersion supported by the system is indicated by a red dot ("2") and the corresponding field profile is shown in Fig. 4.15(b).

Note the presence of zero frequency dispersion in both examples considered. Furthermore, the general evolution of optical modes supported by the system from NIM to PIM as a

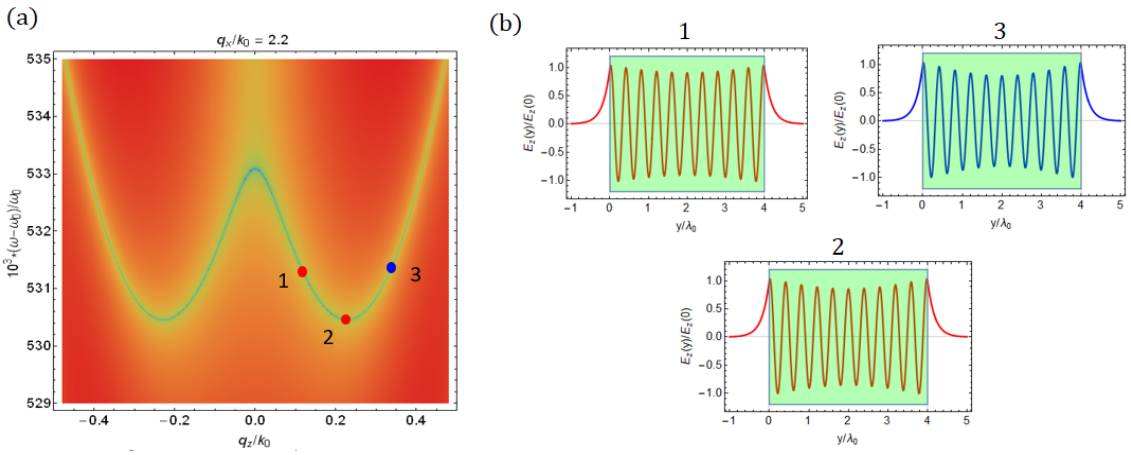

Figure 4.15. Panel-(a) shows the frequency dispersion of the system mode consisting of NaF-TeO_2-NaF. The schematic of the system is the same as shown in Fig. 4.13(b). Note the nontrivial evolution of the mode supporting NIM, PIM, and zero dispersion. Panel-(b) shows corresponding field profiles of all three regimes.

function of momentum is consistent with the nontrivial frequency dispersion of biaxial media. It is this nontrivial dispersion that results in mode degeneracies in both regime-3 and regime-4 of isotropic-biaxial-isotropic systems. In the next section, we will discuss the lifting of frequency degeneracies, which are protected by the symmetry of the system.

4.11 Lifting degeneracies and symmetry

Hybrid mode-induced degeneracies supported by isotropic-biaxial-isotropic system are the outcome of the interplay between two separate dynamics of the system. One is the result of the DP of biaxial media while the other is structure-induced parity (P) symmetry [82] which represents reflection symmetry with respect to the center of the system. Moreover, due to being Hermitian [83], the system poses time (T) reversal symmetry and combined parity-time (PT) [84–88] symmetry as well. Consequently, frequency degeneracies of such systems cannot be removed without breaking the PT symmetry.

Since, DPs of the biaxial media are material induced, removing DPs requires changing the crystallographic structure [74, 89] which would result in altering the optical phase (biaxial)

of the material. On the other hand, PT symmetry can be easily broken by either breaking P or T symmetry which results in lifting of the degeneracies as shown in Figs.(4.16 - 4.17).

In our system, P-symmetry is broken because of different isotropic media being used on the sides of biaxial crystal in parallel plate waveguide configuration as shown in Fig. 4.16 (a). The waveguide is designed to excite ghost surface waves on both interfaces as introduced in Sec. (4.5). Moreover, as discussed in Sec. (4.7), interaction between two such surface waves leads to non-monotonous frequency splitting as shown in Fig. 4.16 (b). Note the frequency separation between the modes irrespective of biaxial slab thickness resulting in no degeneracy supported by such systems.

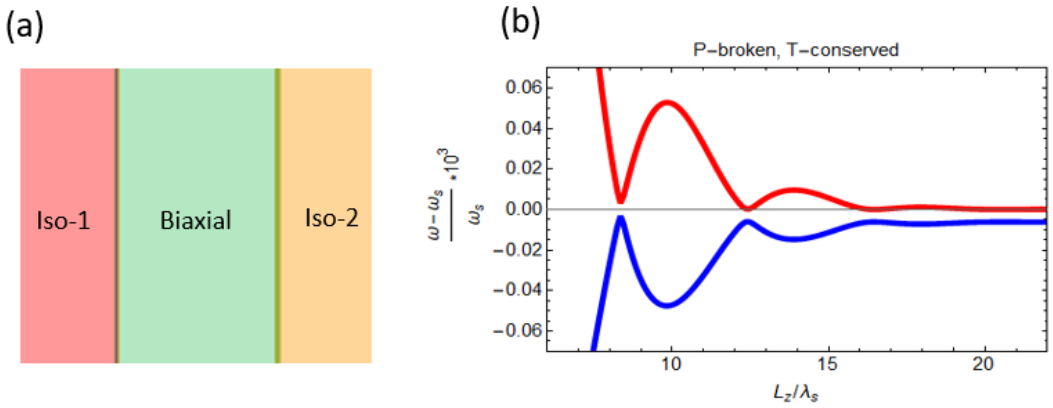

Figure 4.16. Evolution of degeneracies by removing the parity symmetry of the system, the one shown in Fig. 4.8 but with different configurations. Two different isotropic media are used with permittivities 2.01 and 2.0101 as indicated by two different colors shown in panel (a) with $NaNO_2$ as biaxial medium between them. Panel (b) shows the resonance frequencies of the system in red and blue colors as a function of biaxial slab length where the frequency separation between the modes is clearly visible for P-broken case. Here, the transverse component of wavevector used for the incident evanescent field is $(q_x, q_z) \simeq (0.793, 1.182)$ in units of ω_s/c.

Similarly, time symmetry is broken by introducing loss in the system. In our case, small amount of loss within the dielectric permittivity suffices the non-conservativeness of the system. The idea is implemented by considering two separate cases: (I) adding tiny loss within biaxial crystal while the surrounding isotropic media are transparent as shown in Fig. 4.17 (a), and (II) introducing same amount of loss in the isotropic media to keep the reflection symmetry while biaxial crystal is transparent as shown in Fig. 4.17 (c). The real part of the

permittivities are the same as PT symmetric case, and tangential momenta $(\frac{q_x}{\omega_s/c}, \frac{q_z}{\omega_s/c}) \simeq (0.793, 1.182)$ are used to excite ghost surface wave. Even though the interaction between two eigenmodes is non-monotonous, as evident from panel-(b) and panel-(d), the frequency gap between them is finite as shown in the insets.

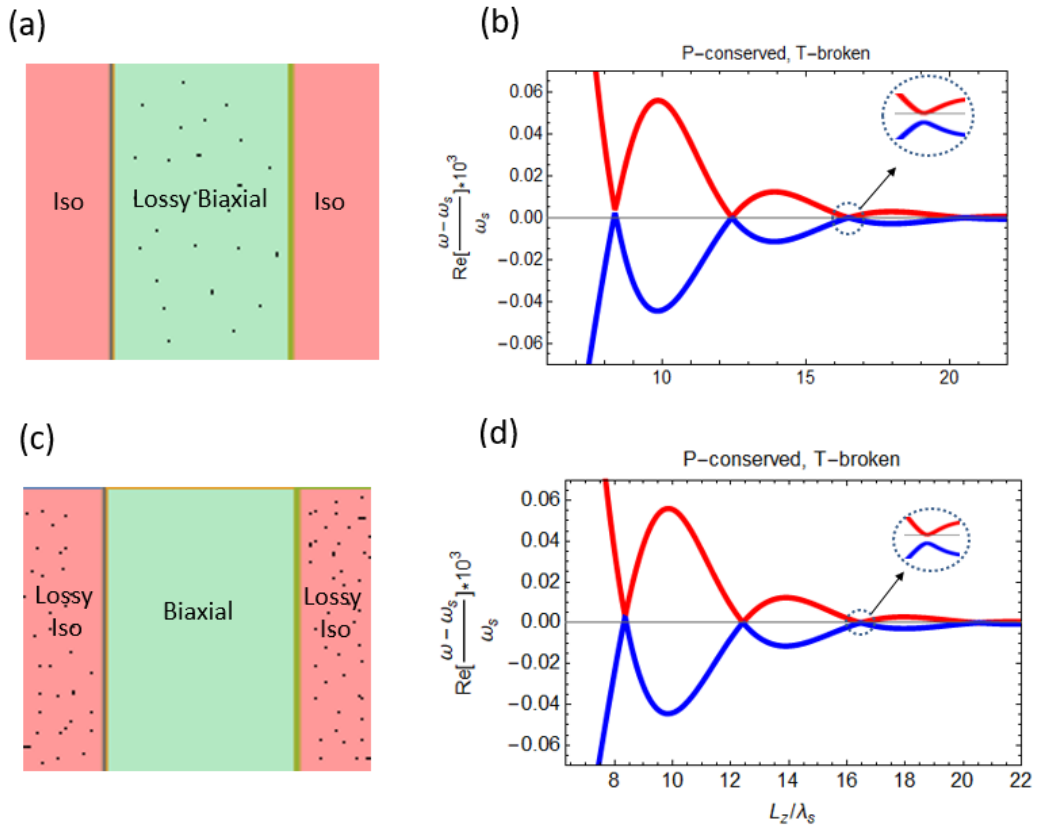

Figure 4.17. Evolution of degeneracies by removing time symmetry of the system. In the case shown by panel (a), the system is configured by introducing loss within the $NaNO_2$ with permittivity tensor $\bar{\bar{\epsilon}} = \text{diag}(1.806, 2.726 + 10^{-4}i, 1.991)$ while keeping the isotropic media on both sides transparent with permittivity 2.01. The loss within biaxial slab is indicated by black dots. However, for the second case shown in panel (c), the loss is introduced within isotropic media while the biaxial medium is transparent. The permittivities of both isotropic media are chosen as $2.01 + 10^{-6}i$ and used transparent $NaNO_2$ as biaxial medium. Corresponding surface resonance frequencies are shown on the right column in panels (b) and (d), respectively as a function of slab thickness. Note that the two resonance frequencies indicated by the red and blue colors for either case do not cross each other. A magnified view of the resonance frequencies shown in the inset of panels (b) and (d) clearly reveals the separation between them in the frequency scale for even large biaxial slab thickness.

On the contrary, however, a non-Hermitian Hamiltonian [90] can still commute with PT system. Following the quantum mechanical formalism [82, 91], a non-Hermitian [87]

system can be PT-symmetric if $\epsilon(z) = \epsilon^*(-z)$ along the transfer coordinate axis z: which requires the real (imaginary) part of the ϵ is symmetric (antisymmetric) about the center of reflection z=0. The realization of PT-symmetric optical structures in a coupled two-component system [92] has drawn considerable attention and resulted in many nontrivial effects both using active and passive systems i.e.: loss-induced transparency [93] and lasing [94], PT-symmetric lasers [95], laser absorbers [96], non-reciprocal light propagation [97], power oscillations [98], unidirectional invisibility [99, 100], etc.

In the case of active system, constituents contain equal amount of loss and gain which is contrary to the passive system where different amounts of losses are used instead of gain and loss. However, the former one is equivalent to the latter case under appropriate gauge transformation [90]. Under this transformation, zero loss of active system is equivalent to the average loss of passive system. In our research, we only consider passive system for isotropic-biaxial-isotropic slab waveguide.

The necessary complex potential for our planar system is introduced by adding different losses within the surrounding isotropic media (see Fig. 4.18(a)). With asymmetric losses, the resonance frequencies are complex in general whose real and imaginary parts are shown in panels (b) and (c), respectively. As the slab thickness is changed, contrary to T-broken or p-broken systems, for non-Hermitian PT system, not only do the real parts of the frequencies cross at the degenerate points but the imaginary parts also "spike".

The behavior of the resonance frequencies as a function of slab thickness can be described by a two-state model with an asymmetric Hamiltonian [101]

$$H = \begin{bmatrix} \omega_1 + i\gamma_1 & \kappa \\ \kappa & \omega_2 + i\gamma_2 \end{bmatrix} \tag{4.23}$$

where $\omega_{1,2}$ are the resonance frequencies of the two coupled modes, κ is the coupling coefficient, and $\gamma_{1,2}$ are their decay rates. Such a 2×2 system Hamiltonian leads to a quadratic characteristic equation, and the solution corresponds to the system resonance frequencies which can be calculated from the eigenvalues of the system as follows

$$\omega_{\pm} = \omega_{av} + i\gamma_{av} \pm \sqrt{\kappa^2 + (\omega_{diff} + i\gamma_{diff})^2} \tag{4.24}$$

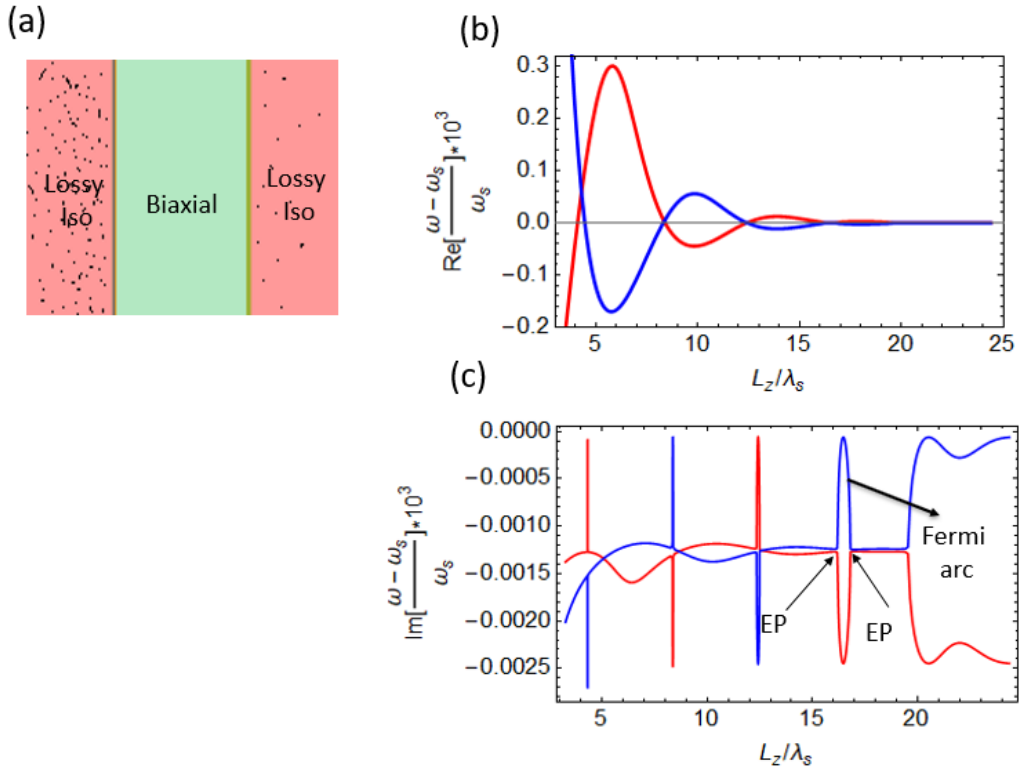

Figure 4.18. Panel (a) shows the schematic of broken-PT symmetry system implemented by introducing different losses within the isotropic media as $2.01+10^{-6}i$ and $2.01+4\times10^{-5}i$ while biaxial medium is lossless. Note that losses in isotropic media are indicated by black dots. Panels (b) and (c) show the real and the imaginary parts, respectively where red and blue colors correspond to the resonance frequencies of surface modes as a function of biaxial slab length.

Here, $\omega_{av} = (\omega_1 + \omega_2)/2$ and $\omega_{diff} = (\omega_1 - \omega_2)/2$ correspond to average and difference of the resonance frequencies, respectively, whereas $\gamma_{av} = (\gamma_1 + \gamma_2)/2$ and $\gamma_{diff} = (\gamma_1 - \gamma_2)/2$ are the associated loss factors, respectively. In general, each of the eigenvalues shows a square-root dependence on the interaction [101] between the system modes dictated by the slab thickness.

In the case of non-Hermitian PT system, $\omega_{diff} = 0$ and with appropriate gauge transformation, we can assume $\gamma_{av}= 0$ with modified eigenvalues as $\omega'_{\pm} = \omega_{av} + \pm\sqrt{\kappa^2 - \gamma^2_{diff}}$. Thus, for the PT-symmetric system to have (pseudo)real eigenvalues, $\kappa > \gamma_{diff}$ and the symmetry gets broken when $\kappa < \gamma_{diff}$. The boundary between two phases are located at the

point where $\kappa = \gamma_{diff}$, know as Exceptional point (EP) [101]. Beyond the EP, the resonance frequencies show a square-root divergence consistent with Fig. 4.18(c). Mathematically, this means the eigenvalues (ω') are taking two different paths starting from the complex branch-cut and EP marks an abrupt phase transition from real to complex spectra. Contrary to that, when P or T symmetry is broken, frequency changes smoothly near the degenerate points without any bifurcation as shown in Figs. 4.16 - 4.17. This square-root dependence near exceptional points can be utilized in sensing applications.

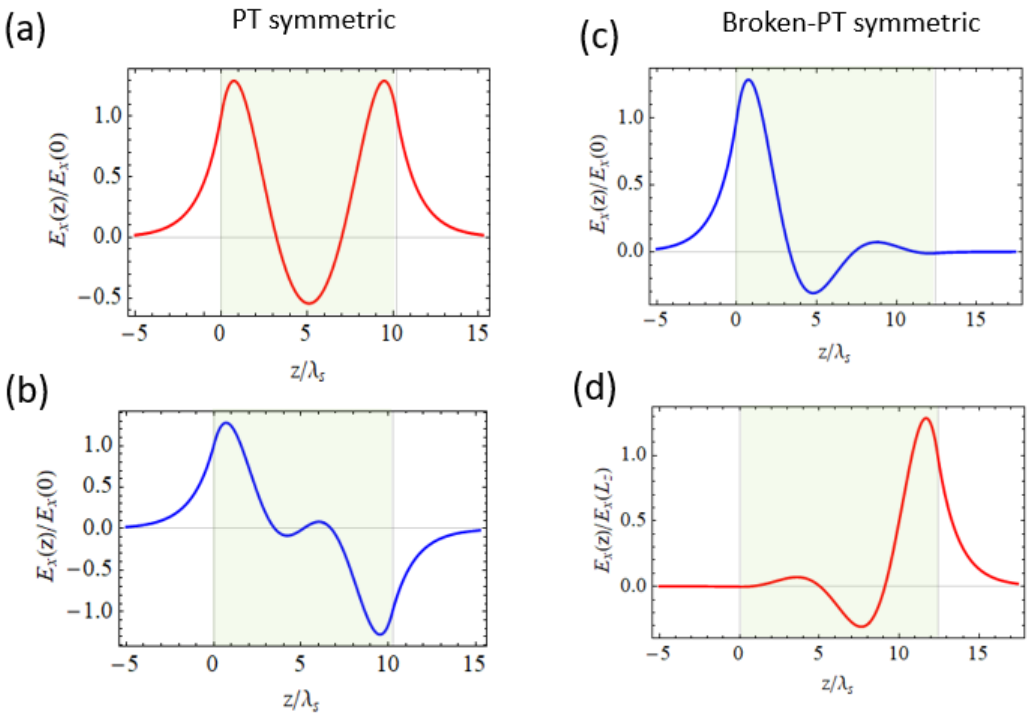

Figure 4.19. Field profiles of surface modes associated with PT-symmetric and broken-PT symmetric phases as a function of coordinate space. The system parameters are same as Fig.4.18. For PT-symmetric phase, real and imaginary parts of frequencies are taken for biaxial length $L_z = 10\lambda_s$ whereas for broken-PT phase, field profiles correspond to $L_z = 12\lambda_s$ where Im[ω] are extreme.

Note that, for large slab length $\kappa \approx 0$, which makes ω' purely complex conjugate. Consequently, eigenvalues permanently takes two branches as shown in Fig. 4.18(c) for $l_z/\lambda_s > 20$. However, for smaller biaxial length κ increases and oscillate in a periodic manner for ghost

wave as discussed in Sec.(4.7). As a result, the system goes through alternatively between PT and broken-PT phases through EPs.

In other words, we show here that ghost mode induced degenerate points give rise to a pair of EPs in high dimensional (complex) frequency space which is consistent with corresponding coupled-mode analysis. Moreover, the transition from DP to EPs has been theoretically predicted for birefringent structures [102]. It is also clear from the plot that two EPs are connected through Fermi arc [103, 104] which is a rift (hole) in complex frequency space. As long as the system possesses broken-PT symmetry, the Fermi arc is non-vanishable.

Field profiles of these two separate phases are shown in Fig. 4.19. In the PT-symmetric phase, field profiles (eigenfunctions) are similar to Hermitian system (symmetric probability distribution) as shown in panels (a) and (b). However, for broken-PT systems, such as in our case, eigenfunctions correspond to two complex eigenvalues which are symmetric with respect to the average frequency (ω_{av}). As a result, field profiles become asymmetric with respect to the center of the system. The larger the separation between imaginary parts of resonance frequency, the stronger the mismatch between the field profiles as shown in panels (c) and (d).

4.12 Summary

In conclusion, we showed that the degrees of freedom offered by the strong anisotropy in biaxial media give rise to DP. The presence of DP creates nontrivial curvature in the momentum space resulting in a cusp. Furthermore, the cusp regime evolves into the ghost regime where optical modes are simultaneous oscillatory and evanescent in nature. Due to the vectorial nature of optical modes, both the cusp and ghost regimes show frequency degeneracies and mode repulsion. The vanishing mode coupling has potential applications in integrated waveguides where undesirable crosstalk between modes can be completely prevented even at finite interaction lengths. Additionally, the degeneracies can be used for sensing purposes since any perturbation in the refractive indices caused by analyte binding would result in a measurable breaking of the system degeneracy. Since most biaxial materials are also nonlinear (e.g. KTP, LBO, $NaNO_2$, TeO_2, As_2S_3 etc), biaxial anisotropy-induced degeneracies

can also offer new ways of controlling optical modes interactions. Moreover, with correct orientation of the biaxial crystal and appropriate Fabry-Perot cavity design, the cusp regime can support cavity mode with zero frequency dispersion. Similarly, mode repulsion results in a change in the number of nodes within the same mode (wavefunction) supported by both "cusp" and ghost regimes. Furthermore, we showed that the degeneracies supported by our system are protected by PT symmetry and using standard quantum mechanism formalism, we can create broken-PT symmetry through EPs. While EPs are known to have high optical sensitivity [105, 106], field profiles of broken-PT phase are asymmetric which can be used for topological photonics [107–109] applications.

5. GHOST RESONANCE IN OPTICAL SCATTERING

This chapter has been partially reproduced from previous publications [110, 111].

5.1 Introduction

Similar to guided ghost waves where two real propagating constants annihilate each other, in the case of scattering, two frequencies do the job. Those frequencies correspond to well-known Mie [59] resonances in optical scattering [112] and consequently ghost resonance is the product of annihilation of two Mie resonances. Conversely, ghost resonance can bifurcate and give rise to two Mie resonances. We show the presence of such ghost resonances in optical scattering using structural anisotropy configured by a system of isotropic cylinders.

5.2 Ghost resonances

From conventional optical devices such as the Fabry-Perot interferometer to recent developments in nanophotonics such as negative refractive index, [113] and optical cloaking [114], the route to nontrivial electromagnetic responses generally relies on resonant field enhancement due to formation of a quasi-bound state [115]. Furthermore, quasi-bound electromagnetic states are generally interesting, as they often show counter-intuitive behavior such as the formation of a toroidal resonance [116–118], where resonance is due to the radial current instead of axial current. In the present work, we uncover another example of such nontrivial behavior - the electromagnetic ghost resonance in optical scattering.

Qualitatively, the formation of an optical resonance can generally be explained as a result of constructive interference along the path of periodic ray trajectories [119, 120]. When two such trajectories annihilate, such as in a "tangent bifurcation" [121], the corresponding optical resonance is no longer supported by the system. This quasi-classical explanation can be extended to the general case, where instead of classical trajectories one relies on resonant eigenstates derived from the exact scattering matrix of the system.

The framework of scattering theory [122, 123] is well established and has been developed to study both particle [124] and wave scattering [125]. In general, scattering (S)-matrix [126] is related to the probability amplitude of wave-function near the scatterer and to the cross-section of various interactions in both classical [127] and quantum mechanics [128]. At resonances, near the scatterer, both probability amplitude of wave function and scattering cross section which are observable, maximize. Mathematically, there are two extreme cases of probability amplitudes related to either only incoming waves or only scattered waves. They correspond to the singularities [129] of the S-matrix in complex frequency plane.

Controlling these singularities result in engineering light-scattering and many interesting phenomenon such as perfect absorption [130, 131], coherent perfect absorption [132], coherent perfect absorption laser [96, 133], virtual perfect absorption (complex zeros with temporally shaping input) [134], bound state in continuum [135–137], exceptional points [138, 139] or zeros [140] in non-Hermitian PT-symmetric system, etc. In this chapter, we show the residue of the annihilation of singularities, another interesting scattering (ghost) resonance.

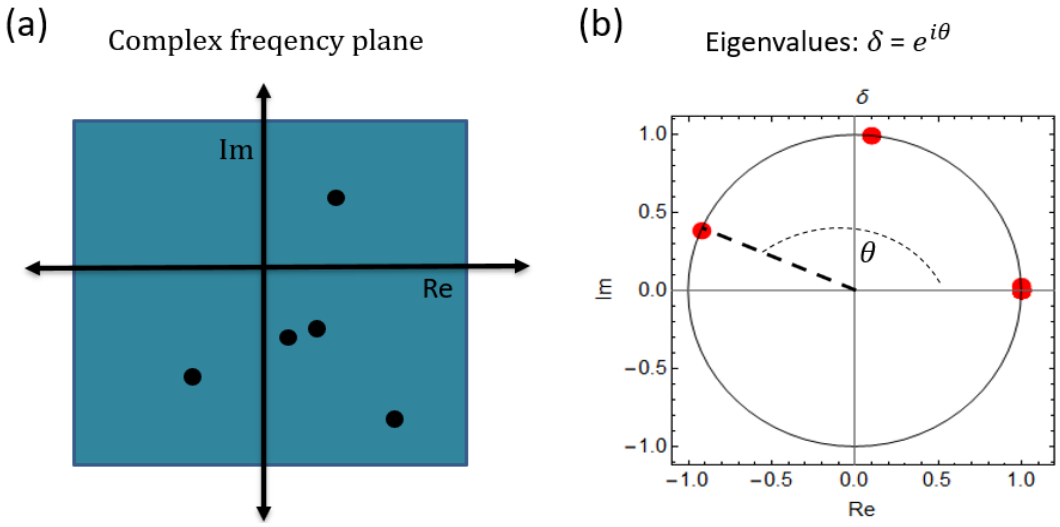

Figure 5.1. Schematics of two different approaches of calculating scattering resonances. Panel -(a) shows the conventional approach where complex resonance frequencies are indicated by black dots corresponding to the positions of the singularities of scattering matrix. Panel-(b) shows the plot of eigenvalues (red dots) of unitary matrix on unit circle where θ corresponds to the phase of each eigenvalue. Note that as the system parameters are changed, those dots rotate on the circle resulting in changes within the eigenphases only, while the magnitudes remain fixed to unity.

Furthermore, like their semi-classical counterparts, the annihilation dynamics can be explained by classical tangent bifurcation [141] in nonlinear dynamics. However, contrary to their semi-classical counterparts, in general, annihilation of two resonances at the tangent bifurcation creates "ghost" resonances which is the remnant of the annihilation. The designation "ghost" [52, 142] refers to the fact that these resonances are created in tangent bifurcations that annihilate pairs of resonances and represent the optical analog of the "ghost" orbits in the quantum theory of non-integrable dynamical systems. Conversely, ghost resonances can bifurcate and give rise to resonance pairs analogous to saddle-node bifurcation in nonlinear systems [143].

Mathematically, scattering resonances are complex numbers as shown in Fig. 5.1 (a) and finding them in a complex frequency plane involves 2D-root search. Even though the numerical search mechanism [144] is time consuming, it has been widely used to study optical phenomena such as total absorption of light by metallic grating [145, 146], coupling of incident laser beam into a waveguide [147], field enhancement [148, 149], perfect blazing of corrugated wavegudie [150], etc. However, convergence of the search mechanism depends on the starting point and the vicinity of the singular points. Moreover, if these singularities are close to each other or have low quality factor, resolving them in complex frequency space and resolving their contributions to the observable are both challenging.

In this work, we have developed a new mechanism to find those singularities which reduces higher dimensional root search into 1-D. Moreover, our mechanism distinctly resolves the contribution of each resonance to the observable (scattering cross section) irrespective of the frequency or associated quality factor. Furthermore, this approach also captures the residue of annihilation and also the bifurcation of "ghost" or "shape" [143] resonance into singularity pair. We show the presence of such "ghost" resonances in optical scattering for dielectric cylinder.

In this new approach, we first formulate the scattering matrix in angular momentum basis and calculate the matrix for single cylinder for plane wave indecent. Instead of 2D root search mechanism, we calculate eigenvalues and eigenvectors of the matrix which correspond to the scattering channels: monopole, dipole, quadruple, etc. Since, the scattering matrix is unitary, only the phases (θ) of the eigenvalues change with the system parameters as shown

in Fig. 5.1(b). Consequently, the dynamics of the system depend only on the eigenphase which is inherently 1D. Moreover, since the eigenmodes are orthogonal, the contribution to the observable from each channel can be calculated separately irrespective of their resonance frequencies and quality factors.

Using this approach, we also show the presence of new ("shape" or "ghost") class of resonance within each channel. Since the dipole is the dominant scattering mode, furthermore, we perturb the "ghost" resonance of dipole channel and bifurcate it into singularity pair similar to saddle-node [143] bifurcation in nonlinear dynamics. Finally, we show "ghost" resonance induced long-range interaction between two dipoles supported by dielectric cylinders.

5.3 Scattering matrix formalism

Consider the standard scattering problem in angular momentum basis where the S-matrix describes the scattering from angular momenta l_1 to l_2. If an incoming wave vector $\vec{\alpha}$ containing all the momentum components turns into $\vec{\beta}$ after scattering, then, mathematically those vectors are related by

$$\vec{\beta} = [S]\vec{\alpha}. \tag{5.1}$$

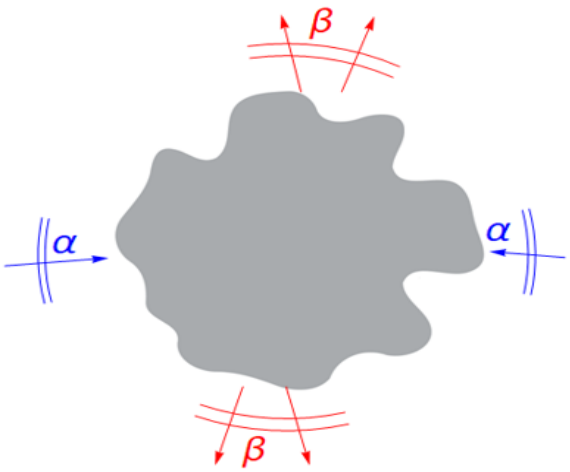

Figure 5.2. Scattering system in angular momentum basis where α and β correspond to the strength of incoming and outgoing waves, respectively

The eigenvectors of S correspond to eigenvalues of the related Hamiltonian. Therefore the eigenvector set of S does not represent a complete basis, since it only describes the scattering states which asymptotically, far from the scatterer, take the form of plane waves. Moreover, such eigenvectors do not include the bound states which have profiles that drop off exponentially ($\psi(r \to \infty) = 0$) far from the scattering object.

However, it offers the complete basis for the scattering solutions as those generally do not mix (bound state in continuum [151] is an important exception). Assuming our system does not support any bound state in continuum, for the scattering states the basis of the eigenvectors of S is both complete and orthogonal. Therefore, any field can be represented in terms of eigenvectors of S as follows

$$\psi(\vec{r}) = \sum_n \zeta_n \psi_n(\vec{r}) \tag{5.2}$$

where,

$$\psi_n(\vec{r})_{\vec{r}>\vec{R_0}} = \sum_l \alpha_l^{(n)} H_l^{(-)}(\vec{r}) + \sum_l \beta_l^{(n)} H_l^{(+)}(\vec{r}). \tag{5.3}$$

Here, $H_l^{(\pm)}$ are the incoming (-) and outgoing (+) cylindrical waves with $\{\alpha_l, \beta_l\}$ as the strength of the l^{th} component of the cylindrical harmonics and $\vec{R_0}$ is the radius of the scattering interface with respect to the center of the system.

Incoming fields enter into the scattering region via the input channels and exit through the output channels. Due to the conservation of angular momentum, each component of the incoming wave will be scattered independently and transformed into an outgoing wave according to the eigenvalue (χ) of the S matrix as follows

$$\beta_l^{(n)} = \chi^{(n)} \alpha_l^{(n)} \tag{5.4}$$

Since S is unitary, its eigenvalues must have the form of $e^{i\theta}$ which indicates conservation of the probability of scattered wave. Here, θ is a function of system parameters whose effect is to attach a phase factor to the outgoing wave. Akin to the total probability conservation, this phase shift creates angular distribution in the scattered field of the corresponding channel.

Hence, the dynamics of θ would determine the properties of the scattering field. If amplitude γ_l is a measure of the scattering in the l^{th} angular momentum, then $\vec{\gamma}$, consisting of all angular momentum components of the scattered wave can be defined as

$$\vec{\gamma} = \vec{\beta} - \vec{\alpha}. \tag{5.5}$$

The effective scattering cross-section (σ) which is different from the geometric cross-section, can be calculated from the contribution of all angular momentum components. Due to the orthogonality relation among all scattering channels, σ, with a normalization constant σ_0 yields as follows

$$\sigma = \sigma_0 \sum_n |\zeta_n|^2 \left|e^{i\theta_n} - 1\right|^2. \tag{5.6}$$

Note the functional dependency of the phase of eigenvalues with the total scattering cross-section. When the scattered wave is 180° out of phase with that of the incoming wave, the effective scattering cross section maximizes. The corresponding frequencies where the phases of the eigenvalues $\theta = \pi$, indicate the resonance frequencies of the scattering channels.

Conventionally, the frequency model is extended into complex plane to calculate the quality factor of the scattering resonance where the resonance corresponds to a pole in $S(\omega)$ at a complex point as shown in Fig. 5.1 (a). The real part of the point indicates the resonance frequency while the imaginary part corresponds to the resonance width. Contrary to that, with eigenvalue approach, such as in our case, one-dimensional dynamics of the system modes provide insight about the resonances.

Since the scattering resonance frequency is within the continuous spectrum of the system, the corresponding wave state elapses finite time within the scatting object which indicates finite quality factor of the resonance. At resonance, the interaction time of the probing wave can be quantified in terms of the *Wigner delay time* [125, 152] which is the derivative of phase of eigenvalue with respect to the resonance frequency.

In the following sections, we analyze the dynamics of scattering modes in a circular cylinder and show resonance state in each channel. Moreover, the dynamics reveal the presence of ghost resonances in optical scattering.

5.4 Plane wave scattering by single cylinder

In the case of isotropic cylinder, both TE and TM polarization modes degenerate and produce same electromagnetic responses in all propagating directions. In this work, we are only considering TM polarization which has the electric field component along the cylinder axis(z). For cylindrical system, the l^{th} angular momentum component of the field can be expressed as

$$E_z(r) \propto J_l(k_0\sqrt{\epsilon}r)exp(il\phi) \tag{5.7}$$

where (r, ϕ) are cylindrical co-ordinates, ϵ is material dielectric permittivity, J is the Bessel function of the first kind, and k_0 is the free space propagation constant. Furthermore, any plane wave can be treated as infinite summation of cylindrical harmonics and the exact scattering element of two (l, l') asymptotically free waves in angular momentum basis can be formulated as [153]

$$s_{ll'} = \frac{\sqrt{\epsilon}J_l'(k_0\sqrt{\epsilon}R)H_l^{(-)}(k_0R)J_l(k_0\sqrt{\epsilon}R)H_l'^{(-)}(k_0R)}{\sqrt{\epsilon}J_l'(k_0\sqrt{\epsilon}R)H_l^{(+)}(k_0R)J_l(k_0\sqrt{\epsilon}R)H_l'^{(+)}(k_0R)}\delta_{ll'} \tag{5.8}$$

Since the plane wave expansion [154] in angular momentum basis contains infinite components, following the conservation of angular momentum, scattered wave also contains infinite components. So the matrix $S = [s_{ll'}]$ also has infinite dimension which has been truncated [144] to conduct numerical calculation. If, L=2K+1 denotes the truncation order, corresponding to the incident and scattered waves with numbers, l=-K,...,K in Eq.(5.8). Then S matrix relates L incident and L scattered waves in angular momentum basis. The eigenvalue and eigenvector calculation of the truncated scattering matrix has been carried out using commercial computer.

Each eigenvalue of the unitary S matrix corresponds to a channel of scattering in the cylindrical system where the phase of the eigenvalue is directly related with the phase shift in the corresponding scattered wave. Even though all the eigenvalues have unit magnitudes, phases are different as shown in Fig. 5.3(b). As the system parameter (frequency of the incoming wave, in this case) is changed, all the eigenvalues traverse on unit circle in the

complex plane which only changes phases. As a result, with this approach, conventional 2D root search of the scattering resonances, reduces to 1D for the system.

The dynamics of the system can be explained by the trajectory of the corresponding eigenvalue on the unit circle which is not monotonic as shown in Fig.5.3(c). Note the presence of two different regimes:, "fast" and "slow" in the phase plot as a function of frequency. The "fast" branch is directly related to frequency of the incoming plane wave, whereas the "slow" ("shape" or "ghost" resonance [143]) branch is the contribution of the system rotational symmetry. Since the overall phase of each mode depends on the slowest path, the symmetry-induced "shape" resonance dictates the dynamics of individual scattering channel and the system as well.

The resonance frequency is indicated by ω_0 in Fig. 5.3(c) where the corresponding eigenvalue has $\theta = \pi$. Note the quality factor of the quasi-bound state is directly related with the slope of that mode at $\omega = \omega_0$. Hence, the resonance frequency can be defined with a complex term $\omega_0 - i\Gamma$, where Γ represents the width of the resonance. This description quantitatively produces the standard BreitWigner [155] profile as used in conventional methods to describe the energy distribution near the resonance.

However, the presence of ghost resonances slows down the rate at which the phases of eigenvalues evolve on the unit circle. As a consequence, if the ghost resonance is nearby the primary resonance ($\theta = \pi$), the quality factor of that resonance reduces. In the case of isotropic cylinder, ghost resonances in higher angular momentum stay relatively far from ω_0 compared to that of the lower angular momentum as evident from Fig. 5.3(c). This effect results in larger quality factor for higher angular momentum in single cylinder system. Moreover, notice the asymmetric profile of the phase with respect to the resonance frequency. Since the "slow" branch has broad frequency spectrum, any nearby presence of such branch affects the shape of the overall resonance profile. For instance, $l = 3$ mode is less skewed compared to $l = 1$ mode in the circular cylinder system as shown in Fig. 5.3(c).

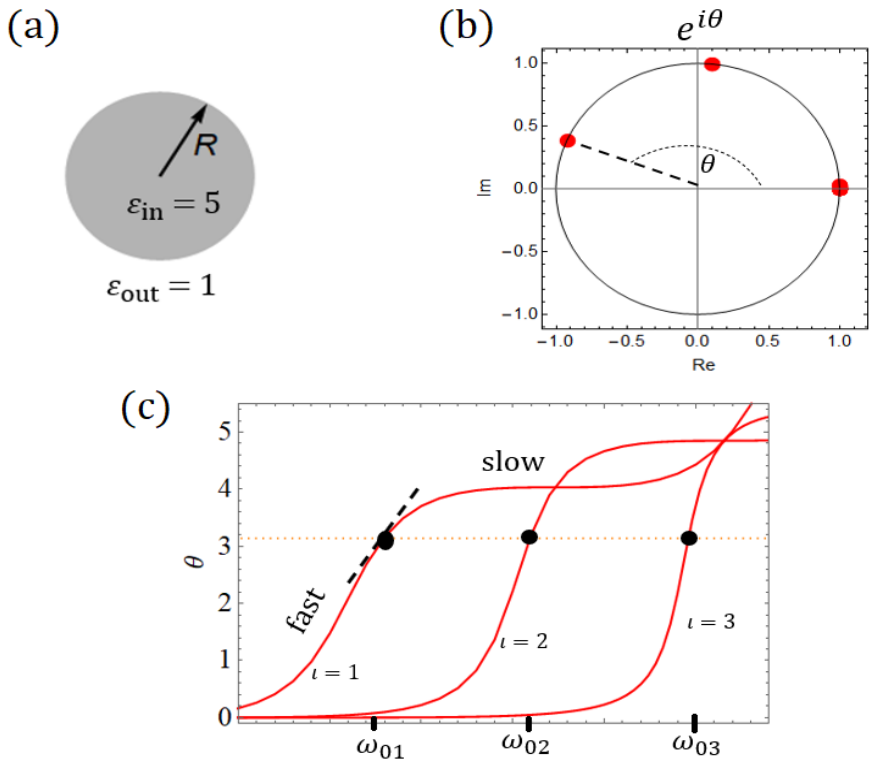

Figure 5.3. (a) Schematic of single cylinder scattering system where free space plane propagating wave is scattered by transparent dielectric cylinder with permittivity $\epsilon = 5$. Panel (b) shows the eigenvalues of the scattering matrix plotted on a unit circle where each red dot represents the system scattering mode. Panel (c) shows the rotational dynamics of the system modes ($l = 1-3$) on the unit circle as a function of the frequency of the incoming plane wave. The corresponding resonance frequencies ($\omega_{01} - \omega_{03}$) are indicated by black dots and the width (Γ) of the resonance can be calculated from the slope (black dotted line) of the phase at $\omega = \omega_0$. Note, the presence of two qualitatively different dynamics indicated by "fast" and "slow" (shape resonance). If the shape resonance is close to the primary resonance ($\theta = \pi$), then the speed of the corresponding red dot slows down on the unit circle resulting in a change in the quality factor.

To show the characteristic behavior of the scatterer, we plot the scattering cross-section of 2D cylinder as shown in Fig. 5.4(a) while being illuminated by plane wave. Mathematically, the effective scattering cross section of circular cylinder takes the form of

$$\sigma_{2D}^{norm} = \frac{\sigma_{2D}}{2R} = \frac{\lambda}{\pi R} \sum_{l} \left| e^{i\theta_l} - 1 \right|^2 \tag{5.9}$$

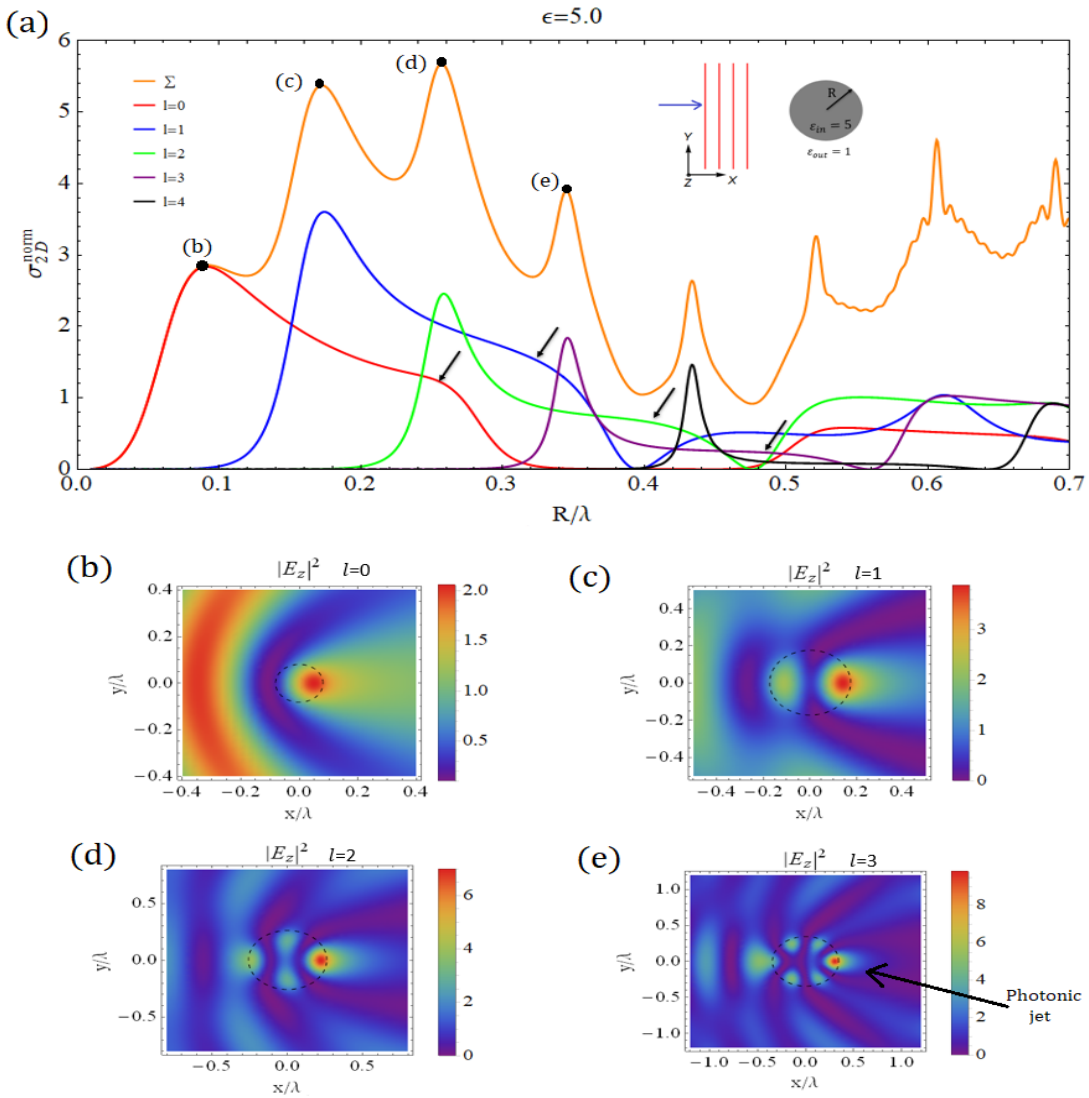

Figure 5.4. (a) Scattering cross-section of 2D cylinder illuminated by plane wave (inset) as a function of normalized wavelength (R/λ). The top (orange) curve corresponds to the total scattering cross-section and contributions from individual angular momentum are shown with different colors at the bottom. Note, the presence of shape resonance in each angular momentum channel indicated by black arrows. Panels (b)-(d) correspond to the intensity of electric field for different channels (l_s) while they are in resonance with the incoming plane wave. The corresponding positions of the resonances are indicated by black dots in panel-(a). Note that the photonic jet effect [156–159] intensifies the field strength at the shadow-side of the scatterer along the axis of plane wave propagation. Moreover, near the scatterer, the width of the jet is sub-wavelength and the confinement increases even further for higher angular momentum.

where λ is free space wavelength. Notice, two qualitatively different features are present in the total cross section as a function of the frequency $(1/\lambda)$ of incident wave. The low frequency peaks correspond to different principal energy bands [160] while the high frequency peaks within each band are due to the contribution from different channels (l). Electric field intensity profiles in Figs. 5.4(b)-(d) show the excitation mode profiles at the resonance frequency of individual channel.

Note the presence of shape resonance in each channel indicated by black arrows. Since the shape resonances have inherent broad spectrum, the presence of such resonances change the quality factor of the primary resonance and make the energy distribution asymmetric with respect to resonance frequency. It is evident from Fig. 5.4(a) that within the first principal energy band, $l = 0$ mode has the lowest quality factor since the corresponding shape resonance is closest in the frequency scale compared to that of other modes ($l > 0$) consistent with Fig. 5.3(c). Similarly, energy distribution of the resonance in higher angular momentum is more symmetric than that of lower angular momentum with respect to the corresponding resonance frequency.

To compare the conventional 2D root search method with the eigenphase approach, we calculate resonance frequencies based on both methods and compare it with respect to the position of the total scattering cross-section peak as show in Fig. 5.5. As evident from the analysis, both methods resolve the scattering cross-section peak for resonances with high quality factor (n) for all materials (ϵ_{in}). However, as the quality factor of the resonance diminishes, performance varies depending of the permittivity of the material. The eigenphase method works better over the conventional approach for high permittivity (panel-c), whereas for lower permittivity, conventional approach works better (panel-a). For low permittivity, when "n" is small, the presence of multiple resonances from nearby different channels and ghost resonance within each channel results in frequency shift of the total scattering cross-section-peak of the scatterer.

In the next section, we will discuss a systematic method to control ghost resonance in optical scattering. Since dipole is the dominant optical response, we will show a prototypical mechanism to perturb the shape resonance within the dipole mode. However, the approach holds for other modes too.

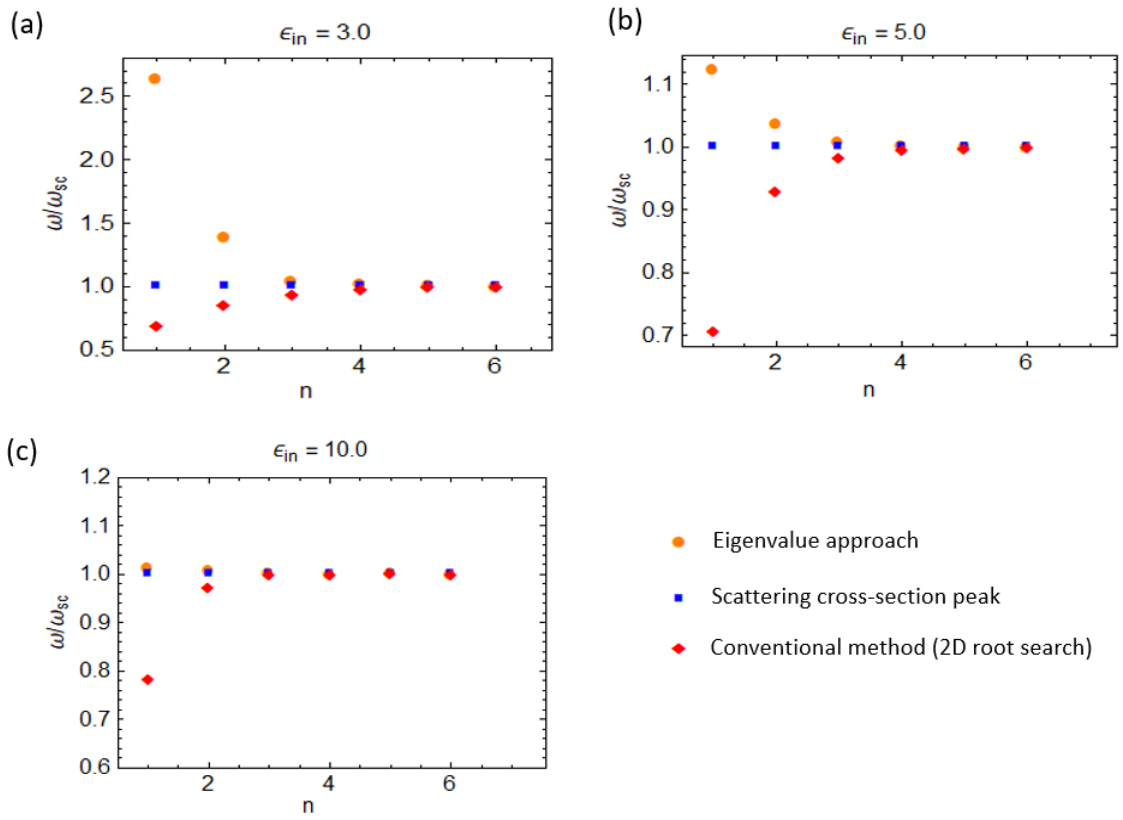

Figure 5.5. . Plot of scattering resonance frequency (ω) as a function of resonance number (n) which is proportional to quality factor (higher the value of n, higher the quality factor of the resonance is). Vertical axis of the plot is normalized to the frequency of scattering cross-section peak (ω_{sc}). Panels (a), (b), and (c) correspond to permittivity of the cylinder ϵ_{in} = 3, 5, and 10, respectively.

5.5 Optical scattering by two-cylinders system and ghost resonance

To respect the C_2 symmetry of dipole, we use a system of two identical circular cylinders separated by finite distance with two axes of symmetry as shown in Fig.5.6(a). Using standard co-ordinate transfer method [161, 162], scattering matrix of the system is calculated, and the corresponding eigenvalues are shown in Fig.5.6(b). Note that each dot on the complex plane corresponds to a scattering mode of the system. Since the system does not have rotational symmetry, dipoles become the lowest energy modes instead of monopole. The nonzero phases of two dots as shown in Fig. 5.6(b) correspond to the system dipole modes.

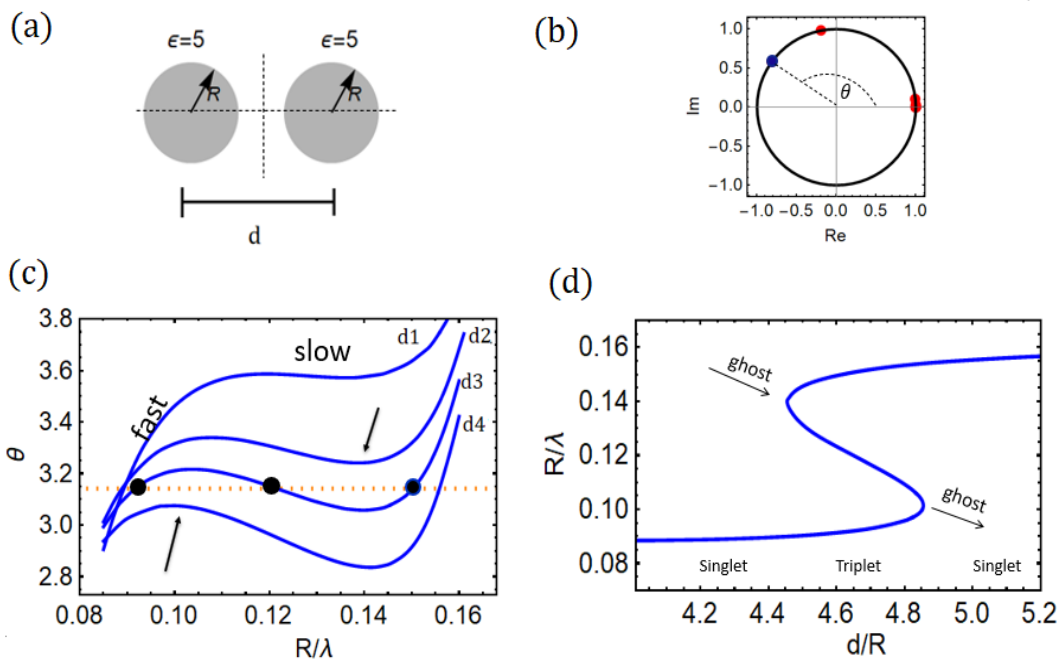

Figure 5.6. (a) Schematics of two-cylinders system separated by distance d while each cylinder having radius, R and permittivity, ϵ. Panel-(b) shows the scattering eigenvalues of the system on complex plane where each dot correspond to a system mode. As the parameters of the system are changed, all the dots traverse on the periphery of the unit circle. The nonzero phases of the two dots (red and blue) correspond to the lowest energy dipole modes of the system. Panel-(c) shows the evolution of the system mode as function of the frequency of the incoming wave where d acts as a control parameter. Note the evolution of the system mode supports three resonance frequencies indicated by purple dots. Continuous evolution of the resonance frequency is shown in panel -(d) where the system mode goes through singlet-triplet-singlet (STS) transition in normalized parameter space.

At low energy, higher order modes are not being scattered by the system and hence, phases of the corresponding eigenvalues are zero.

To show the dynamics of the system mode, we plot the phase of the eigenvalue corresponds to one of the dipole modes as a function of frequency (see Fig.5.6(c)). Note, the presence of both "fast" and "slow" branches in the system mode for d=d_1 which are similar to that of single cylinder case (see Sec.5.4). As the separation between the scatterers is changed to d=d_2, the symmetry-induced dynamics evolve into ghost resonance indicated by black arrow. Eventually, ghost resonance bifurcates and creates system triplet state at $d = d_3$ where the mode supports three resonance frequencies. Further change in d = d_4 leads to

the annihilation of two resonance frequencies followed by the creation of one ghost at low frequency while the system resonates at high frequency.

Continuous evolution of singlet-triplet-singlet (STS) transition is shown in Fig.5.6(d) which looks like "S" in the parameter space of d/R vs R/λ. This nontrivial evolution is due to the presence of system ghost modes (black arrows) in both low and high frequency regimes. At the tangent bifurcation points, these ghost resonances split and give rise to system dipole resonances.

Evolution of the electric field intensity is shown in Fig. 5.7 while the system is illuminated by plane wave propagating along the end-fire axis. The configuration of the system illumination is shown in panel-(a) inset. Note that, even though an incoming plane wave has all $(-\infty, \infty)$ angular momentum components, only few of them would be scattered by each cylinder due to their finite size (R). Furthermore, spatially separated scattered fields from each object would overlap and excite secondary waves. However, due to coustic effect [163], only few angular momenta compared to the size of the system would couple to each other and form the scattering mode of the system. Moreover, the lack of rotational symmetry results in $l = 0$ mode to cease to exist within the system. On the contrary, structural induced C_2 symmetry is in favor of dipole mode and thus the lowest energy mode of the system turns out to be dipole ($l = 1$).

Figures 5.7(b)-(f) illustrate different cylinder modes responsible for the system resonance. At low frequency (lowest"arm" of "S"), constituents of the system behave as monopole which is consistent with the monopole resonance frequency of the individual cylinder (see Fig. 5.4(a)). Similarly, high frequency (highest "arm" of "S"), corresponds to dipole excitation within the constituents of the system as shown in panel-(f). Continuous transition between monopole and dipole excitations are mediated (middle "arm" of "S") due to the presence of ghost modes. Since the origin of the ghost mode comes from the slowest dynamics of the system, the middle "arm" of the triplet state has the lowest quality factor consistent with the leaky nature of the field profile as shown in panel-(d). From the field profile, it is evident that during the transition, constituents of the system neither behave like monopoles nor dipoles. Instead, maximum energy of the field is confined between the cylinders.

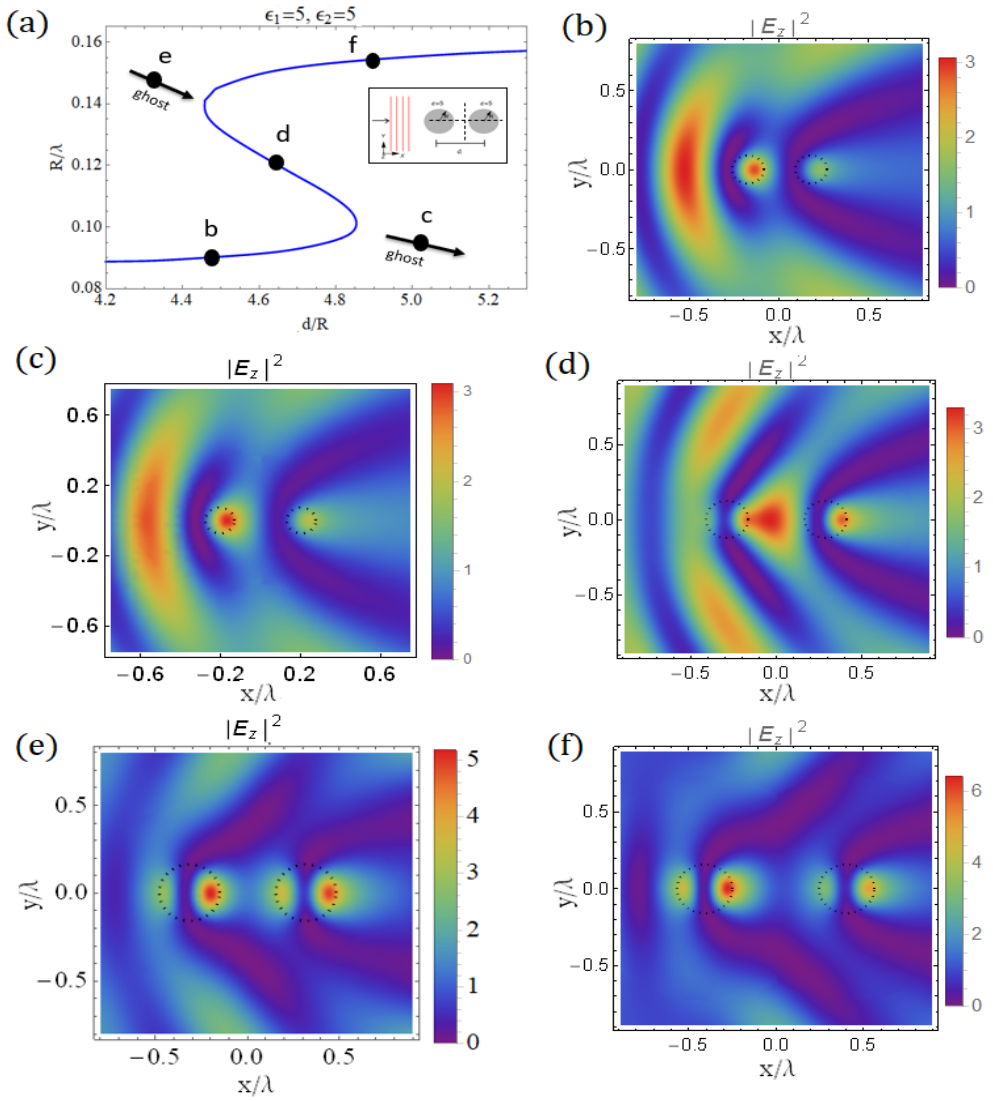

Figure 5.7. Evolution of the dipole mode of the system in the parameter space of d/R vs R/λ is shown in panel -(a). The corresponding field intensity profiles are shown in panels (b)-(f) for the resonance frequencies indicated in panel (a). Note the presence of photonic jet in each intensity profile at the shadow side of the system where the positions of the cylinders are indicated by black dotted circles. Moreover, during the transition, constituents of the system continuously evolve to operate from monopole (panel-b) to dipole (panel-f) while the system behaves as a dipole. The middle "arm" of the triplet state corresponds to the system resonance where maximum energy of the mode is confined between the cylinders resulting in the leaky nature of the mode as shown in panel-(d). However, beyond the tangent bifurcations, system still resembles a dipole thus indicating the presence of ghost regime where constituents could behave as either monopole (panel-c) or dipole (panel-e) depending on the operating frequency.

Note the field profiles of ghost resonances shown in panel-(c) and panel-(d). Even though scattering due to ghost resonance does not represent true system resonance, constituents of the system behave in such a way that the system resembles resonance with the incoming plane wave. After the annihilation of resonance frequencies at d/R = 4.85, monopole excitation still continues within each cylinder for d/R > 4.85. Similarly, for the highest "arm" of "S", dipole excitation within each cylinder also sustains even after the annihilation as shown in panel-(e).

The existence of ghost effect can be explained based on the extension of resonance dynamics to an extended phase space of higher dimensionality. In this higher-dimensional space, the resonance remains in existence even beyond the point of the tangent bifurcation in this approach. This is akin to the behavior of the solutions of a quadratic equation - while a real solution can only exist if the corresponding discriminant is not negative. In a higher dimensional (complex) space, this equation always has a solution irrespective of the sign of discriminant. The ghost resonance can then be explained as a projection of this higher-dimensional resonance onto the actual physical phase space.

Finally, to show observable scattering behavior, we plot the scattering cross-section of the system as shown in Fig.5.8. The configuration of the structure and illumination are shown in panel-(a). The coupling effect with respect to the size of the cylinders, separation between the cylinders, and wavelength of the incoming light are studied here. The color density plot of panel-(b) corresponds to normalized scattering cross section as a function of separation between the cylinders and the wavelength of the incoming wave where both parameters are normalized by the radius of the cylinder.

To compare different methods, we calculate scattering resonance frequencies of the system of two cylinders based on both eigenvalue method (continuous lines) and conventional method (discrete crosses) which are superimposed on the plot as shown in Fig.5.8 (b). Note that, even though frequencies from both methods follow the peaks of the scattering cross-section, they are slightly off due to low permittivity of the cylinders and low quality factor of the resonance mode as we discussed in Sec. 5.4 (see Fig. 5.5 (b)). Furthermore, notice the presence of strong scattering activity due to ghost resonance (dotted green line) which diminishes gradually from the bifurcation point as a function of cylinder separation. On the other

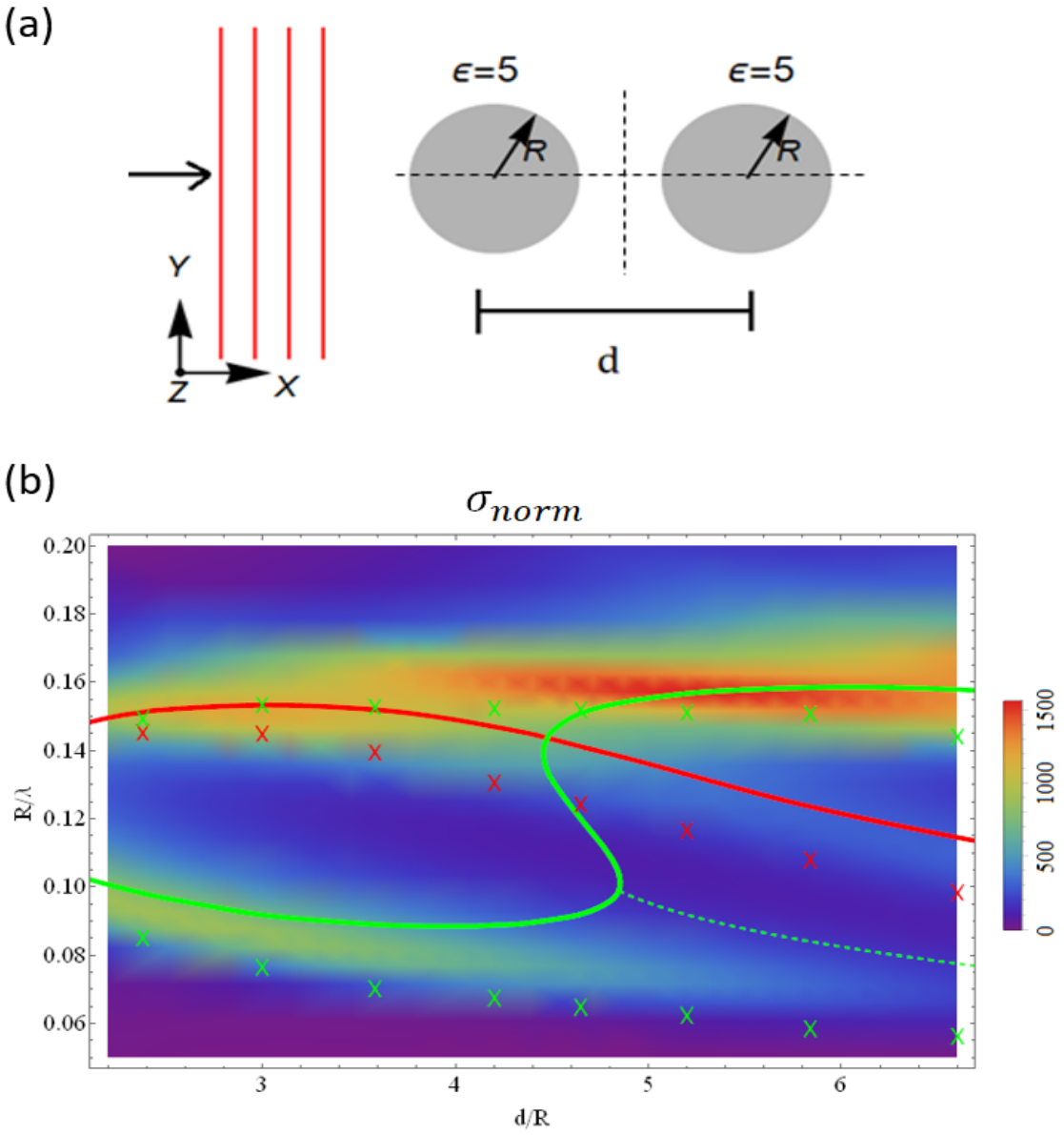

Figure 5.8. Scattering cross-section of the system of two isotropic cylinders with permittivity $\epsilon = 5$ surrounded by air. Panel-(a) shows the system setup for end-on illumination with a plane wave. Corresponding normalized scattering cross section (σ_{norm}) is shown in panel-(b) in false color as a function of system parameters. Notice the scattering cross section peak due to ghost resonance indicated by the dotted green line.

hand, the transition "arm" of the triplet state does not show strong scattering activity due to the leaky nature of the system mode consistent with field intensity profile shown in Fig 5.7(d).

For smaller separation between the cylinders ($d/R < 3$), there are two scattering cross-section peaks which is consistent according to the eigenvalue method. However, contrary to that, the conventional method indicates three resonances for smaller separation. On the other hand, for larger separation ($d/R > 4$), the conventional method works well since there are three observable scattering cross-section peaks consistent with the number of resonance modes. Similarly, with the concept of ghost resonance, which starts at the extreme point of triplet state, the eigenvalue method is also consistent.

Even though both methods work well for large separation between the cylinders, the conventional approach cannot explain the gradual decrease of the cross-section peak with the increase of separation ($d/R > 4.8$ and $R/\lambda < 0.08$). Since ghost resonance can be thought of as the projection of higher dimensional frequency on physical phase space, there is always an exponentially decaying factor associated with it which explains the diminishing factor of cross-section peak. Furthermore, the eigenvalue method shows the exact starting point of the ghost scattering regime.

To show that eigenphase method works for even larger separation we extend our calculation for distance till $d/R = 20$ as shown in Fig. 5.9. Note the STS transitions of both dipole modes and creation of ghost resonances each time from the tip of "S" indicated by dotted lines. Whereas, conventional method also tracks the resonance peaks but does not know the existence of ghost resonances. Finally, when the separation is too large to create strong coupling between the cylinders, both the system dipole modes no longer show STS transitions. Instead, the system behaves like two individual dipoles with resonance frequencies of that of single cylinder dipole. Note that there are ghost resonances also at higher frequency ($R/\lambda > 0.16$) due to the STS transitions of dipole modes. However, associated scattering cross-sections are screened out due to the presence of scattering from high frequency system modes.

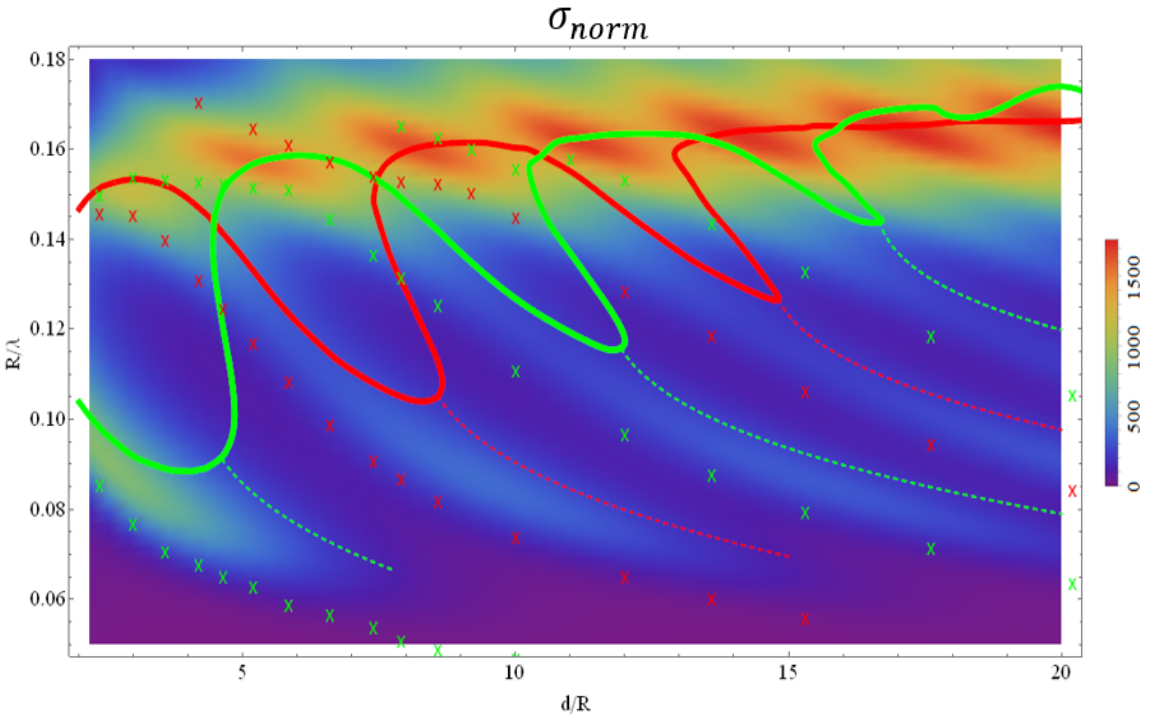

Figure 5.9. Normalized scattering cross section (σ_{norm}, in false color) of two dielectric cylinders due to lowest order dipole modes as a function of separation (d) and incoming wavelength(λ). Both parameters are normalized with respect to the radius of the cylinder (R). The evolution of the resonance frequency calculated based on conventional (crosses) and eigenvalue approaches (solid and dash lines) are superimposed on the plot. Note the presence of ghost resonance (dashed line) and associated scattering cross sections peaks due to STS transitions of the system dipole modes.

5.6 Ghost induced long-range interaction and polarization of dipole modes

The C_2 symmetry of the two-cylinders system supports total four dipole modes. Here, we are showing all four eigenmodes (m_1-m_4) of the system as shown in Fig. 5.10(a). The resonance frequencies of the modes are calculated based on the eigenvalue method whose polarizations are indicated in the inset. Note the presence of frequency splittings and degeneracies between symmetric and anti-symmetric polarizations of both broadside and end-on orientations of the dipoles. The splitting is due to the coupling between the scattered field from each cylinder while the oscillatory nature of the scattering mode is responsible for the frequency degeneracies.

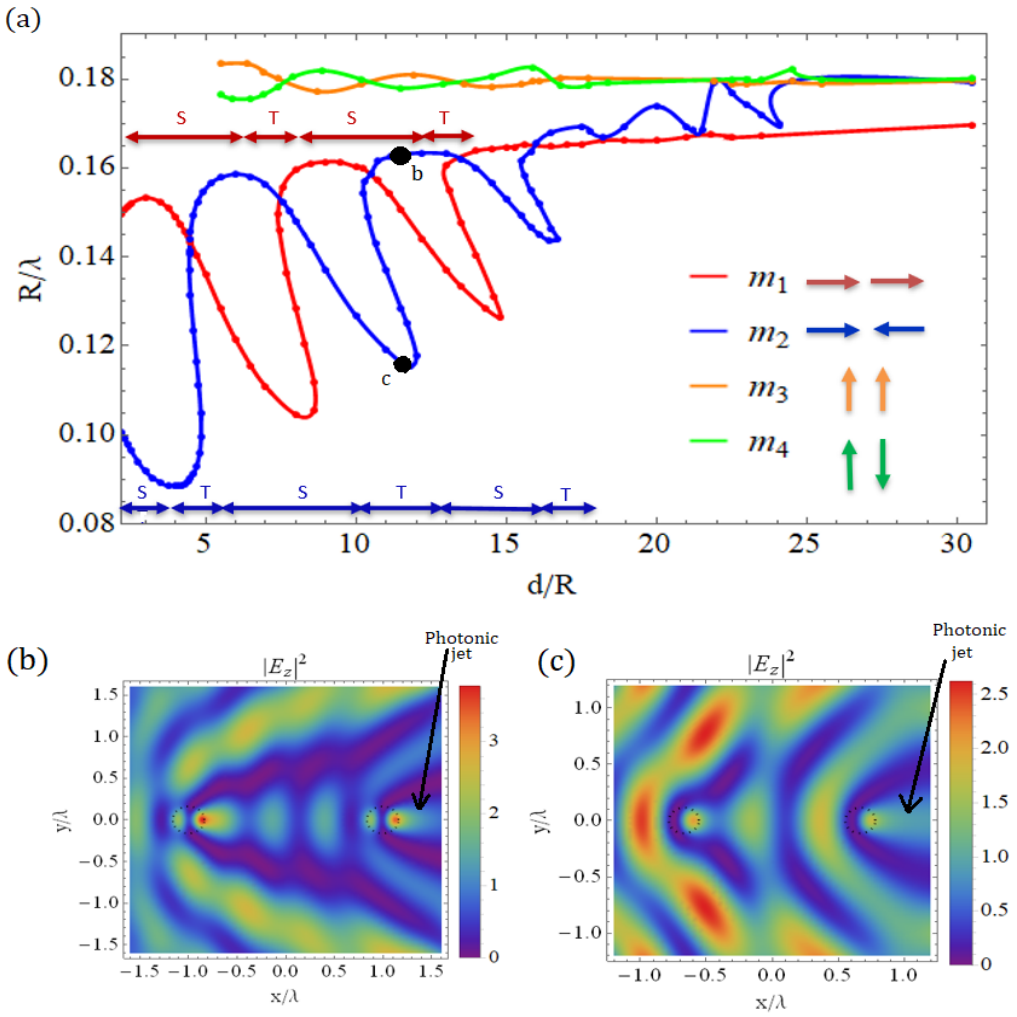

Figure 5.10. (a) Evolution of the system dipole modes as a function of normalized frequency (R/λ) and normalized separation (d/R) between the cylinders with dielectric permittivities $\epsilon = 5$. The orientation of each eigenmode is indicated in the inset. For large separation constituents of the system behave like an individual cylinder and all the system modes (m_1-m_4) approaches a single cylinder dipole frequency (R/λ = 0.1795) consistent with Fig.5.4(a). As the separation decreases, coupling results in frequency splitting of broadside modes with respect to the single cylinder dipole frequency. However, symmetric and anti-symmetric modes of end-on orientation evolve through STS transition multiple times due to the presence of ghosts. Consequently, as evident from the intensity plots of the electric field in panels (b)-(c), the interaction between the scatterer extends for long-range (d/λ>1). Notice, the presence of photonic jet at the end of the system for both field plots. Furthermore, while panel-(b) shows long-range dipole-dipole interaction, pane-(c) shows monopole-monopole coupling for resonance frequencies indicated in panel (a).

As the separation between the cylinders increases, coupling becomes weaker. Consequently, the frequencies of the system dipole modes asymptotically approach the single cylinder electric dipole frequency (see Fig. 5.4(a)). Since the end-on symmetric mode corresponds the strongest coupling among all other system dipole modes, constituents of the system need to be placed farthest to reach the asymptotic frequency.

Conversely, as the coupling increases for finite distance, frequencies of two collective modes (m_3 and m_4) of broadside orientation oscillate above and below the isolated cylinder dipole frequency. The amplitude of the oscillation increases as the cylinders are brought closer to each other. Associated field distributions of individual dipoles are such that their orientations correspond to symmetric and antisymmetric combinations. This behavior is consistent with the theoretical prediction of toroidal dipole modes supported by two cylinders system [117].

On the other hand, end-on-oriented modes (m_1 and m_2) evolve through STS transition multiple times as the coupling is increased. Note the presence of bifurcation and annihilation every time the system evolves through the transition giving rise to ghost resonances at multiple frequencies within the strong coupling regime. With $\epsilon = 5$ used for both cylinders, ghost induced strong coupling persists up to $d/R \approx 18.0$ as shown in Fig. 5.10(a).

To show the long-range interaction, we plot field profiles in panels (b)-(c) for large separation between the cylinders ($d/\lambda > 1$). Note the presence of photonic jet at the end of the system indicating that the overall system behaves like a dipole while the constituents have degrees of freedom of operating either as dipole (panel -b) or monopole (panel-c).

Physical explanation of such degrees of freedom and STS transitions can be explained by the presence of ghost resonances and their broad spectrum within each channel as introduced in Sec. 5.4 and shown in Fig. 5.4(a). With broad spectrum, dipole-ghost induced scattered field from both cylinders induce monopole resonance within their neighbors in such a way that the system behaves like dipole. As a consequence, the operating frequency of the system reduces close to individual monopole frequency of the cylinder. Similarly, while the monopole modes are excited in both cylinders, ghost resonance of monopole modes induce dipoles within their neighbors. As such, the constituents of the system change their operation

mode between monopole and dipole while the system resonance frequencies oscillate, and the amplitude of oscillation increases gradually with the increase of coupling.

5.7 Summary

In summary, we have shown a new mechanism to calculate scattering resonance and compared with the conventional approach for single dielectric cylinder. Using this new approach, we show the presence of ghost resonance in optical scattering which originates from the rotational symmetry of the scatterer. Moreover, the presence of ghost resonance for each angular momentum state allows one to build a macroscopic optical system supporting such resonances. We extended our calculation for a system of two cylinders using the eigenvalue approach and showed the presence of ghost resonance supported by the system. By varying the system parameters, we have shown a systematic method of bifurcating such ghost resonances giving rise to new system resonances. Furthermore, akin to the broad spectrum of ghost resonances the constituents of the system continuously change their excitation mode between monopole and dipole while the system goes through the STS transition. Such ghost induced transitions lead to long range ($d >> \lambda$) dipole-dipole and monopole-monopole interactions exceeding current state of art [164] which claims a sub-wavelength interaction length ($d \approx \lambda/2$) using hyperbolic metamaterials.

6. CONCLUSION AND FUTURE WORK

The manifestation of different optical phases in the optical anisotropy sets directional dependent refractive indices as independent macroscopic parameters. By using these macroscopic degrees of freedom, more optical phases are expected to open in the future which could push the current state-of-art in optical science and technologies. In this research, we investigated all three classes (isotropic, uniaxial, and biaxial) of dielectric anisotropy and showed qualitatively new optical properties along several avenues: light absorption, thermal radiation, guided modes, and optical scattering.

In particular, we have shown the persistence of Brewster phenomenon even in the presence of material loss by using anisotropic media. Moreover, we showed, that changes in the topology of electromagnetic responses associated with phase transitions leave characteristic signatures in far-field thermal emission. As we further increase anisotropy in material parameters (biaxial media), nontrivial curvature in the momentum space results in qualitatively new electromagnetic responses including but not limited to mode degeneracies, mode interactions, negative frequency dispersion, and ghost surface waves. Using planar geometry with a biaxial core, we showed changes in the mode profiles which are usually obtained by circular geometry [165]. Furthermore, the presence of EPs and topological modes supported by planar geometry has opened new avenues for low-cost optical sensing [44] and lead us to expect topological photonics [166] on simple geometry, respectively.

In this research, we only considered naturally available biaxial crystals where all permittivity components are positive. However, a combination of their degrees of freedom in material parameters along with their ($\pm$) sing can offer many more optical phases for future research. Moreover, anisotropic media are known to have nonlinear optical responses. Evolution of linear optical properties found in this research is an intriguing question that needs to be answered. One of the challenges remains in the small degrees of optical anisotropy available within natural media. In the near future, multi-layer artificial composites will hopefully achieve this using nano-fabrication technology.

Furthermore, we have shown how internal degrees of freedom for circular geometry can be used by the presence of "ghost" resonance in optical scattering. The origin of such a new

class of resonances is related to circular symmetry and examples have been presented based on single and two cylinders systems. The result needs to be extended for periodic structure and explore the consequence of symmetry-induced resonances for larger systems.

To summarize, we have shown how degrees of freedom in material parameters and structural symmetry open up new optical phases which bring qualitatively new properties. It is the author's sincere belief that this will have broad impacts on both scientific advances and technological development.

REFERENCES

[1] V. M. Shalaev, "Optical negative-index metamaterials," *Nature photonics*, vol. 1, no. 1, pp. 41–48, 2007.

[2] S. Debnath, E. Khan, and E. E. Narimanov, "Incoherent perfect absorption in lossy anisotropic materials," *Optics express*, vol. 27, no. 7, pp. 9561–9569, 2019.

[3] N. Liu, M. Mesch, T. Weiss, M. Hentschel, and H. Giessen, "Infrared perfect absorber and its application as plasmonic sensor," *Nano letters*, vol. 10, no. 7, pp. 2342–2348, 2010.

[4] V. Petrov and V. Gagulin, "Microwave absorbing materials," *Inorganic Materials*, vol. 37, no. 2, pp. 93–98, 2001.

[5] K. Aydin, V. E. Ferry, R. M. Briggs, and H. A. Atwater, "Broadband polarization-independent resonant light absorption using ultrathin plasmonic super absorbers," *Nature communications*, vol. 2, no. 1, pp. 1–7, 2011.

[6] Y. Chong, L. Ge, H. Cao, and A. D. Stone, "Coherent perfect absorbers: Time-reversed lasers," *Physical review letters*, vol. 105, no. 5, p. 053 901, 2010.

[7] W. Wan, Y. Chong, L. Ge, H. Noh, A. D. Stone, and H. Cao, "Time-reversed lasing and interferometric control of absorption," *Science*, vol. 331, no. 6019, pp. 889–892, 2011.

[8] W. Li and J. Valentine, "Metamaterial perfect absorber based hot electron photodetection," *Nano letters*, vol. 14, no. 6, pp. 3510–3514, 2014.

[9] I. Celanovic, D. Perreault, and J. Kassakian, "Resonant-cavity enhanced thermal emission," *Physical Review B*, vol. 72, no. 7, p. 075 127, 2005.

[10] N. I. Landy, S. Sajuyigbe, J. J. Mock, D. R. Smith, and W. J. Padilla, "Perfect metamaterial absorber," *Physical review letters*, vol. 100, no. 20, p. 207 402, 2008.

[11] A. Tittl, P. Mai, R. Taubert, D. Dregely, N. Liu, and H. Giessen, "Palladium-based plasmonic perfect absorber in the visible wavelength range and its application to hydrogen sensing," *Nano letters*, vol. 11, no. 10, pp. 4366–4369, 2011.

[12] D. Baranov, A. Vinogradov, and C. Simovski, "Perfect absorption at zenneck wave to plane wave transition," *Metamaterials*, vol. 6, no. 1-2, pp. 70–75, 2012.

[13] Z. Wang, Y. Feng, B. Zhu, J. Zhao, and T. Jiang, "Explicit expression of the pseudo-brewster angle for anisotropic metamaterials," *Optics Communications*, vol. 284, no. 12, pp. 2678–2682, 2011.

[14] M. Khalid, N. Tedeschi, and F. Frezza, "Analysis of reflection from a novel anisotropic lossy medium characterized by particular material properties," *Journal of Electromagnetic Waves and Applications*, vol. 31, no. 8, pp. 798–807, 2017.

[15] D. Baranov, J. H. Edgar, T. Hoffman, N. Bassim, and J. D. Caldwell, "Perfect interferenceless absorption at infrared frequencies by a van der waals crystal," *Physical Review B*, vol. 92, no. 20, p. 201 405, 2015.

[16] C. A. Balanis, *Antenna theory: analysis and design*. John wiley & sons, 2016.

[17] M. Tschikin, S.-A. Biehs, R. Messina, and P. Ben-Abdallah, "On the limits of the effective description of hyperbolic materials in the presence of surface waves," *Journal of Optics*, vol. 15, no. 10, p. 105 101, 2013.

[18] H. Ryu, K. Jeon, M. Kang, H. Yuh, Y. Choi, and J. Lee, "A comparative study of efficiency droop and internal electric field for ingan blue lighting-emitting diodes on silicon and sapphire substrates," *Scientific reports*, vol. 7, no. 1, pp. 1–9, 2017.

[19] M. Schubert, T. Tiwald, and C. Herzinger, "Infrared dielectric anisotropy and phonon modes of sapphire," *Physical Review B*, vol. 61, no. 12, p. 8187, 2000.

[20] S. Vangala, G. Siegel, T. Prusnick, and M. Snure, "Wafer scale bn on sapphire substrates for improved graphene transport," *Scientific reports*, vol. 8, no. 1, pp. 1–9, 2018.

[21] M. Autore *et al.*, "Boron nitride nanoresonators for phonon-enhanced molecular vibrational spectroscopy at the strong coupling limit," *Light: Science & Applications*, vol. 7, no. 4, pp. 17 172–17 172, 2018.

[22] A. B. Djurii and E. H. Li, "Optical properties of graphite," *Journal of applied physics*, vol. 85, no. 10, pp. 7404–7410, 1999.

[23] D. Brewster, "On the laws which regulate the polarisation of light by reflexion from transparent bodies," *Philosophical Transactions of the Royal Society of London*, vol. 105, pp. 125–159, 1815.

[24] A. V. Kukushkin, A. A. Rukhadze, and K. Rukhadze, "On the existence conditions for a fast surface wave," *Physics-Uspekhi*, vol. 55, no. 11, p. 1124, 2012.

[25] S. Debnath and E. E. Narimanov, "Thermal emission at the optical topological transition," *Applied Physics Letters*, vol. 115, no. 15, p. 151 906, 2019.

[26] I. Lifshitz *et al.*, "Anomalies of electron characteristics of a metal in the high pressure region," *Sov. Phys. JETP*, vol. 11, no. 5, pp. 1130–1135, 1960.

[27] E. Abbe, "Beiträge zur theorie des mikroskops und der mikroskopischen wahrnehmung," *Archiv für mikroskopische Anatomie*, vol. 9, no. 1, pp. 413–468, 1873.

[28] P. Shekhar, J. Atkinson, and Z. Jacob, "Hyperbolic metamaterials: Fundamentals and applications," *Nano convergence*, vol. 1, no. 1, p. 14, 2014.

[29] H. N. Krishnamoorthy, Z. Jacob, E. Narimanov, I. Kretzschmar, and V. M. Menon, "Topological transitions in metamaterials," *Science*, vol. 336, no. 6078, pp. 205–209, 2012.

[30] Z. Liu, H. Lee, Y. Xiong, C. Sun, and X. Zhang, "Far-field optical hyperlens magnifying sub-diffraction-limited objects," *science*, vol. 315, no. 5819, pp. 1686–1686, 2007.

[31] L. V. Alekseyev and E. Narimanov, "Radiative decay engineering in metamaterials," *Tutorials in Metamaterials*, pp. 209–223, 2011.

[32] Y. Guo, C. L. Cortes, S. Molesky, and Z. Jacob, "Broadband super-planckian thermal emission from hyperbolic metamaterials," *Applied Physics Letters*, vol. 101, no. 13, p. 131 106, 2012.

[33] S.-A. Biehs, M. Tschikin, and P. Ben-Abdallah, "Hyperbolic metamaterials as an analog of a blackbody in the near field," *Physical review letters*, vol. 109, no. 10, p. 104 301, 2012.

[34] Y. Guo and Z. Jacob, "Thermal hyperbolic metamaterials," *Optics express*, vol. 21, no. 12, pp. 15 014–15 019, 2013.

[35] C. Luo, A. Narayanaswamy, G. Chen, and J. Joannopoulos, "Thermal radiation from photonic crystals: A direct calculation," *Physical Review Letters*, vol. 93, no. 21, p. 213 905, 2004.

[36] M. R. Querry, *Optical constants of minerals and other materials from the millimeter to the ultraviolet*. Chemical Research, Development & Engineering Center, US Army Armament , 1987.

[37] R. Siegel and J. Howell, *Thermal radiation heat transfer, hemisphere, washington, d*, 1981.

[38] B. T. Schwartz and R. Piestun, "Total external reflection from metamaterials with ultralow refractive index," *JOSA B*, vol. 20, no. 12, pp. 2448–2453, 2003.

[39] P. Yeh *et al.*, *Optical waves in layered media*. Wiley New York, 1988, vol. 95.

[40] P. Yeh, *Optical Waves in Layered Media*, ser. Wiley Series in Pure and Applied Optics. Wiley, 2005, ISBN: 9780471731924.

[41] C. P. Dietrich, A. Fiore, M. G. Thompson, M. Kamp, and S. Höfling, "Gaas integrated quantum photonics: Towards compact and multi-functional quantum photonic integrated circuits," *Laser & Photonics Reviews*, vol. 10, no. 6, pp. 870–894, 2016.

[42] A. J. Hoffman *et al.*, "Negative refraction in semiconductor metamaterials," *Nature materials*, vol. 6, no. 12, pp. 946–950, 2007.

[43] S. Debnath, E. Khan, and E. E. Narimanov, "Ghost-induced exact degeneracies," *Optics Letters*, vol. 46, no. 7, pp. 1708–1711, 2021.

[44] E. Khan, S. Debnath, and E. E. Narimanov, "Ghost resonance spectroscopy," in *CLEO: Science and Innovations*, Optical Society of America, 2021, SM3O–6.

[45] M. J. Weber, *Handbook of optical materials*. CRC press, 2018.

[46] H. Dong, H. Liu, and S. Wang, "Optical anisotropy and blue-shift phenomenon in tetragonal bifeo3," *Journal of Physics D: Applied Physics*, vol. 46, no. 13, p. 135 102, 2013.

[47] J. Midwinter and J. Warner, "The effects of phase matching method and of uniaxial crystal symmetry on the polar distribution of second-order non-linear optical polarization," *British Journal of Applied Physics*, vol. 16, no. 8, p. 1135, 1965.

[48] E. E. Narimanov, "Dyakonov waves in biaxial anisotropic crystals," *Physical Review A*, vol. 98, no. 1, p. 013 818, 2018.

[49] J. Nemirovsky, M. C. Rechtsman, and M. Segev, "Negative radiation pressure and negative effective refractive index via dielectric birefringence," *Optics Express*, vol. 20, no. 8, pp. 8907–8914, 2012.

[50] E. E. Narimanov, "Ghost resonance in anisotropic materials: Negative refractive index and evanescent field enhancement in lossless media," *Advanced Photonics*, vol. 1, no. 4, p. 046 003, 2019.

[51] H. C. Chen, *Theory of electromagnetic waves: a coordinate-free approach*. McGraw-Hill, 1983.

[52] M. Ku, F. Haake, and D. Delande, "Prebifurcation periodic ghost orbits in semiclassical quantization," *Physical review letters*, vol. 71, no. 14, p. 2167, 1993.

[53] M. Dyakonov, "New type of electromagnetic wave propagating at an interface," *Sov. Phys. JETP*, vol. 67, no. 4, pp. 714–716, 1988.

[54] O. Takayama, L.-C. Crasovan, S. K. Johansen, D. Mihalache, D. Artigas, and L. Torner, "Dyakonov surface waves: A review," *Electromagnetics*, vol. 28, no. 3, pp. 126–145, 2008.

[55] T. A. Albright, J. K. Burdett, and M.-H. Whangbo, *Orbital interactions in chemistry*. John Wiley & Sons, 2013.

[56] B. E. Saleh and M. C. Teich, *Fundamentals of photonics*. john Wiley & sons, 2019.

[57] J. B. Pendry, "Negative refraction makes a perfect lens," *Physical review letters*, vol. 85, no. 18, p. 3966, 2000.

[58] H. A. Haus and W. Huang, "Coupled-mode theory," *Proceedings of the IEEE*, vol. 79, no. 10, pp. 1505–1518, 1991.

[59] R. Shankar, *Principles of quantum mechanics*. Springer Science & Business Media, 2012.

[60] J. R. Pierce, "Coupling of modes of propagation," *Journal of Applied Physics*, vol. 25, no. 2, pp. 179–183, 1954.

[61] A. Yariv, "Coupled-mode theory for guided-wave optics," *IEEE Journal of Quantum Electronics*, vol. 9, no. 9, pp. 919–933, 1973.

[62] V. Veselago, "Properties of materials having simultaneously negative values of the dielectric and magnetic susceptibilities," *Soviet Physics Solid State USSR*, vol. 8, pp. 2854–2856, 1967.

[63] S. Sukhov and A. Dogariu, "Negative nonconservative forces: Optical tractor beams for arbitrary objects," *Physical review letters*, vol. 107, no. 20, p. 203 602, 2011.

[64] I. V. Shadrivov, A. A. Zharov, and Y. S. Kivshar, "Second-harmonic generation in nonlinear left-handed metamaterials," *JOSA B*, vol. 23, no. 3, pp. 529–534, 2006.

[65] A. Fiore, V. Berger, E. Rosencher, P. Bravetti, and J. Nagle, "Phase matching using an isotropic nonlinear optical material," *Nature*, vol. 391, no. 6666, pp. 463–466, 1998.

[66] K. Hannam, D. A. Powell, I. V. Shadrivov, and Y. S. Kivshar, "Dispersionless optical activity in metamaterials," *Applied Physics Letters*, vol. 102, no. 20, p. 201 121, 2013.

[67] K. L. Tsakmakidis, T. W. Pickering, J. M. Hamm, A. F. Page, and O. Hess, "Completely stopped and dispersionless light in plasmonic waveguides," *Physical review letters*, vol. 112, no. 16, p. 167 401, 2014.

[68] D. R. Smith, W. J. Padilla, D. Vier, S. C. Nemat-Nasser, and S. Schultz, "Composite medium with simultaneously negative permeability and permittivity," *Physical review letters*, vol. 84, no. 18, p. 4184, 2000.

[69] Z. Huang and E. E. Narimanov, "Optical imaging with photonic hyper-crystals: Veselago lens and beyond," *Journal of Optics*, vol. 16, no. 11, p. 114 009, 2014.

[70] W. Cai and V. Shalaev, "Optical properties of metal-dielectric composites," in *Optical Metamaterials*, Springer, 2010, pp. 11–37.

[71] H. Kosaka *et al.*, "Superprism phenomena in photonic crystals," *Physical review B*, vol. 58, no. 16, R10096, 1998.

[72] G. V. Eleftheriades, A. K. Iyer, and P. C. Kremer, "Planar negative refractive index media using periodically lc loaded transmission lines," *IEEE transactions on Microwave Theory and Techniques*, vol. 50, no. 12, pp. 2702–2712, 2002.

[73] A. Alù and N. Engheta, "Optical nanotransmission lines: Synthesis of planar left-handed metamaterials in the infrared and visible regimes," *JOSA B*, vol. 23, no. 3, pp. 571–583, 2006.

[74] R. W. Boyd, *Nonlinear optics*. Academic press, 2020.

[75] A. Weiner, *Ultrafast optics*. John Wiley & Sons, 2011, vol. 72.

[76] T. J. Kane and R. L. Byer, "Monolithic, unidirectional single-mode nd: Yag ring laser," *Optics letters*, vol. 10, no. 2, pp. 65–67, 1985.

[77] M. J. Weber, *Handbook of optical materials*. CRC press, 2002, vol. 19.

[78] J. Robertson, "Electronic structure of sno2, geo2, pbo2, teo2 and mgf2," *Journal of Physics C: Solid State Physics*, vol. 12, no. 22, p. 4767, 1979.

[79] H. Nasu, O. Matsushita, K. Kamiya, H. Kobayashi, and K. Kubodera, "Third harmonic generation from li2o–tio2–teo2 glasses," *Journal of non-crystalline solids*, vol. 124, no. 2-3, pp. 275–277, 1990.

[80] H. Lin, S. Jiang, J. Wu, F. Song, N. Peyghambarian, and E. Pun, "Er3+ doped na2o–nb2o5–teo2 glasses for optical waveguide laser and amplifier," *Journal of Physics D: Applied Physics*, vol. 36, no. 7, p. 812, 2003.

[81] E. Skelton, J. Feldman, C. Liu, and I. Spain, "Study of the pressure-induced phase transition in paratellurite (teo 2)," *Physical Review B*, vol. 13, no. 6, p. 2605, 1976.

[82] C. M. Bender and S. Boettcher, "Real spectra in non-hermitian hamiltonians having p t symmetry," *Physical Review Letters*, vol. 80, no. 24, p. 5243, 1998.

[83] S. K. Gupta *et al.*, "Parity-time symmetry in non-hermitian complex optical media," *Advanced Materials*, vol. 32, no. 27, p. 1 903 639, 2020.

[84] C. M. Bender and A. Turbiner, "Analytic continuation of eigenvalue problems," *Physics Letters A*, vol. 173, no. 6, pp. 442–446, 1993.

[85] C. M. Bender, "Introduction to $\mathcal{PT}$-symmetric quantum theory," *Contemporary physics*, vol. 46, no. 4, pp. 277–292, 2005.

[86] A. Beygi, S. Klevansky, and C. M. Bender, "Coupled oscillator systems having partial pt symmetry," *Physical Review A*, vol. 91, no. 6, p. 062 101, 2015.

[87] L. Feng, R. El-Ganainy, and L. Ge, "Non-hermitian photonics based on parity–time symmetry," *Nature Photonics*, vol. 11, no. 12, pp. 752–762, 2017.

[88] R. El-Ganainy, M. Khajavikhan, D. N. Christodoulides, and S. K. Ozdemir, "The dawn of non-hermitian optics," *Communications Physics*, vol. 2, no. 1, pp. 1–5, 2019.

[89] L. A. Shuvalov *et al.*, *Modern crystallography IV: physical properties of crystals*. Springer, 1988.

[90] . K. Özdemir, S. Rotter, F. Nori, and L. Yang, "Parity–time symmetry and exceptional points in photonics," *Nature materials*, vol. 18, no. 8, pp. 783–798, 2019.

[91] C. M. Bender, S. Boettcher, and P. N. Meisinger, "Pt-symmetric quantum mechanics," *Journal of Mathematical Physics*, vol. 40, no. 5, pp. 2201–2229, 1999.

[92] R. El-Ganainy, K. Makris, D. Christodoulides, and Z. H. Musslimani, "Theory of coupled optical pt-symmetric structures," *Optics letters*, vol. 32, no. 17, pp. 2632–2634, 2007.

[93] A. Guo *et al.*, "Observation of p t-symmetry breaking in complex optical potentials," *Physical Review Letters*, vol. 103, no. 9, p. 093 902, 2009.

[94] M. Brandstetter *et al.*, "Reversing the pump dependence of a laser at an exceptional point," *Nature communications*, vol. 5, no. 1, pp. 1–7, 2014.

[95] H. Hodaei, M.-A. Miri, M. Heinrich, D. N. Christodoulides, and M. Khajavikhan, "Parity-time–symmetric microring lasers," *Science*, vol. 346, no. 6212, pp. 975–978, 2014.

[96] S. Longhi, "Pt-symmetric laser absorber," *Physical Review A*, vol. 82, no. 3, p. 031 801, 2010.

[97] B. Peng *et al.*, "Parity–time-symmetric whispering-gallery microcavities," *Nature Physics*, vol. 10, no. 5, pp. 394–398, 2014.

[98] C. E. Rüter, K. G. Makris, R. El-Ganainy, D. N. Christodoulides, M. Segev, and D. Kip, "Observation of parity–time symmetry in optics," *Nature physics*, vol. 6, no. 3, pp. 192–195, 2010.

[99] Z. Lin, H. Ramezani, T. Eichelkraut, T. Kottos, H. Cao, and D. N. Christodoulides, "Unidirectional invisibility induced by p t-symmetric periodic structures," *Physical Review Letters*, vol. 106, no. 21, p. 213 901, 2011.

[100] A. Regensburger, C. Bersch, M.-A. Miri, G. Onishchukov, D. N. Christodoulides, and U. Peschel, "Parity–time synthetic photonic lattices," *Nature*, vol. 488, no. 7410, pp. 167–171, 2012.

[101] M.-A. Miri and A. Alu, "Exceptional points in optics and photonics," *Science*, vol. 363, no. 6422, 2019.

[102] J. Gomis-Bresco, D. Artigas, and L. Torner, "Transition from dirac points to exceptional points in anisotropic waveguides," *Physical Review Research*, vol. 1, no. 3, p. 033 010, 2019.

[103] . K. Özdemir, "Fermi arcs connect topological degeneracies," *Science*, vol. 359, no. 6379, pp. 995–996, 2018.

[104] H. Zhou *et al.*, "Observation of bulk fermi arc and polarization half charge from paired exceptional points," *Science*, vol. 359, no. 6379, pp. 1009–1012, 2018.

[105] M. I. Rosa, M. Mazzotti, and M. Ruzzene, "Exceptional points and enhanced sensitivity in pt-symmetric continuous elastic media," *Journal of the Mechanics and Physics of Solids*, vol. 149, p. 104 325, 2021.

[106] H. Hodaei *et al.*, "Enhanced sensitivity at higher-order exceptional points," *Nature*, vol. 548, no. 7666, pp. 187–191, 2017.

[107] Y. Wu, C. Li, X. Hu, Y. Ao, Y. Zhao, and Q. Gong, "Applications of topological photonics in integrated photonic devices," *Advanced Optical Materials*, vol. 5, no. 18, p. 1 700 357, 2017.

[108] G. B. Shvets, "Applications of topological photonics to light manipulation: From sorting to sub-wavelength confinement," in *Metamaterials, Metadevices, and Metasystems 2021*, International Society for Optics and Photonics, vol. 11795, 2021, 117951G.

[109] M. Kremer, T. Biesenthal, L. J. Maczewsky, M. Heinrich, R. Thomale, and A. Szameit, "Demonstration of a two-dimensional $\mathcal{PT}$-symmetric crystal," *Nature communications*, vol. 10, no. 1, pp. 1–7, 2019.

[110] S. Debnath and E. E. Narimanov, "Ghost resonance in optical scattering," in *Laser Science*, Optical Society of America, 2017, JW3A–105.

[111] S. Debnath and E. E. Narimanov, "Ghost resonance in light scattering," in *CLEO: Applications and Technology*, Optical Society of America, 2018, JW2A–89.

[112] D. W. Hahn, "Light scattering theory," *Department of Mechanical and Aerospace Engineering, University of Florida*, 2009.

[113] D. R. Smith, J. B. Pendry, and M. C. Wiltshire, "Metamaterials and negative refractive index," *Science*, vol. 305, no. 5685, pp. 788–792, 2004.

[114] M. Selvanayagam and G. V. Eleftheriades, "Experimental demonstration of active electromagnetic cloaking," *Physical review X*, vol. 3, no. 4, p. 041 011, 2013.

[115] J. J. Sakurai and E. D. Commins, *Modern quantum mechanics, revised edition*, 1995.

[116] D. W. Watson, S. D. Jenkins, J. Ruostekoski, V. A. Fedotov, and N. I. Zheludev, "Toroidal dipole excitations in metamolecules formed by interacting plasmonic nanorods," *Physical Review B*, vol. 93, no. 12, p. 125 420, 2016.

[117] A. C. Tasolamprou, O. Tsilipakos, M. Kafesaki, C. M. Soukoulis, and E. N. Economou, "Toroidal eigenmodes in all-dielectric metamolecules," *Physical Review B*, vol. 94, no. 20, p. 205 433, 2016.

[118] M. Gupta, Y. K. Srivastava, M. Manjappa, and R. Singh, "Sensing with toroidal metamaterial," *Applied Physics Letters*, vol. 110, no. 12, p. 121 108, 2017.

[119] J. U. Nöckel and A. D. Stone, "Ray and wave chaos in asymmetric resonant optical cavities," *Nature*, vol. 385, no. 6611, pp. 45–47, 1997.

[120] J.-W. Ryu and M. Hentschel, "Ray model and ray-wave correspondence in coupled optical microdisks," *Physical Review A*, vol. 82, no. 3, p. 033 824, 2010.

[121] S. Rasband, "Chaotic dynamics of nonlinear systems. new york: Wiley," 1990.

[122] A. Gonis and W. H. Butler, *Multiple scattering in solids*. Springer Science & Business Media, 1999.

[123] E. Rutherford, "The scattering of α and β particles by matter and the structure of the atom," *Philosophical Magazine*, vol. 92, no. 4, pp. 379–398, 2012.

[124] L. Faddeev, "Scattering theory for a three particle system," *Sov. Phys. JETP*, vol. 12, no. 5, pp. 1014–1019, 1961.

[125] R. G. Newton, *Scattering theory of waves and particles*. Springer Science & Business Media, 2013.

[126] M. Nevière, E. Popov, and R. Reinisch, "Electromagnetic resonances in linear and nonlinear optics: Phenomenological study of grating behavior through the poles and zeros of the scattering operator," *JOSA A*, vol. 12, no. 3, pp. 513–523, 1995.

[127] M. Kotlarchyk, "Scattering theory," 1999.

[128] M. Reed and B. Simon, *III: Scattering Theory*. Elsevier, 1979, vol. 3.

[129] H. Nussenzveig, "The poles of the s-matrix of a rectangular potential well of barrier," *Nuclear Physics*, vol. 11, pp. 499–521, 1959.

[130] R. L. Fante and M. T. McCormack, "Reflection properties of the salisbury screen," *IEEE transactions on antennas and propagation*, vol. 36, no. 10, pp. 1443–1454, 1988.

[131] W. W. Salisbury, *Absorbent body for electromagnetic waves*, US Patent 2,599,944, 610 1952.

[132] L. Ge, Y. Chong, and A. D. Stone, "Steady-state ab initio laser theory: Generalizations and analytic results," *Physical Review A*, vol. 82, no. 6, p. 063 824, 2010.

[133] S. Longhi and L. Feng, "Pt-symmetric microring laser-absorber," *Optics letters*, vol. 39, no. 17, pp. 5026–5029, 2014.

[134] D. G. Baranov, A. Krasnok, and A. Alù, "Coherent virtual absorption based on complex zero excitation for ideal light capturing," *Optica*, vol. 4, no. 12, pp. 1457–1461, 2017.

[135] C. W. Hsu *et al.*, "Observation of trapped light within the radiation continuum," *Nature*, vol. 499, no. 7457, pp. 188–191, 2013.

[136] Y. Yang, C. Peng, Y. Liang, Z. Li, and S. Noda, "Analytical perspective for bound states in the continuum in photonic crystal slabs," *Physical review letters*, vol. 113, no. 3, p. 037 401, 2014.

[137] K. Koshelev, A. Bogdanov, and Y. Kivshar, "Meta-optics and bound states in the continuum," *Science Bulletin*, vol. 64, no. 12, pp. 836–842, 2019.

[138] Y. Chong, L. Ge, and A. D. Stone, "P t-symmetry breaking and laser-absorber modes in optical scattering systems," *Physical Review Letters*, vol. 106, no. 9, p. 093 902, 2011.

[139] M.-A. Miri *et al.*, "Scattering properties of pt-symmetric objects," *Journal of Optics*, vol. 18, no. 7, p. 075 104, 2016.

[140] W. R. Sweeney, C. W. Hsu, S. Rotter, and A. D. Stone, "Perfectly absorbing exceptional points and chiral absorbers," *Physical review letters*, vol. 122, no. 9, p. 093 901, 2019.

[141] Y. A. Kuznetsov, *Elements of applied bifurcation theory*. Springer Science & Business Media, 2013, vol. 112.

[142] Y. Pomeau and P. Manneville, "Intermittent transition to turbulence in dissipative dynamical systems," *Communications in Mathematical Physics*, vol. 74, no. 2, pp. 189–197, 1980.

[143] S. H. Strogatz, *Nonlinear dynamics and chaos*. CRC press, 2018.

[144] D. A. Bykov and L. L. Doskolovich, "Numerical methods for calculating poles of the scattering matrix with applications in grating theory," *Journal of lightwave technology*, vol. 31, no. 5, pp. 793–801, 2012.

[145] M. Hutley and D. Maystre, "The total absorption of light by a diffraction grating," *Optics communications*, vol. 19, no. 3, pp. 431–436, 1976.

[146] R.-L. Chern and W.-T. Hong, "Nearly perfect absorption in intrinsically low-loss grating structures," *Optics Express*, vol. 19, no. 9, pp. 8962–8972, 2011.

[147] M. Neviere, "The homogeneous problem," in *Electromagnetic theory of gratings*, Springer, 1980, pp. 123–157.

[148] E. N. Bulgakov and D. N. Maksimov, "Optical response induced by bound states in the continuum in arrays of dielectric spheres," *JOSA B*, vol. 35, no. 10, pp. 2443–2452, 2018.

[149] E. Popov and L. Tsonev, "Electromagnetic field enhancement in deep metallic gratings," *Optics communications*, vol. 69, no. 3-4, pp. 193–198, 1989.

[150] P. Vincent and M. Neviere, "Corrugated dielectric waveguides: A numerical study of the second-order stop bands," *Applied physics*, vol. 20, no. 4, pp. 345–351, 1979.

[151] C. W. Hsu, B. Zhen, A. D. Stone, J. D. Joannopoulos, and M. Soljai, "Bound states in the continuum," *Nature Reviews Materials*, vol. 1, no. 9, pp. 1–13, 2016.

[152] Y. V. Fyodorov and H.-J. Sommers, "Statistics of resonance poles, phase shifts and time delays in quantum chaotic scattering: Random matrix approach for systems with broken time-reversal invariance," *Journal of Mathematical Physics*, vol. 38, no. 4, pp. 1918–1981, 1997.

[153] M. Hentschel and K. Richter, "Quantum chaos in optical systems: The annular billiard," *Physical Review E*, vol. 66, no. 5, p. 056 207, 2002.

[154] C. A. Balanis, *Advanced engineering electromagnetics*. John Wiley & Sons, 2012.

[155] G. Breit and E. Wigner, "Breit 1936," *Phys. Rev*, vol. 49, p. 519, 1936.

[156] Z. Chen, A. Taflove, and V. Backman, "Photonic nanojet enhancement of backscattering of light by nanoparticles: A potential novel visible-light ultramicroscopy technique," *Optics express*, vol. 12, no. 7, pp. 1214–1220, 2004.

[157] S. Lecler, Y. Takakura, and P. Meyrueis, "Properties of a three-dimensional photonic jet," *Optics letters*, vol. 30, no. 19, pp. 2641–2643, 2005.

[158] H. Mohseni, "Photonic jet and its applications in nano-photonics," in *Frontiers in Optics*, Optical Society of America, 2015, FM3B–4.

[159] I. V. Minin, O. V. Minin, Y. Cao, B. Yan, Z. Wang, and B. Luk'yanchuk, "Photonic lenses with whispering gallery waves at janus particles," *arXiv preprint arXiv:2012.09489*, 2020.

[160] E. Doron and U. Smilansky, "Semiclassical quantization of chaotic billiards: A scattering theory approach," *Nonlinearity*, vol. 5, no. 5, p. 1055, 1992.

[161] P. A. Martin, *Multiple scattering: interaction of time-harmonic waves with N obstacles*, 107. Cambridge University Press, 2006.

[162] T.-G. Tsuei and P. W. Barber, "Multiple scattering by two parallel dielectric cylinders," *Applied optics*, vol. 27, no. 16, pp. 3375–3381, 1988.

[163] O. Stavroudis, *The optics of rays, wavefronts, and caustics*. Elsevier, 2012, vol. 38.

[164] W. D. Newman *et al.*, "Observation of long-range dipole-dipole interactions in hyperbolic metamaterials," *Science advances*, vol. 4, no. 10, eaar5278, 2018.

[165] F. Jansen, F. Stutzki, C. Jauregui, J. Limpert, and A. Tünnermann, "Avoided crossings in photonic crystal fibers," *Optics Express*, vol. 19, no. 14, pp. 13 578–13 589, 2011.

[166] D. Smirnova, D. Leykam, Y. Chong, and Y. Kivshar, "Nonlinear topological photonics," *Applied Physics Reviews*, vol. 7, no. 2, p. 021 306, 2020.